Label-Free Detection of Single Biological Molecules Using Microtoroid Optical Resonators

Thesis by

Judith Su

In Partial Fulfillment of the Requirements

for the Degree of

Doctor of Philosophy

California Institute of Technology

Pasadena, California

2014

(Defended May 30, 2014)

To Dad, whose love for science was what sparked my curiosity.

Abstract

Being able to detect a single molecule without the use of labels has been a long standing goal of bioengineers and physicists. This would simplify applications ranging from single molecular binding studies to those involving public health and security, improved drug screening, medical diagnostics, and genome sequencing. One promising technique that has the potential to detect single molecules is the microtoroid optical resonator. The main obstacle to detecting single molecules, however, is decreasing the noise level of the measurements such that a single molecule can be distinguished from background. We have used laser frequency locking in combination with balanced detection and data processing techniques to reduce the noise level of these devices and report the detection of a wide range of nanoscale objects ranging from nanoparticles with radii from 100 to 2.5 nm, to exosomes, ribosomes, and single protein molecules (mouse immunoglobulin G and human interleukin-2). We further extend the exosome results towards creating a non-invasive tumor biopsy assay. Our results, covering several orders of magnitude of particle radius (100 nm to 2 nm), agree with the 'reactive' model prediction for the frequency shift of the resonator upon particle binding. In addition, we demonstrate that molecular weight may be estimated from the frequency shift through a simple formula, thus providing a basis for an "optical mass spectrometer" in solution. We anticipate that our results will enable many applications, including more sensitive medical diagnostics and fundamental studies of single receptor-ligand and protein-protein interactions in real time. The thesis summarizes what we have achieved thus far and shows that the goal of detecting a single molecule without the use of labels can now be realized.

Contents

List of Figures

List of Tables

Chapter 1

Introduction

1.1 Biological and chemical sensing using microtoroid optical resonators

Highly sensitive biodetection is important for many applications such as high throughput drug discovery studies, as it can dramatically reduce the amount of analyte needed and speed the assays. A variety of applications in medical diagnostics (e.g., detecting trace amounts of tumor specific antigens to monitor the re-occurrence of cancer) and public health (e.g., detecting bacteria or viruses) would benefit from improved speed and sensitivity [1]. If the sensitivity can be pushed to the single molecule level, fundamental studies become more direct and decisive, permitting, for example, studies of molecular conformations at a single molecule level [2]. Since the early reports in the mid-70's [3], label-mediated single-molecule detection has become routine in many laboratories. Certain biophysical events, such as, the action of molecular motors (myosins and kinesins) are best studied from a single molecule viewpoint. Basic features, such as the motor's step size, would be obscured by the averaging from traditional bulk measurements.

Biosensing techniques can be separated into two categories: those that require labeling of the target molecule (e.g., by attaching some fluorescent [4], radioactive [5], or enzymatic tag), and those that are label-free, sensing directly some physical property of the analyte. The majority of single molecule studies have required labels, using a bead or dye on a molecular motor to follow its motion over time, for example. Label-free sensing would have advantages, as labels can be expensive, difficult to generate, and for small analytes, might perturb the molecular events under study. One of the most commonly used label-free tests is, the ELISA, which senses an analyte via its binding to an antibody. In recent years, there has been a push towards the development of sensitive label-free techniques, resulting in a range of new ultra-sensitive techniques including optical microcavities [6, 7], mechanical sensors such as cantilevers [8, 9], and electrical sensors such as nanowires [10] and ion-sensitive field-effect transistors (ISFETs) [11]. The current gold standard for label-free, low concentration biosensing is the Biacore [12], an instrument first commercialized in 1990 that has since received over 1200 citations, attesting to its utility and popularity. The Biacore's operation is based upon surface plasmon resonance [12, 13], sensing the binding of an unlabeled analyte to a cognate receptor that has been covalently bound to a thin metal surface. The analyte binding is measured as the deflection of a laser bounced off the metal-solution interface, because the change in the index of refraction from the analyte alters the manner in which the plasmon waves of the metal substrate's surface interact with the evanescent light. While this sensing mechanism is label-free, the Biacore is not highly sensitive. It requires that enough analyte binds to alter the index of refraction over the region of the laser illumination. As a result, the typical lower limit of detection of the Biacore is on the order of nM in $\sim 250\ \mu$l of solution (Figure 1.1), several orders of magnitude greater than the typical of the single molecule regime ($\sim$ attomolar concentrations).

Recently a class of devices known as whispering gallery mode (WGM) optical resonators has attracted attention due to their potential for ultra-sensitive biological and chemical detection. These devices are named after the whispering gallery acoustical effect discovered by Lord Rayleigh while standing under the dome in St. Paul's cathedral in London. Whispers at one end of the dome could be heard at the other end due to the sound reflecting along the edges of the dome with low loss [14]. Whispering gallery mode optical resonators operate based on light circulating inside a glass device. The figure of merit for these devices is known as the quality factor (Q), defined as the ratio of the resonant wavelength (λ), to its linewidth ($\Delta\lambda$). Q is proportional to how many times the light circulates around the cavity; for a large Q ($Q > 10^8$), each photon circulates over 250,000 times. Because of the bent optical path there is evanescence from the toroid surface into the surrounding

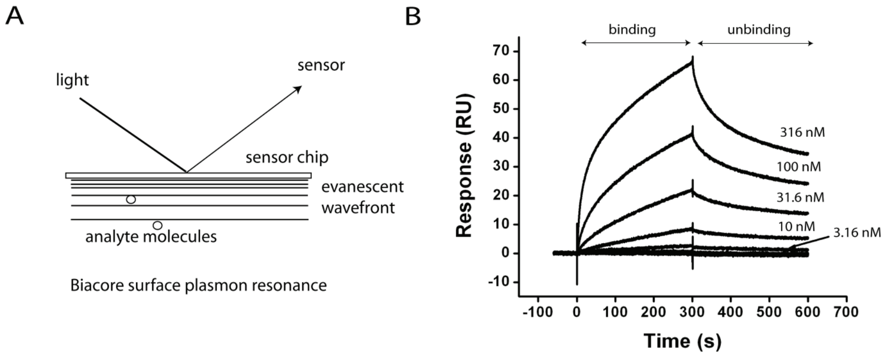

Figure 1.1: Biosensing with a Biacore surface plasmon resonance instrument.(A) The binding of analytes to covalently attached binding partners (i.e., antibodies or receptors) changes the index of refraction near the metal film and changes the angle of the reflection. As the change in index of refraction requires no exogenous label, and is proportional to the amount of analyte bound, the magnitude and rate of deflection provide a simple means to obtain quantitative data on binding. (B) Biacore response plot (sensorgram) of biotinylated-protein G binding to streptavidin (linked to the sensor chip). A half log dilution series was preformed from micromolar down to attomolar concentrations. The minimum detectable response was 3.16 nM. Traces from smaller concentrations spanning nine orders of magnitude superimpose as the lowest trace and are indistinguishable from noise.

fluid, permitting a Biacore-like sensing of an analyte bound to the surface. Because these devices are made of glass they can be functionalized to allow for the specific attachment of "bait" molecules. When analyte molecules bind to the bait this causes a change in the index of refraction near the device, which in turn alters the resonance frequency (Figure 1.2). The high Q contributes to the sensitivity in two ways: first, the light circulates in a small mode volume over 250,000 times, re-interrogating any bound analyte many times; second, the high Q value gives a narrow resonance peak, whose wavelength can be measured accurately.

The most widely used of these optical resonators for biosensing are the microsphere [15–24], microring [25–42], and microtoroid [43–48], so named because of their geometries. Due to the heat reflow (melting) treatment designed to remove surface imperfections, microspheres and microtoroids possess an extremely (atomic scale) smooth surface finish [44], and thus retain light for longer (on the order of tens of nanoseconds) periods of time. Microrings retain the lithographic blemishes caused during manufacturing; however, they can be fabricated in conjunction with a waveguide to input light (as opposed to microspheres and microtoroids that require critical positioning of a tapered optical fiber). This permits the fabrication of large arrays and so offers the advantage of being able

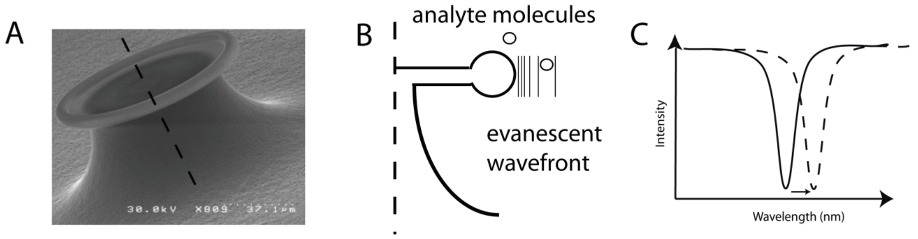

Microtoroid scanning electron micrograph

Microtoroid cross-section

Molecular binding is detected by shifts in the resonance frequency

Figure 1.2: The microtoroid as an example of a whispering gallery mode optical resonator. (A) A scanning electron micrograph of a microtoroid. (B) A schematic of the evanescent wavefront interacting with molecules near the microtoroid (not to scale) (C) Molecules binding to the toroid's surface changes the resonant frequency of the device. Whispering gallery mode resonators provide enhanced sensitivity as light interacts with the analyte molecules multiple times.

to perform many experiments simultaneously on a large scale. To date, microspheres have been shown capable of detecting a single nucleotide polymorphism in a μM of solution [22] as well as a single InfA virus [15] and microrings have been used to simultaneously detect 5 different protein markers with picomolar sensitivity [49].

Compared to microspheres and microrings, microtoroids are likely to have the greatest sensitivity [44]. Microtoroids have demonstrated 100 times higher quality values in water [50] and have smaller mode volumes than microspheres, which should increase sensitivity by increasing the number of times light circulates and by concentrating more light in a smaller volume. In addition, the toroids have fewer propagation angles than a sphere, and they are easier to mode match to the optical fiber taper, maximizing the size and sharpness of the drop in transmission of the optical fiber that appears at the WGM resonance (Figure 1.2).

Extremely high sensitivity was demonstrated by Lu et al. [50], who used a Mach-Zehnder interferometer as a means to more accurately measure the laser wavelength, allowing them to subtract laser frequency jitter noise from the measured toroidal response signal, thus enhancing sensitivity. With this approach, they demonstrated detection of single InfA virus ($\sim$ 100 nm) particles, and $r = 12.5$ nm polystyrene beads using a microtoroid. In terms of mass, this represents a detection of 75 and 9 ag, respectively. For comparison, HIV has a mass of 600 ag, the smallest RNA virus MS2 has a mass of 6 ag, and BSA has a mass of 0.1 ag [21]. We note that detection signal strength scales with particle volume [18].

In a hybrid dual-resonator approach, microspheres have recently been coupled to 70 nm radius silica core gold nanoshells to boost signal in order to detect single BSA ($\sim$ 14 nm) molecules [21], however, this approach is limited in that there are only two hotspots per nanoparticle and one nanoparticle per microsphere limiting the active detection area of the sensor. The advance described here, Frequency Locked Optical Whispering Evanescent Resonator (FLOWER), would improve the detection capabilities of optical resonators in general, including hybrid systems.

1.2 The microtoroid as a viable, quantitative biosensor

To compare the microtoroid [44] as a biosensor with the Biacore, we performed parallel analyses of the same series of analyte solutions (Protein A) and binding partners attached to the sensors (Fc Region of human IgG). An example microtoroid response trace for a 1.0 nM concentration of protein A shows a measured resonance shift of the toroid with a signal-to-noise ratio (SNR) of > 3 in 15 seconds (Figure 1.3), significantly faster than the Biacore performance at 3 nM (Figure 1.1B). The Biacore, and other emerging label-free biodetection techniques such as cantilevers [51], are in general slower, with steady state response times of up to hours. The fast response times of the microtoroids offer advantages for applications such as high throughput analyses and medical diagnostics. This data was taken via the conventional swept-frequency method in which the laser continuously scans through a range of wavelengths to find the resonance wavelength of the microtoroid.

Quantitative parameters such as equilibrium dissociation constants (K_d, the concentration of analyte that produces a response at half saturation) can be extracted from the microtoroid from a dose-response curve. For the Biacore, this involves plotting the steady state beam deflection for a series of concentrations; for the microtoroids this involves plotting the steady state resonance wavelength shift. Figure 1.4 compares the dose-response curves for the Biacore and microtoroid sensors, using the same Protein A-IgG interaction pair as used in Figure 1.3. Good agreement of the values reported by the toroid (K_d of 6×10^{-9}M) and the Biacore (K_d of 4.5×10^{-9}M) even with the sparse ($N = 1$) data set. Interestingly, the dose-response curve of the toroid is steeper (Hill coefficient of ~ 6) than the curve obtained by the Biacore (Hill coefficient of ~ 1). This higher Hill coefficient suggests some form of cooperative process occurring on the toroid.

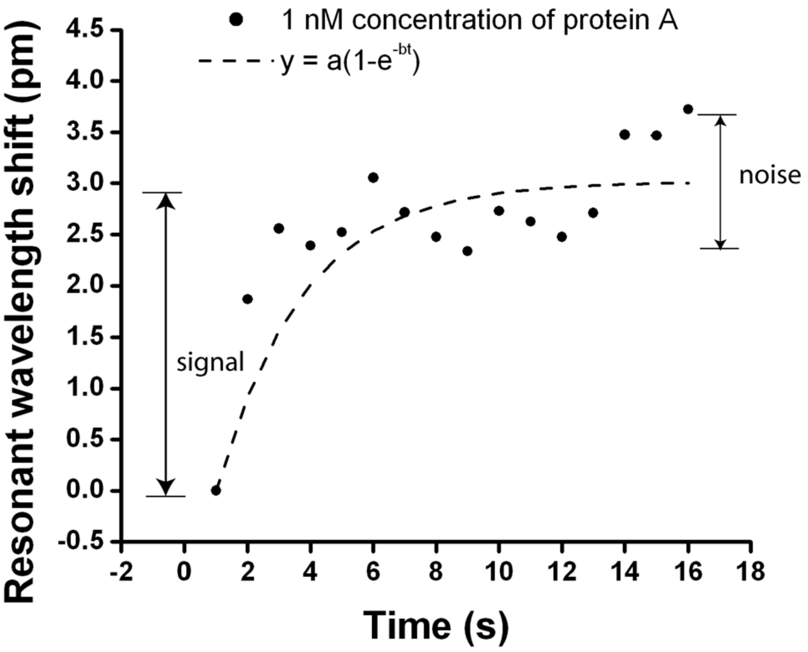

Figure 1.3: Response trace for a microtoroid WGM resonator. The resonance wavelength shifts within seconds to a new value after a 1 nM solution of protein A is flowed onto a toroid functionalized with the Fc region of human IgG. The response to the flow rate of 50μl/min is fit adequately by a simple exponential ($r^2 = 0.7$).

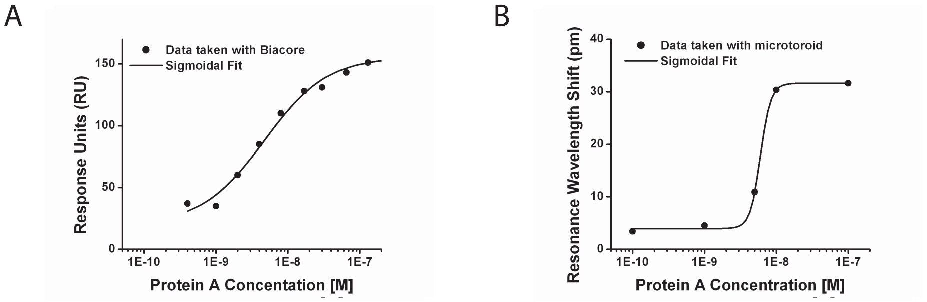

Figure 1.4: Dose response curves for protein A binding to human Fc fragments. (A) Equilibrium experiment performed on a Biacore. (B) Equivalent experiment performed on the toroid with human Fc covalently bound to the surface.

1.3 What is the true limit of detection? The single molecule controversy

In 2007, a paper was published by in Science [52] claiming to have detected single molecules using the microtoroid, however, this result was met with considerable skepticism [27, 53–55]. In this report, an antibody directed against interleukin-2 was non-specifically bound to the surface of the microtoroid and a low concentration of interleukin-2 was flowed by. Sudden, step-like changes in resonance wavelength were taken to be the response of the microtoroid to single molecules. As expected, the rate of these events linearly scaled with concentration (but the amplitude did not) and followed Poisson binding statistics in time as would be expected for single molecule detection. In addition, an experiment was performed in which fluorescently tagged molecules were bound to the microtoroid so that their unitary photo-bleaching could be used to "count" molecules. Unitary blue shifts in the resonance wavelength and corresponding increases in the quality factor of the microtoroid were seen, as anticipated when particles with large absorption cross-sections bleach or un-bind from the microtoroid.

In support of these experiments, a thermo-optic model was proposed to explain the step-like shifts from single molecules binding [52]. The thermo-optic theory proposed that the local heating of the toroid would result from the large circulating power interacting with single molecules bound to the toroid. The temperature dependence of the index of refraction would thereby amplify any wavelength shift as single molecules bound to the toroid. The molecular cross-sections used to calculate the expected shifts from a single molecule, however, were recorded as more than a factor of a 1000 too large, calling into question the reported match between experiment and theoretical prediction [54, 56]. As stated in [54]:

> Our Streptavidin cross section plugged into Armani's theoretical equation would yield a wavelength shift less than one thousandth of what is calculated and measured in [Armani, et al.]—and—For the conditions presented in [Armani, et al.] (i.e. standard parameters) our calculations show that the thermo-optic mechanism associated with linear absorption is smaller than its reactive counterpart, and cannot account for even one thousandth of the reported frequency shifts attributed to single protein binding.

Thus, the model as developed in [52] does not predict the experimentally observed steps, given the real absorbance cross sections. A correction was later published retracting the model [57]. As a further point of controversy, the results have yet to be repeated [53, 55].

Linear theory suggests that the shift is dependent purely on index of refraction changes in the evanescent field due to the binding of a molecule, and not on the quality factor of the toroid or laser power [54]. Arnold, et al., computed the ratio of the contribution from the linear reactive mechanism to the thermo-optic mechanism for both a sphere and a toroid and found that the contribution from the thermo-optic mechanism should only be 40% of the linear mechanism, and not several thousand times larger as was initially predicted [52]. Therefore, we expect the observed shift to be approximately predicted by the linear mechanism alone by at least within a factor of 2. This greatly simplifies the model.

Questions have also been raised regarding the high binding rate of molecules to the microtoroid's surface. Squires et al., [51] modeled based on pure diffusion what the time between binding events should be and arrived at an estimate of one event every six to seven seconds for a molecule of diffusivity $D = 10\ \mu\text{m}^2/\text{s}$ and a concentration of 10 fM. Furthermore, Squires et al., calculated that equilibrium should take around one hour to reach. Recent work by Arnold, et al., has shown that microspherical optical resonators generate optical trapping forces that cause significantly enhanced (100×) nanoparticle transport velocities [58]. We anticipate this effect to be even greater in our frequency-locked system as we are always on resonance as opposed to sweeping past resonance, thus increasing the amount of circulating power our devices experience. This significantly increases the expected particle encounter rate. Our rates are consistent with the binding rates from nanowire experiments which report saturation from the binding of thousands of molecules within seconds at similar concentrations [10]. We note that the binding rates from our experiments and from nanowire experiments are dramatically faster than the mass transport predicted by Squires et al. A full analysis of the mass transport in this system remains unavailable, and the discrepancy between Squires predicted rate and the results from microtoroids remains an open controversy

Chapter 2

Microtoroid creation and experimental setup overview

2.1 Toroid fabrication

Microtoroids are fabricated using a combination of lithography and etching techniques [44]. An overview of this process may be seen in Figure 2.1. First, circular pads of photoresist are patterned on top of a silicon wafer with a 2 micron thick thermal oxide layer. After patterning, the areas in between the circular pads are etched away using hydrofluoric acid, leaving behind a silicon pad with an SiO_2 top. The silicon pad is selectively undercut using XeF_2 etching to form a pillar. This structure is known as a microdisk. To generate an atomically smooth surface finish, the microdisk is melted or reflowed using a CO_2 laser. This process collapses the microdisk into a smooth structure known as a microtoroid. To further ensure high quality factors, we used intrinsic silicon wafers. These wafers have been doped with a less than typical amount of Boron. The presence of Boron lowers the index of refraction of the microtoroid and has been shown as a result to lower the quality factor [59]. An SEM micrograph of an array of microtoroids can be seen in Figure 2.2.

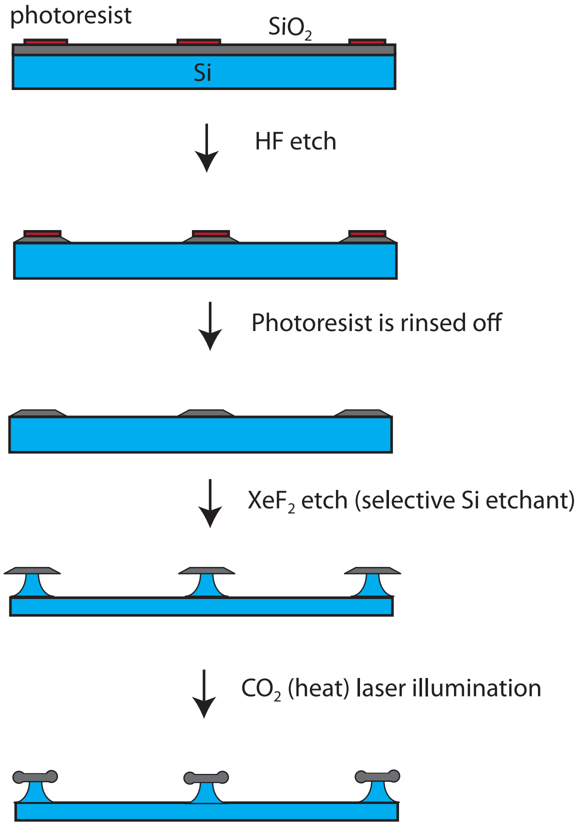

Figure 2.1: Microtoroid fabrication flow stream. Toroids are fabricated through a combination of lithography and etching. First, circular pads of photoresist are patterned on top of a silicon wafer with a 2 micron thick thermal oxide layer. Then, the areas between the pads are etched away. The photoresist is rinsed off leaving pillars which are undercut to form a microdisk structure. Finally, the microdisk is collapsed into a toroid using heat from a CO$_2$ laser.

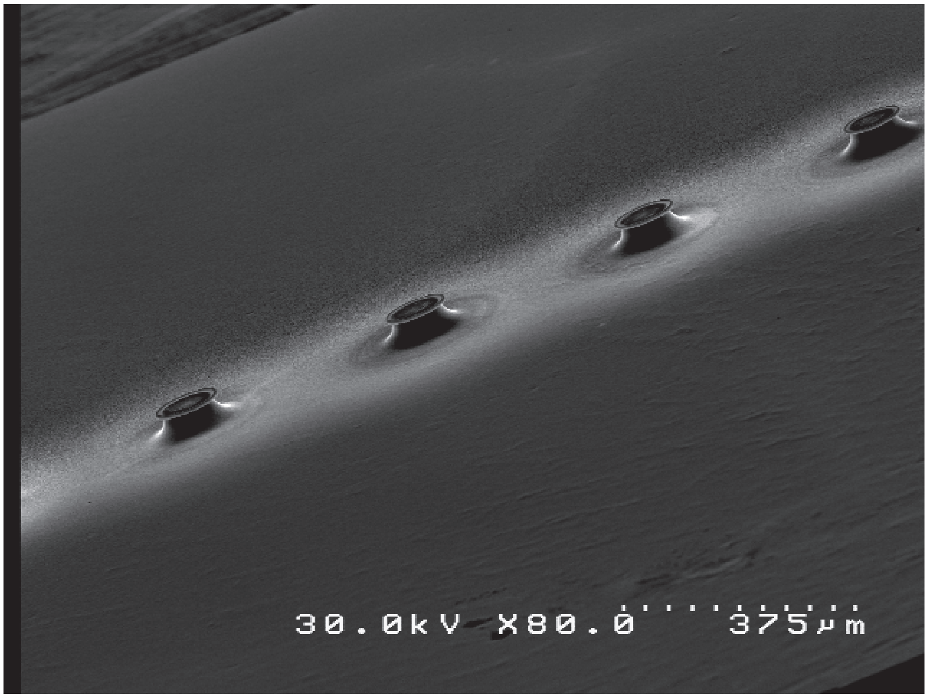

Figure 2.2: SEM micrograph of an array of microtoroids. Toroids are fabricated on a silicon wafer following the procedures of [44]. Toroid fabrication was performed using the cleanroom facilities at the Kavli Nanoscience Institute (KNI), Caltech.

2.2 Modification of CO_2 laser reflow system

One significant challenge in creating microtoroids, is the successful creation of microtoroids with ultra-high ($> 10^8$) quality factors. This requires extremely uniform heating of the toroid when it is in the microdisk stage. To improve our yield of ultra-high-quality microtoroids, we implemented a flat top laser beam shaper (Edmund Optics) made out of ZnSe that converts the Gaussian laser beam input from our CO_2 laser to a collimated flat output beam. As shown in Figure 2.3, the flat top laser beam shaper provides more uniform illumination and therefore a more uniform reflow of the microdisk. A schematic of the CO_2 laser reflow system may be seen in Figure 2.4. Because the wavelength of the CO_2 laser light (10.6 μm) is invisible to the human eye, the laser was first aligned using a Helium Neon laser at 633 nm. Some photographs of the setup are shown in Figure 2.5. To perform reflow, a ramp waveform 10 ms long and 2 volts peak to peak was sent via a function generator to the CO_2 laser.

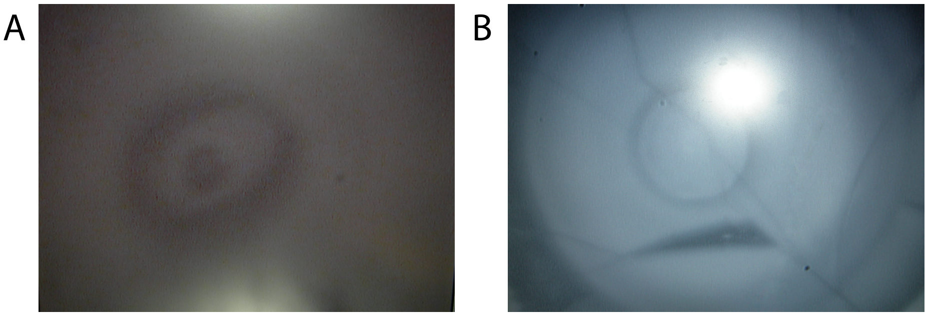

Figure 2.3: Uniform illumination of the microdisk allows for a symmetric toroidal structure to be created. To aid in this process, a flat top laser beam shaper was used. The effect of the flat top laser beam shaper may be seen by shooting the CO_2 laser beam at a glass coverslip and looking at the shape of the melted glass. As shown in (A), before the addition of the beam shaper the beam spot is non-circular while as shown in (B), after the addition of the beam shaper the beam spot is very circular and uniform.

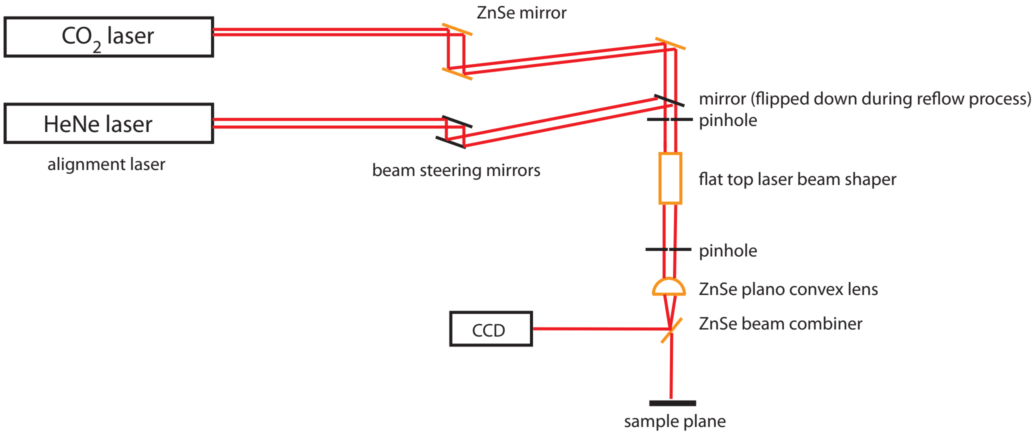

Figure 2.4: Schematic of CO_2 laser reflow system. The CO_2 laser beam is steered using ZnSe mirrors and focused onto the microdisk using a plano-convex ZnSe lens. A flat top laser beam shaper which converts a Gaussian laser beam input to a top-hat output beam was added before the focusing lens to enable more uniform heating of the microtoroid.

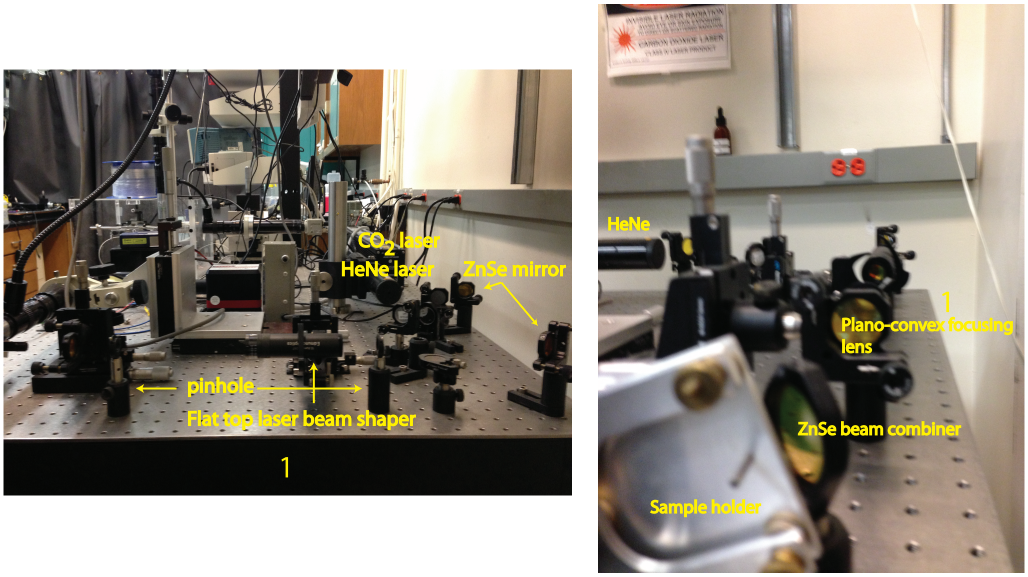

Figure 2.5: CO_2 laser reflow system photographs. As shown in the photographs, the CO_2 laser was hard mounted onto an air floated optical table for stability. The beam was steered using ZnSe mirrors and aligned through two pinholes. Finally, the beam was focused onto the microdisk sample using a plano-convex ZnSe lens. For visualization purposes a beam combiner which passes light at 10.6 μm and reflects light at 633 nm was placed before the sample so that the visible light could be reflected through an imaging column and towards a camera.

2.3 Optical fiber pulling setup

There are several ways of coupling light into microresonators, including direct illumination, prism coupling, and tapered optical fiber coupling. Of these, we use evanescent coupling from a tapered optical fiber because of its low loss [60–62]. In a typical optical fiber, the cladding and large diameter of the fiber prevents evanescent light from leaking out of the fiber. In our case, we want the evanescent mode to leak out from the part of the fiber adjacent to the toroid. This can be easily achieved by removing the cladding from the fiber in this region and by pulling on the fiber to shrink its diameter in this region. When the fiber's diameter is on the order of or smaller than the optical wavelength, a significant amount of optical power is carried in the evanescent field of the fiber. When the toroid is brought within this evanescent field, light naturally couples from the fiber to the toroid and back again. It is important to develop a repeatable method for thinning the fiber in a small region, which we do using a hydrogen torch.

Briefly, a spool of single mode optical fiber was purchased from Newport and about a meter was unwound. One end of the spool was fiber coupled into the laser, while a 1 cm portion of cladding was removed from the middle of the unwound section. Removing the cladding changes the index of refraction of the optical fiber making it multi-mode, so the optical fiber is simultaneously thinned and pulled until it can only support one mode again. The first step in this procedure is washing the portion of the optical fiber that has had the cladding removed with isopropanol alcohol and clamped on either end with magnetic clamps. The assembly was mounted above a hydrogen torch and the fiber was simultaneously heated and pulled in opposite directions at 60 μm/min using two stepper motors (Edmund Optics). To make the heating and thus the thickness of the optical fiber more uniform, the hydrogen torch was dithered horizontally (Figure 2.6(a) and Figure 2.6(b)) at 1 Hz. Pulling was stopped when the fiber became single mode (i.e., when the core diameter reduced to a diameter at which only one mode of light propagation was supported). This was visually estimated to occur when the laser light through the optical fiber stopped blinking and therefore we could conclude that significant intensity fluctuations had stopped. The end of the optical fiber was then cleaved and inserted into an auto-balanced photodetector using a bare fiber adapter. A typical waist diameter for the optical fiber is $\sim$ 500 nm.

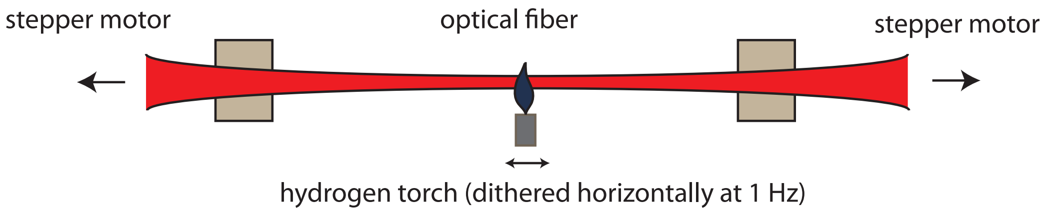

(a) Optical fiber taper puller schematic.

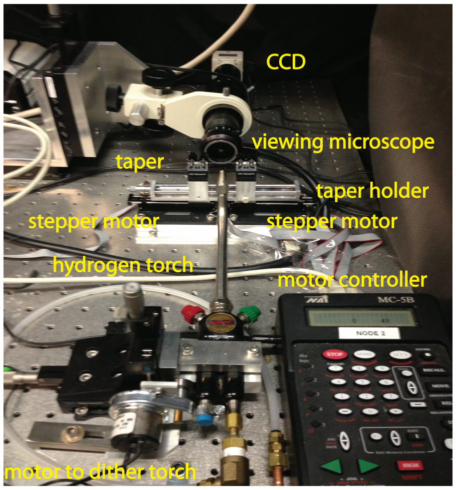

(b) Optical fiber taper puller picture.

Figure 2.6: (a) Schematic of the optical fiber taper puller. To thin the optical fiber sufficiently such that the majority of the light is carried evanescently, the optical fiber is heated using a hydrogen torch and pulled using two stepper motors. To enable more uniform heating of the optical fiber, the hydrogen torch was dithered at a frequency of 1 Hz. (b) Photograph of the optical fiber taper puller. The optical fiber is held in place using a custom machined holder with magnetic clamps. Two stepper motors pull the optical fiber in opposite directions while a hydrogen torch heats the fiber. For visualization purposes, an imaging column with a low (10×) magnification objective and CCD camera is positioned such that a side view of the optical fiber may be seen while pulling occurs.

2.4 Testing setup

Once an optical fiber has been pulled, the resonance peak of the microtoroid may be found by first bringing the toroid into close proximity to the optical fiber using a three-axis nanopositioner (Physik Instrumente). The coupling efficiency of light into the toroid may be tuned by controlling the distance between the optical fiber and the microtoroid [56]. A schematic of the testing setup is shown in Figure 2.7. Two imaging columns are placed perpendicular to each other to generate a top view and a side view image of the microtoroid so that the microtoroid may be visually aligned to the optical fiber. Due to the extreme sensitivity of our system to thermal effects, a hot mirror that reflects infrared light was placed in front of both imaging light sources. Some photographs of the setup may be seen in Figure 2.8. A schematic of the toroid positioned in relation to the optical fiber is shown in Figure 2.9.

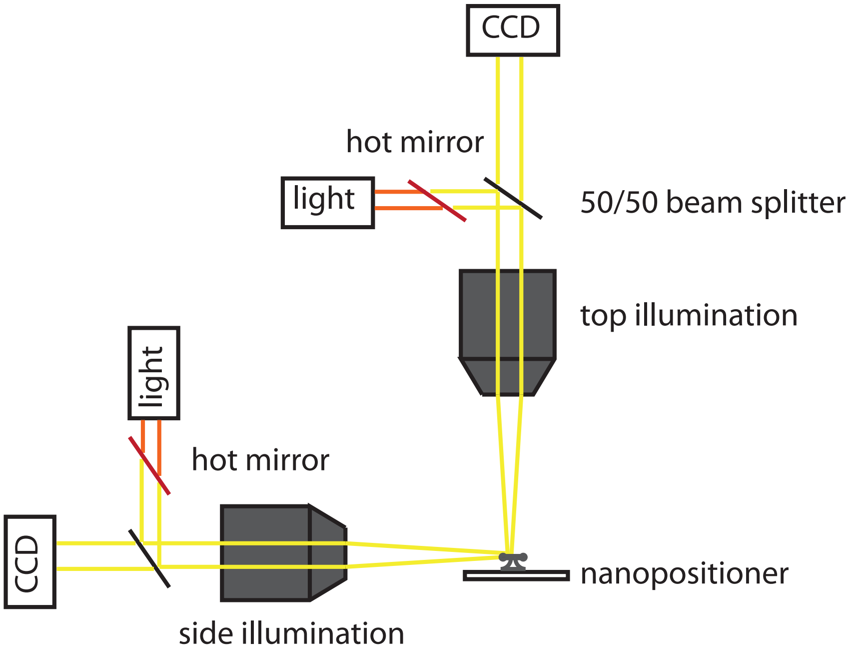

Figure 2.7: Schematic of the testing setup. The microtoroid is on a sample stage that is placed on top of a 3-axis nanopositioning stage that can move the toroid in precise alignment to the optical fiber (shown in Figure 2.8). Two objectives provide both top and side illumination so that the toroid can be viewed from both directions. This helps in precisely aligning the optical fiber with the microtoroid. To reduce thermal effects, hot mirrors that reflect infrared light are placed in front of the imaging lamps.

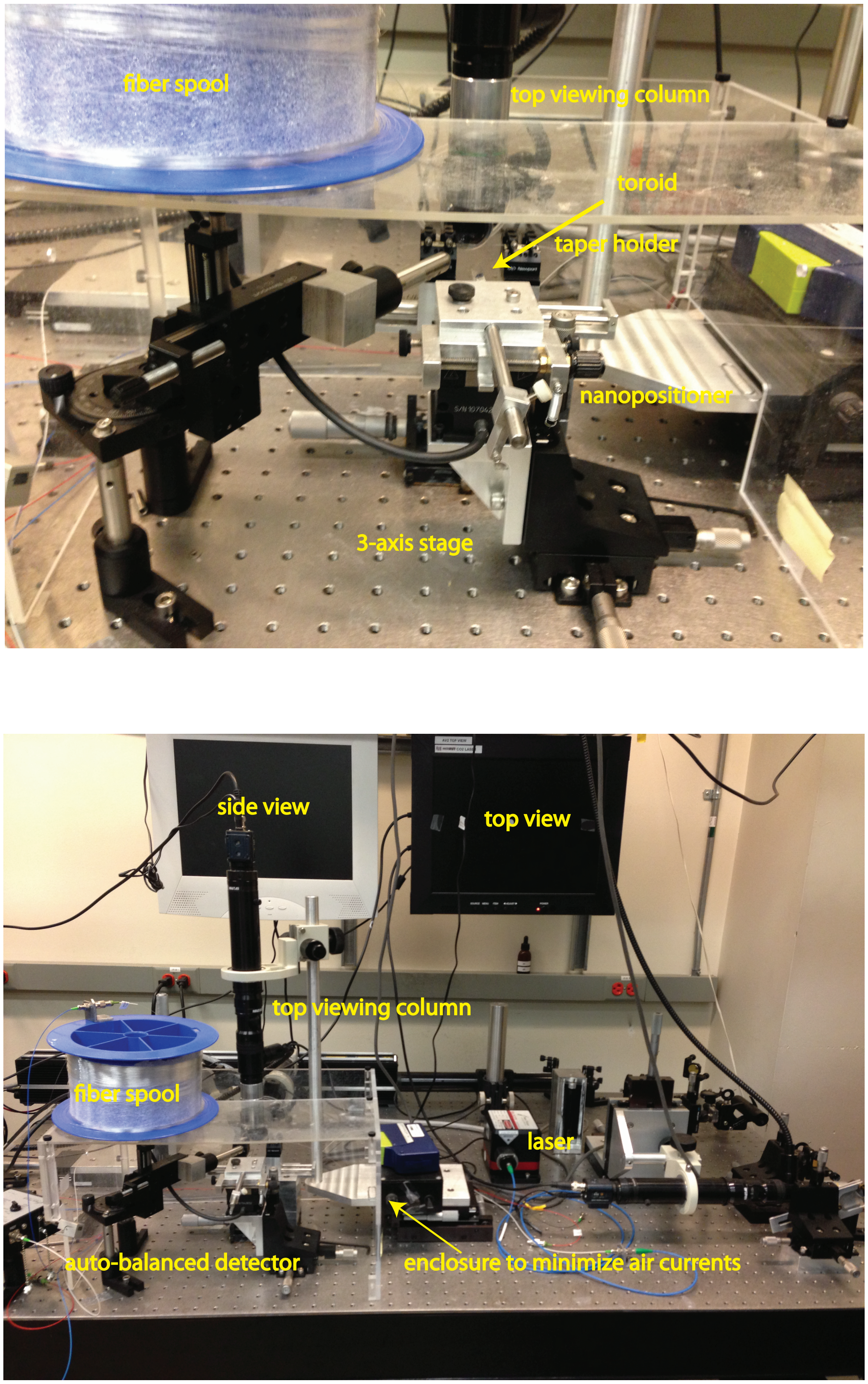

Figure 2.8: Testing setup pictures. The microtoroid is precisely positioned relative to the optical fiber using a 3-axis nanopositioner. The optical fiber is secured in place using magnetic clamps in a custom built holder. To aid in the alignment of the optical fiber with the microtoroid, two visualization columns with microscope objectives and cameras are placed to the top and side of the microtoroid. One end of the optical fiber is connected to a tunable wavelength laser while the other end of the optical fiber is connected to a photodetector. A Plexiglas enclosure is placed over the system to minimize air currents.

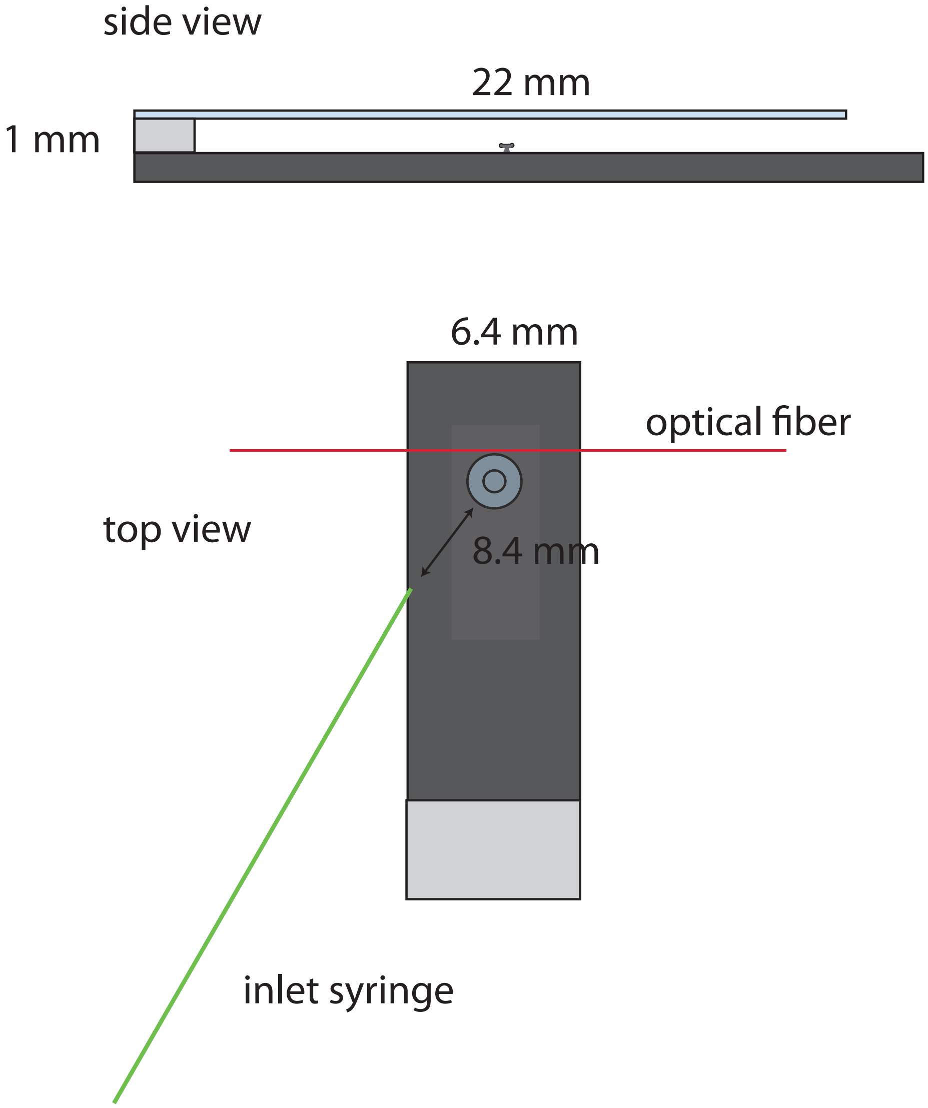

Figure 2.9: Schematic of microtoroid aligned in relation with optical fiber and inlet syringe for fluid flow injection. The microtoroid which is on a silicon chip, is mounted using an adhesive to a steel rod sample holder which is mounted to a 3-axis nano-positioning stage. So that the toroid can be visualized in an aqueous environment, a microscope coverslip is cantilevered out over the microtoroid using a microscope slide as a spacer. Both the coverslip and the slide are cut to the dimensions of the sample holder using a diamond cutter. The coverslip is adhered to the microscope slide using instant Krazy Glue.

Chapter 3

Improving the signal-to-noise ratio using laser frequency locking

3.1 Introduction

The main hurdle for single molecule detection is improving the signal-to-noise ratio such that the one molecule can be distinguished from background. Typically with whispering gallery mode resonators, molecular binding events are detected by continuously scanning the input frequency of a laser using a function generator and monitoring transmission dips in the optical fiber output that occur when resonance is found. This process is further illustrated in (Figure 3.1).

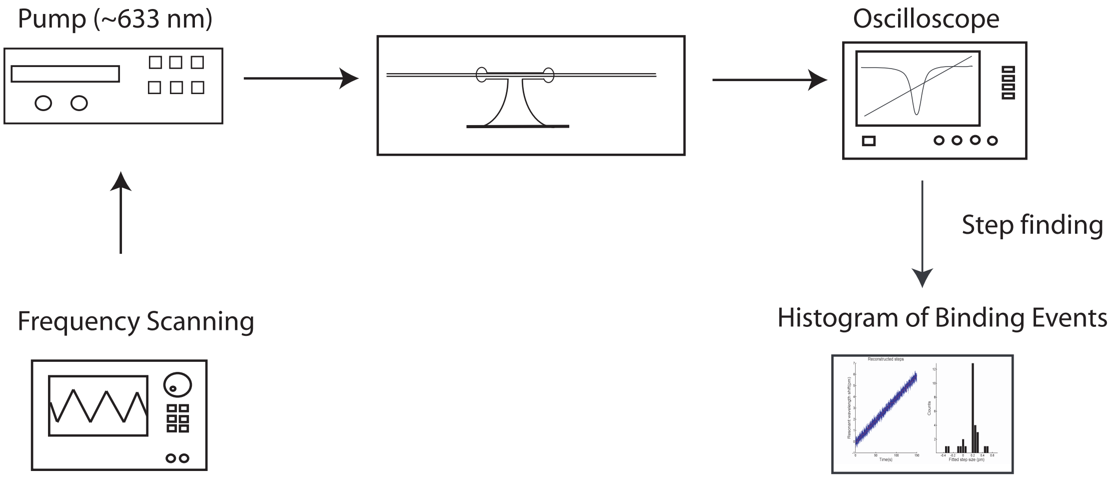

Figure 3.1: Overview of a conventional scanning method for tracking resonant wavelength shifts using a microtoroid optical resonator. In this system, the wavelength of a tunable laser is continuously scanned through a range of wavelengths using a function generator to locate the resonant wavelength of the microtoroid. The output of the scan is detected using a photodetector and the results are displayed using an oscilloscope.

Once resonance is found, the wavelength trace is recorded and curve fit to find the peak. Tracking the centroid of the peak over time generates a data set to which steps may be fit and a histogram of binding events may be created. This method takes a long time and has accuracy limited to the rate (typically 100 Hz for a conventional tunable laser system such as New Focus 6300) and range at which the laser is being swept.

Our frequency locking approach is an improvement over prior scanning systems that continually sweep back and forth over a large frequency range (3.1×10^4 fm, only occasionally matching resonance. In contrast, our work directly tracks the resonant wavelength location within a narrow and adaptively varied frequency range with a fixed length of 19 fm. Thus we track discrete fluctuations in signal more accurately and quickly, permitting slight and transient events to be detected (Figure 3.2). Frequency locking feedback control has been used in applications such as in scanning tunneling microscopy to maintain tip-surface separation [63]; however, to the best of our knowledge has not previously been used as a means to sense biological molecules [64].

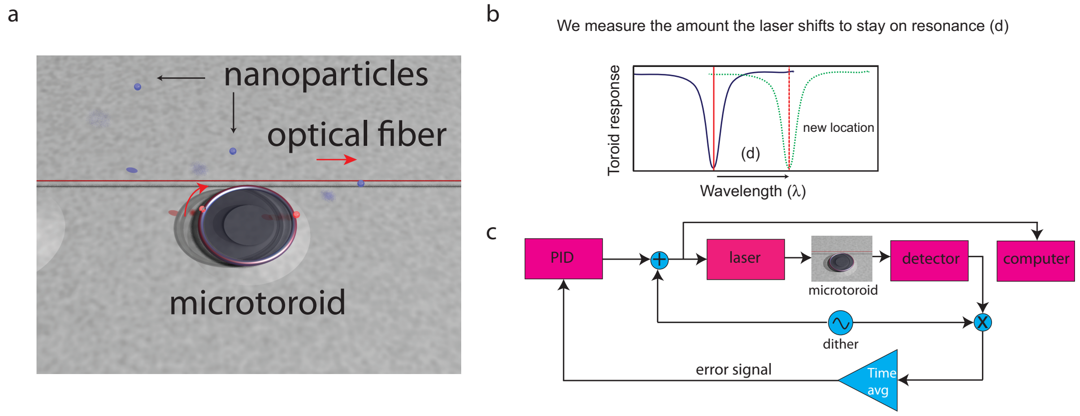

Figure 3.2: (a) Rendering of a microtoroid coupled to an optical fiber (not to scale). In our system, a frequency-tuned laser beam is evanescently coupled to a microtoroid ($\sim$ 90 microns in diameter) using an optical fiber (red). At resonance, light (red curved arrow) coming out of the microtoroid destructively interferes with light going straight through the optical fiber (red arrow), causing a dip in the transmission (peak in absorption) vs. light wavelength. (b) Conceptual basis for particle detection. The laser frequency (red solid line) is locked to the resonance frequency of the microtoroid (blue line). As particles bind, the resonant frequency of the microtoroid shifts to a new location (green dotted line). We measure the control signal needed to keep the laser locked to the microtoroids new resonance frequency (red dashed line). (c) Block diagram of the sensing control system. A small high-frequency dither is used to modulate the driving laser frequency. When multiplied by the toroid output and time-averaged, this dither signal generates an error signal whose amplitude is proportional to the difference between the current laser frequency and resonant frequency. This error signal is sent to a PID controller whose output is used to set the laser frequency, thus completing the feedback loop. A computer records the observed frequency shifts.

This approach has two main advantages:

1. **Continuously staying on resonance.** We are tracking the peak with greater accuracy.
2. **Sampling more points per second.** We sample at 20 kHz vs. 100 Hz which permits more averaging. At present, we have achieved millisecond time resolution with the potential for microsecond time resolution as we are limited only by the speed of our electronics.

3.2 System Overview

Locking the laser frequency to the resonance frequency of the microtoroid is first achieved by finding the location of the resonance peak by using conventional scanning methods (Figure 3.4). The quality factor of the microtoroid, defined as the ratio of the resonant wavelength (λ), to its linewidth ($\Delta\lambda$),

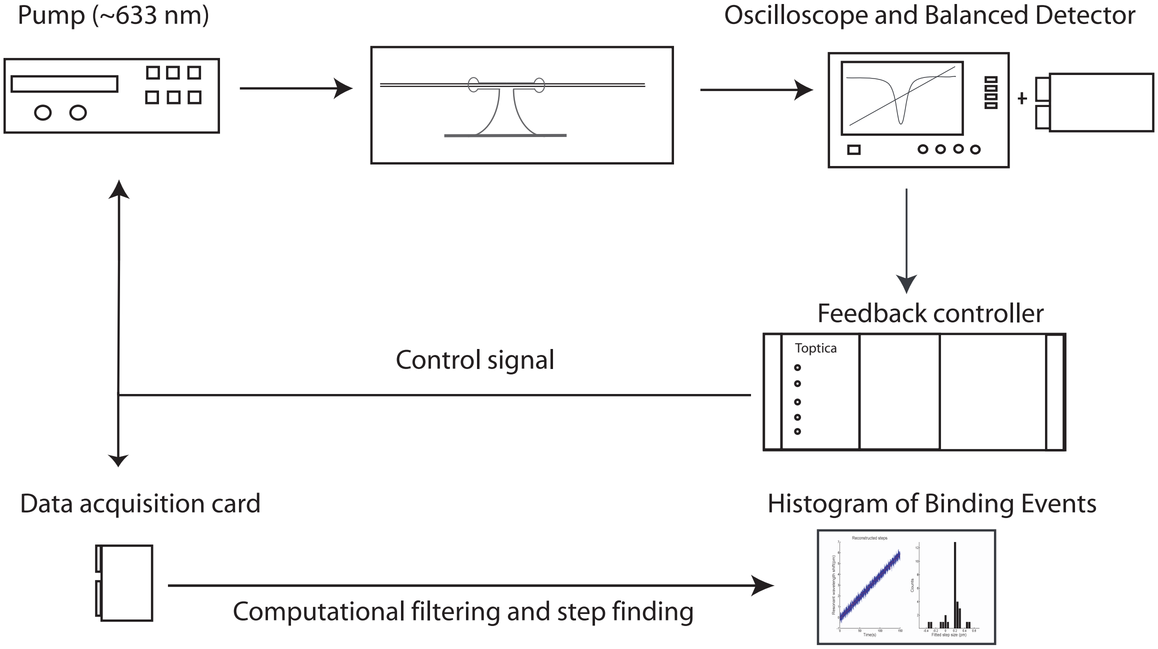

Figure 3.3: An overview of the frequency locking method for peak tracking. In this system, as opposed to continuously scanning through a range of wavelengths to locate the resonant wavelength of the microtoroid, a feedback controller continuously tunes the wavelength of the laser to the resonant wavelength of the cavity. By measuring the amount of voltage it takes to keep the wavelength of the laser matched to the resonant wavelength of the cavity, changes in resonant wavelength may be more accurately monitored.

may be determined by curve fitting to a Lorentzian using a custom-written LabVIEW program as shown in Figure 3.5.

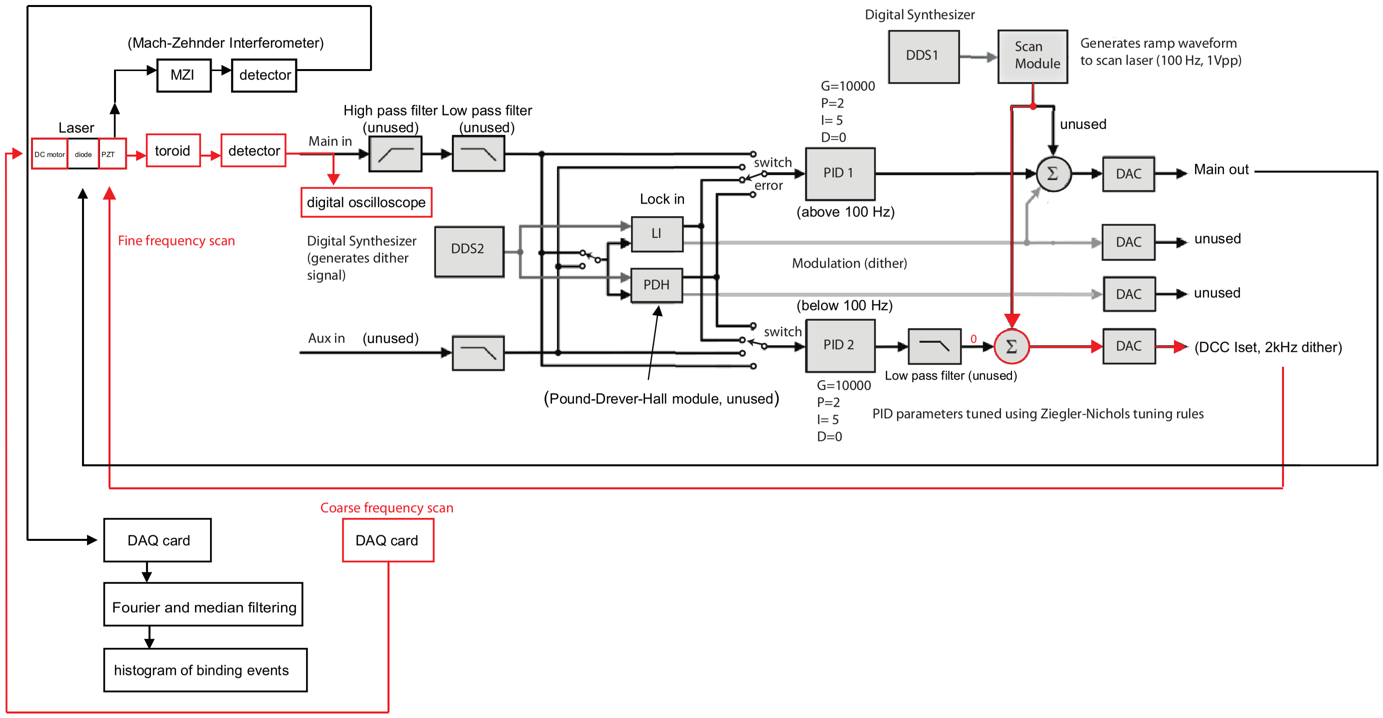

Figure 3.4: Block diagram of how a resonance peak is located (path shown in red).

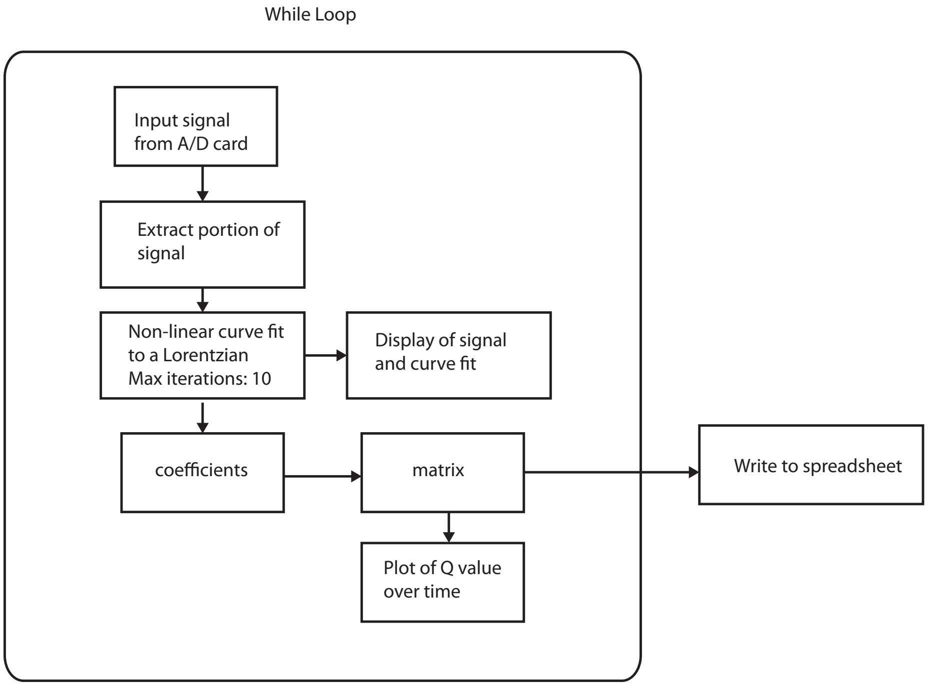

Figure 3.5: Sequence of operations how the quality factor of a microtoroid is measured over time.

After the peak is found, frequency locking is achieved using a lock-in regulator system (Digilock 110, Toptica Photonics). Briefly, a digital synthesizer generates a dither (sinusoidal external reference waveform) signal. This dither signal is sent directly to the laser diode which dithers the frequency over a small range around the resonance peak. This response is detected by a high speed auto-balanced photodiode (Nirvana, New Focus) and sent to a lock-in error signal generator which multiplies the modulated signal with the output from the photodiode to create an error signal. An explanation of why this generates an error signal is given in Section 3.3. The error signal which represents the difference between the laser frequency and the cavity resonance, is then minimized by being sent to two proportional-integral-derivative (PID) feedback controllers. The first controller handles fast (> 100 Hz) fluctuations while the second controller handles slow (< 100 Hz) fluctuations. These controllers attempt to match the laser frequency with the cavity frequency by outputting the appropriate voltage needed to minimize the error signal. This output voltage is converted to wavelength using a scaling factor determined by calibration with a home built Mach-Zehnder interferometer.

A general overview of the system is presented in Figure 3.6. Although the controller can output a dither signal up to 10 MHz, in the experiments presented in this thesis, a dither signal of 2 kHz was used. We note that the dither signal is removed in pre-processing and therefore does not limit the SNR of the system.

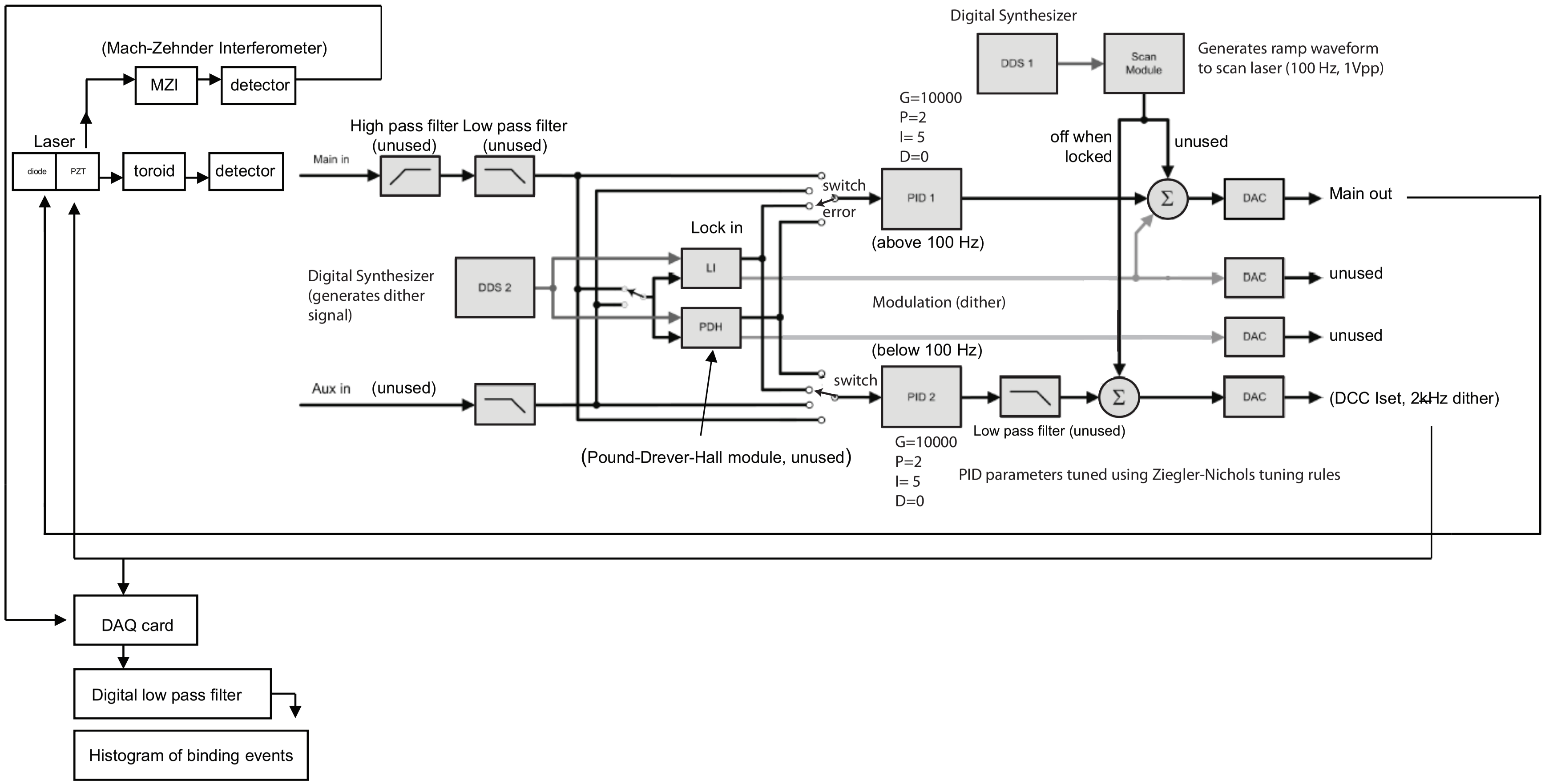

Figure 3.6: Block diagram of toroid control system.

3.3 Conceptual Model

An intuitive understanding of how the feedback controller generates an error signal that is sent to the laser controller may be seen in Figure 3.7. Because the resonance peak (given by $L(x) = \frac{1}{\pi}\frac{0.5\Gamma}{(x-x_0)^2+(0.5\Gamma)^2}$) of the microtoroid is symmetric it is difficult to know on what side of the peak the laser frequency is located. The derivative of the original signal, however, may be readily used to locate the center of the peak as it crosses zero at the center and is antisymmetric around the peak. This makes the derivative a good error signal for the feedback loop as if the laser is to the left of the peak the error is positive, and if the laser is to the right of the peak, the error is negative. Zero error is achieved at the top of the peak.

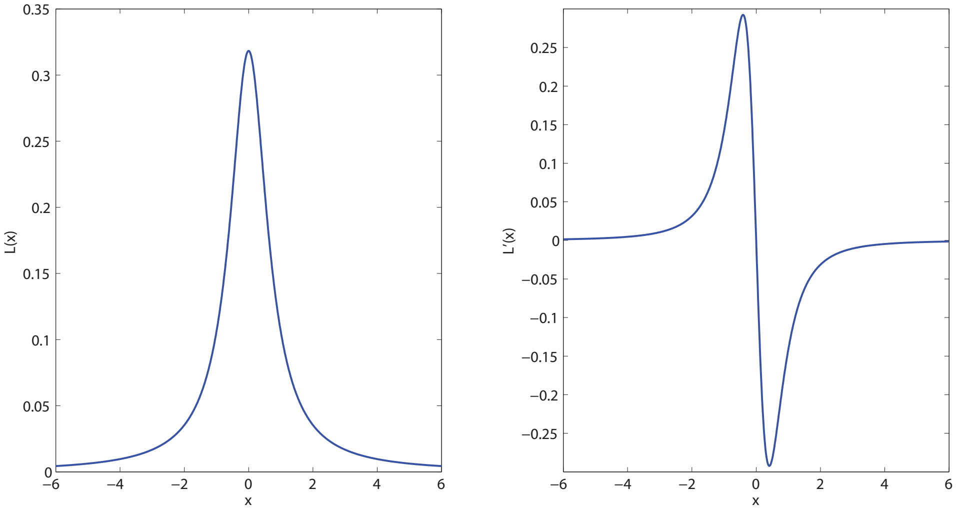

Figure 3.7: Lorentzian ($\Gamma = 1$) and its derivative. The derivative is antisymmetric about the peak

As shown in Figure 3.8, because the toroid response and the dither signal are in phase on the left side of the peak, the result of the demodulation (multiplying and taking the time average), is positive. On the right side of the peak, the toroid response and the dither signal are out of phase and so the error signal which is the result of the demodulation is negative.

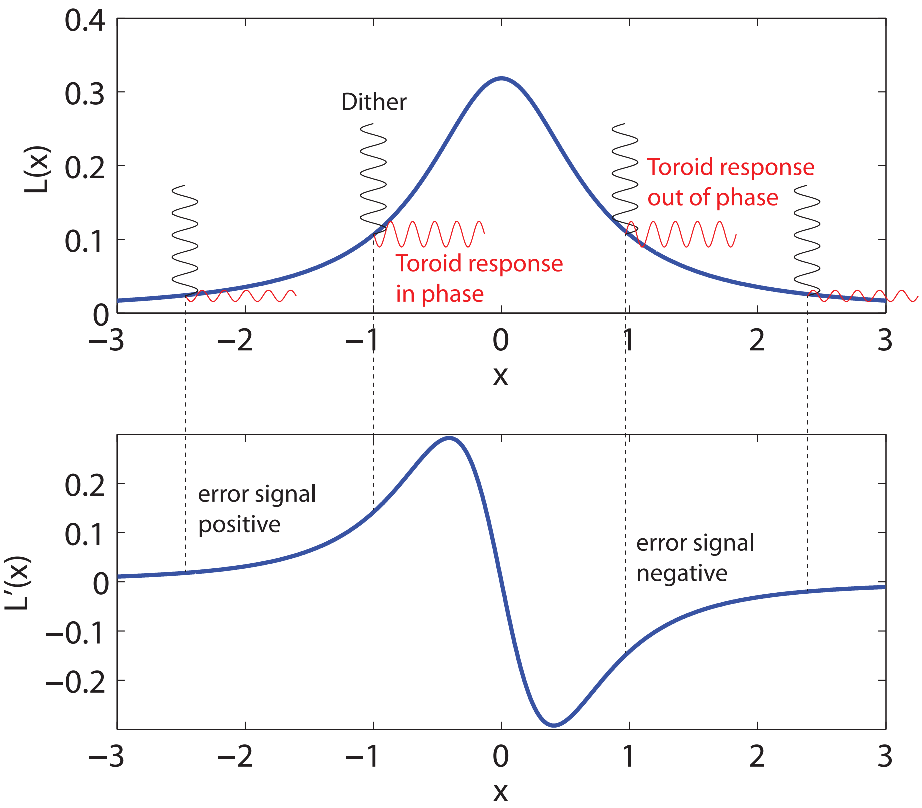

Figure 3.8: Conceptual basis for how the error signal is generated. Demodulating (multiplying and taking the time average) the dither signal with the toroid response gives the derivative.

3.4 Symbolic Model

We can show that the error signal is the derivative of the unmodulated toroid response as follows. Let $d(t) = \sin \omega(t)$ be the dither signal and $I = g(\lambda)$ be the toroid response to a given wavelength with units of intensity. Furthermore, for simplicity, assume λ is defined in a shifted coordinate system such that the peak is at $\lambda = 0$ as in Figs. 3.7 and 3.8. Assume the laser wavelength to be proportional to the controller output voltage signal: $\lambda = \alpha v_0(t)$ and $v_1(t)$ to be the signal measured by the photodiode: $v_1 = \beta g(\lambda(t))$, where β is the responsivity of the photodiode. The output voltage, $v_0(t)$ equals the dither signal plus the error signal or $d(t) + e(t) \Rightarrow v_o(t) = \sin \omega(t) + e(t)$.

$$\begin{aligned} v_1(t) &= \beta g(\lambda) \approx \beta \left[g(\lambda_0) + \left.\frac{\partial g}{\partial \lambda}\right|_{\lambda=\lambda_0} (\lambda - \lambda_0) \right] \\ &= \beta \left[g(\alpha \bar{v_0}) + \left.\frac{\partial g}{\partial \lambda}\right|_{\lambda=\alpha\bar{v_0}} (\alpha v_0 - \alpha \bar{v_0}) \right], \end{aligned} \tag{3.1}$$

where the central wavelength, λ_0, for the Taylor expansion was chosen to be $\alpha\bar{v_0}$, where $\bar{v_0}$ is the time average of v_0 over times somewhat longer than the period of the dither signal. The reason for this will become clear shortly. As $v_0(t) = d(t) + e(t)$, we have $\bar{v_0} = e(t)$.

The lock-in amplifier is designed to generate an error signal based on the time average of the product of the dither signal and the measured photodiode signal:

$$\begin{aligned} e(t) &= \langle d(t) \cdot v_1(t) \rangle \\ &= \left\langle sin\omega(t)\beta \left(g(\alpha e(t))) + \left.\frac{\partial g}{\partial \lambda}\right|_{\lambda=\alpha e(t)} \alpha \sin\omega \right) \right\rangle \\ &= \left\langle \beta g(\alpha(e(t))) \sin\omega t + \alpha\beta \left.\frac{\partial g}{\partial \lambda}\right|_{\lambda=\alpha e(t)} \sin^2 \omega t \right\rangle \\ &= 0 + \left\langle \alpha\beta \left.\frac{\partial g}{\partial \lambda}\right|_{\lambda=\alpha e(t)} \left(\frac{1}{2} - \cos 2\omega t \right) \right\rangle = \frac{1}{2}\alpha\beta \left.\frac{\partial g}{\partial \lambda}\right|_{\lambda=\alpha e(t)} \end{aligned} \tag{3.2}$$

Thus, the error signal generated by the lock-in amplifier is indeed proportional to the derivative of the unmodulated toroid response, $\partial g/\partial\lambda$.

3.5 PID Control

PID controllers are the most common feedback control system [65]. They are designed for a system to reach a setpoint as quickly as possible by outputting a control signal $u(t)$ based on the following three component algorithm:

$$u(t) = k_p e(t) + k_i \int_0^t e(\tau) d\tau + k_d \frac{de}{dt} \tag{3.3}$$

where, $e(t)$ is an error signal, and k_p, k_i, and k_d are tuning parameters that represent proportional gain, integral gain, and derivative gain, respectively. This is represented in block diagram form in Figure 3.9.

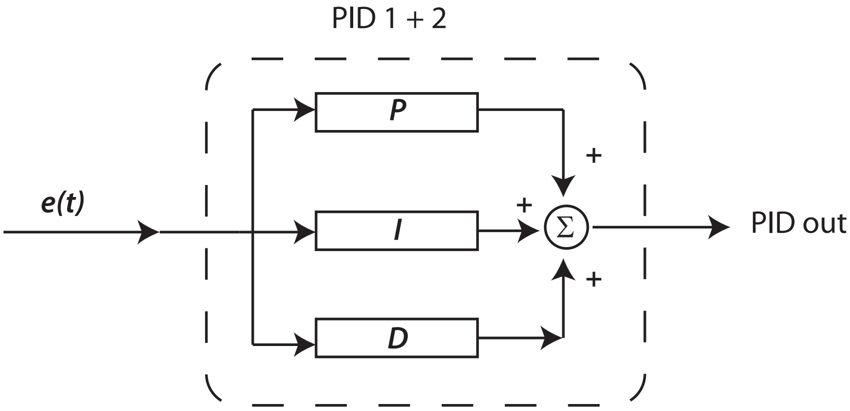

Figure 3.9: Block diagram of the PID feedback controller. The error signal from the lock-in regulator is sent to the PID controller. The contributions from the P, the I, and the D, components are multiplied by the error signal and summed to give a signal that causes the controller to reach its set point in a quick and stable way.

Proportional gain produces an output that is proportional to the error, integral gain produces an output that is proportional to the integral of the error and derivative gain produces an output that is proportional to the derivative of the error. In this way, proportional gain takes care of the present error, integral gain takes care of past errors, and derivative gain attempts to predict future errors through linear extrapolation by calculating a slope.

The values for the PID controllers are set by using a heuristic known as the Ziegler-Nichols tuning rules that help the system stabilize as quickly as possible. Essentially the overall gain of the controller is increased until the system oscillates. The gain at which this occurs is denoted as K_u and the period of oscillation of the system is denoted as T_u. The values for proportional gain, integral time, and derivative time are then given as follows: $k_p = 0.6K_u$, $k_i = 0.6K_u/(0.5T_u)$, and $k_d = (0.6K_u)(0.125T_u)$ [65]. The rise and settling times for our system were characterized by sending a step voltage to our laser piezo and were found to be on the order of ~ 0.5 and 1.5 ms, respectively.

3.6 Converting voltage to wavelength using a Mach-Zehnder interferometer

The voltage the feedback controller sends to the laser controller to adjust the wavelength of the laser may be converted to a wavelength using a calibration factor determined from the distances between fringes of a fiber Mach-Zehnder interferometer (MZI). A MZI was created by splitting the output of the laser into two paths using a 50/50 visible coupler (New Focus). A delay was added in one of the paths by adding an additional fiber that was several meters long. The output was recombined using another 50/50 coupler and sent to a photodiode whose output was displayed on an oscilloscope screen (Figure 3.10). As the laser frequency changes as the laser piezo voltage is being swept, the output of the MZI changes in a fringe sinusoidal pattern. One can compare how much voltage is put on the piezo with how the laser frequency changes by counting the fringes.

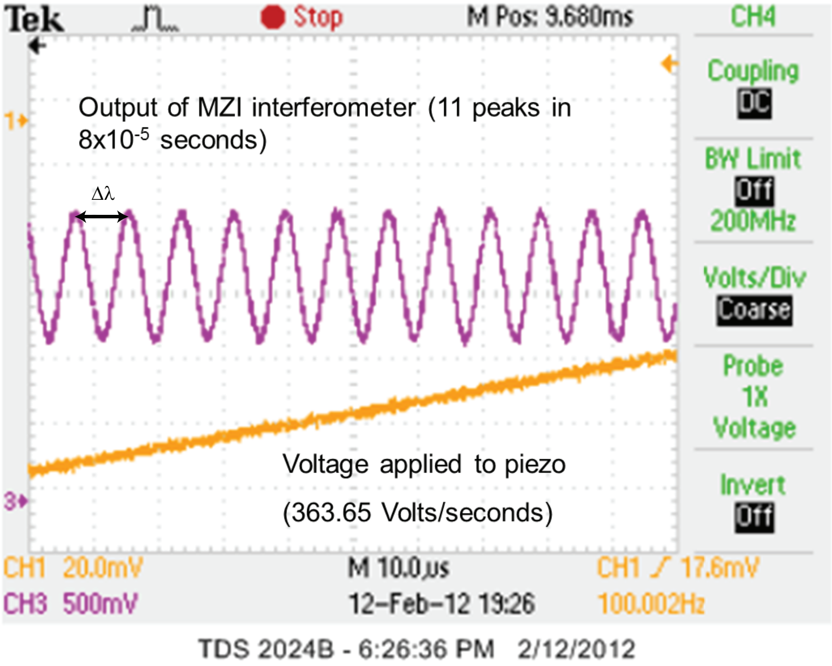

Figure 3.10: Interference fringes of the Mach-Zehnder interferometer displayed on an oscilloscope. A voltage to wavelength conversion factor for the laser was calculated by using a Mach-Zehnder interferometer as an accurate ruler. The Mach-Zehnder interferometer was constructed by combining the outputs of two optical fibers of different lengths. From the fringe spacing and physical properties of the interferometer, the frequency modulation of laser was calculated to be 0.031 nm/V.

The fringe spacing may be calculated as follows: Let Δz be the difference in length between the two fibers. A peak occurs if $\Delta z = N\frac{\lambda}{n}$, where N is an integer number, n is the fiber refractive index and λ is the free space wavelength of the light carried by the optical fiber. Therefore, the free spectral range is:

$$\begin{aligned} \Delta\lambda &= \lambda_N - \lambda_{N+1} \\ &= \frac{n\Delta z}{N} - \frac{n\Delta z}{N+1} \\ &= n\Delta z(\frac{1}{N} - \frac{1}{N+1}) \\ &= n\Delta z(\frac{1}{N^2+1}) \approx \frac{n\Delta z}{N^2} \end{aligned} \tag{3.4}$$

We can calculate N based on the approximate wavelength of the laser being used ($\lambda_N = 635$ nm):

$$N = \frac{n\Delta z}{\lambda_N}. \tag{3.5}$$

Therefore,

$$\begin{aligned} \Delta\lambda &= \frac{n\Delta z}{(\frac{n\Delta z}{\lambda_N})^2} \\ &= \frac{\lambda_N^2}{n\Delta z}. \end{aligned} \tag{3.6}$$

From Figure 3.10, the calibration factor $\frac{\partial\lambda}{\partial V} = \frac{\Delta\lambda}{\Delta V}$, where V is the voltage applied to the piezo. Using $\lambda_N = 635$ nm, $n = 1.6$ (optical fiber core) [66], and $\Delta z = 3$ meters, gives a $\Delta\lambda$ of 8.3×10^{-5}. Given that there are 11 peaks in 8×10^{-5} seconds (Figure 3.10), this gives a calibration factor of 0.031 nm/V.

3.7 Verifying peak tracking

We tested whether or not our system was adequately tracking the toroid resonance by turning on the viewing microscope lamp to heat the toroid (Figure 3.11). Because changes in temperature change the refractive index of the microtoroid and/or causes thermal expansion, the toroid's resonance frequency shifts upon heating from the lamp [67].

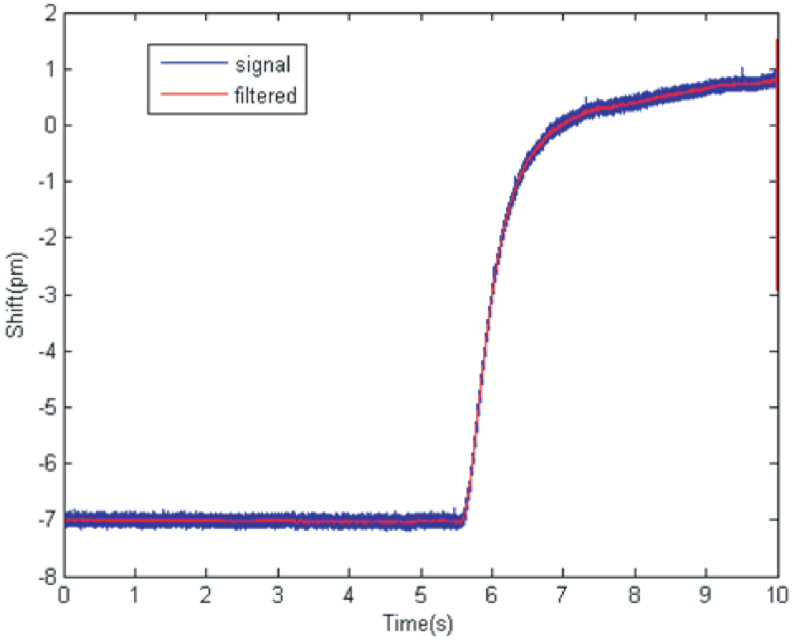

Figure 3.11: Tracking the resonance peak of the toroid in response to heating. As the toroid heats and the resonance peak location shifts, the controller outputs voltage to track the peak. Heating was applied using a microscope lamp. The lamp was turned on at 5.8 seconds.

To prevent resonance frequency shifts due to heating from the microscope lamp during experiments, a hot mirror that reflects infrared light back to the lamp, was added in the light path between both lamps and the microtoroid to minimize the heating effects noticed above.

3.8 Determining the noise level of our system

We calculate the noise level of our system before frequency locking was implemented to be ~ 1 pm (Figure 3.12). This was calculated by taking the standard deviation over 10 seconds of data after HEPES buffer was introduced to the system under stopped flow conditions. Our experimental system and conditions are described in more detail in 4.2.1. To computationally eliminate thermal drift from our calculation, we first fit a polynomial to our data and subtract it from our data before

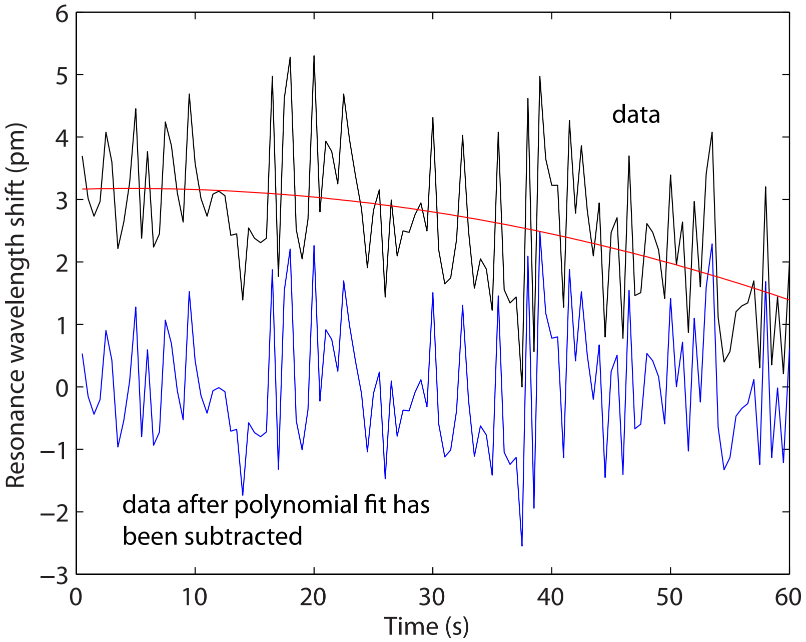

Figure 3.12: Noise level of system before frequency locking is implemented. The noise level was calculated from the RMS over 10 seconds of buffer data to be ∼ 1 pm.

calculating the standard deviation (Figure 3.12, red line). After frequency locking is implemented, we calculate the noise level of our system to be ∼ 0.07 fm (Figure 3.13). We calculate the standard deviation over 60s in Figure 3.12 and over 10s in Figure 3.13 because in older case, the sampling frequency was less due to a different data acquisition card and so we get better statistics sampling over a larger time scale. If we calculate the noise level (standard deviation) over 1 ms intervals which is the approximate time between binding events for our r = 2.5 nm nanoparticle experiments, this number reduces further to $\sim 9.6 \times 10^{-4}$ fm. This represents an average over 20 data points for 10,000 intervals. We note that the noise level decreases when averaging over smaller time intervals as our noise is not white noise. Before this number was calculated, we first computationally filter the data to remove known sources of noise and then apply a median filter of window size 1001.

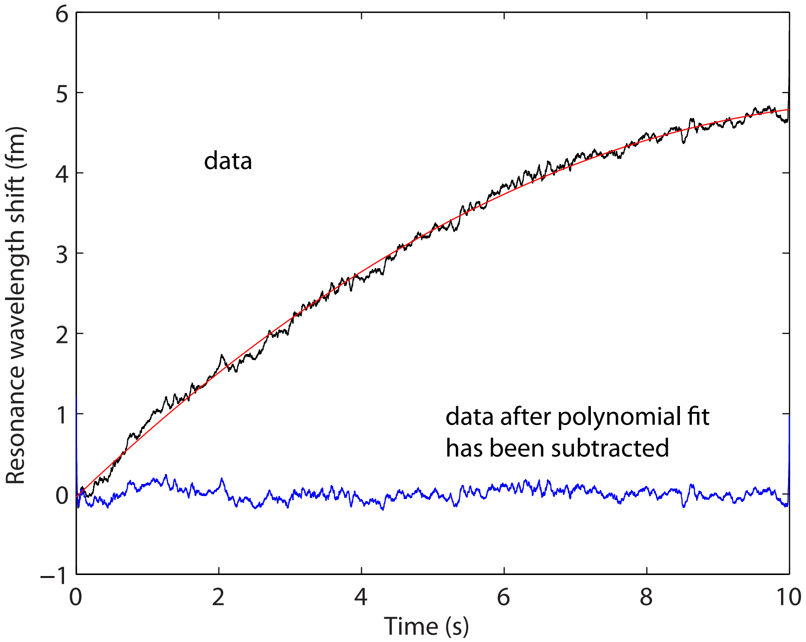

Figure 3.13: Noise level of system after frequency locking is implemented. The noise level was calculated from the RMS over 10 seconds of buffer data to be 0.07 fm. Over 1 ms this number reduces to $\sim 9.6 \times 10^{-4}$ fm.

3.9 Why does frequency locking enable the detection of smaller particles?

The primary reason that frequency locking enables the detection of smaller particles is because of its much faster time resolution (0.5 ms) compared to the temporal resolution of a conventional frequency-sweep method. This faster response time improves the detection method via multiple mechanisms:

1. Small particles have short residence times, requiring quick response. Because small particles experience greater Brownian forces, reduced van der Waals adhesive forces, and reduced optical trapping forces, they do not bind for long periods of time, but instead are rapidly ejected from toroid's evanescent field due to thermal fluctuations. For example, the $r = 2.5$ nm beads studied here bind for only 1.5 ms, on average. For a conventional frequency-swept system, it would be impossible to detect events this rapid, no matter how low its noise level.

2. Rapid response times reduce noise for moderate to long residence times/times between subsequent particles by permitting averaging or low-pass filtering of the data. For a step duration of time T, the uncertainty in the plateau height is proportional to $\sqrt{\tau/T}$, where τ is the response time. This reduction of error is analogous to the reduction in standard error of the mean when making multiple measurements of the same system.

3. The noise in our system is not white. Instead, as shown in the power spectrum resulting from a measurement of pure buffer solution (Figure 3.14), the noise amplitude is significantly greater at frequencies below 10 Hz than it is at frequencies between 10 Hz and 1000 Hz. (Note the spikes at frequencies greater than 10 Hz represent known narrow-band known noise sources, e.g., 60 Hz electrical noise and its harmonics, which we easily filter out and do not affect the ultimate noise level of our measurements.) The higher noise levels below 10 Hz likely stem from physical effects such as thermal drift, fluid convection, or environmental vibrations. By using a system that can identify events occurring more rapidly than 10 Hz, the low-frequency noise sources do not contribute significant error to our measurements, whereas they significantly impact slower frequency-swept systems. This reduces the relevant noise floor in our experiments, enabling the detection of smaller particles.

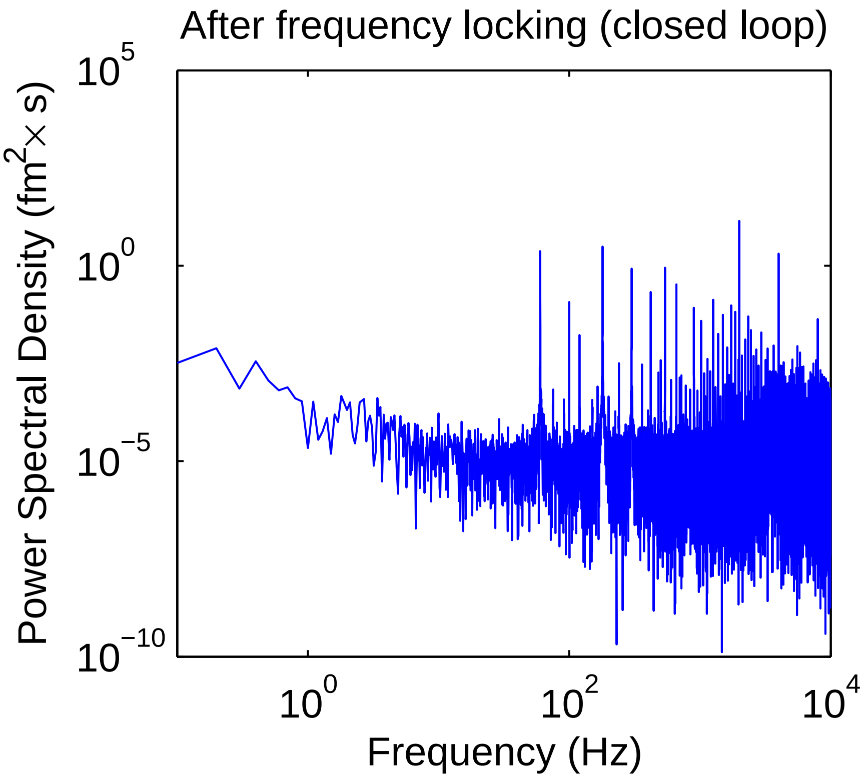

Figure 3.14: Noise level of system after frequency locking is implemented. The power spectrum of a typical buffer data set after the addition of feedback control. The tallest peaks correspond to known noise sources and their multiples.

3.10 Open and Closed Loop Laser Noise Analysis

In this section, we discuss efforts to analyze the noise present from the laser. Note that additional further post-processing is used to filter our data and further reduce noise levels.

From specifications given by the laser manufacturer, Figure 3.15, we estimate our laser frequency fluctuations to be $\sim$ 100 kHz when sampled at a repetition rate of 2 kHz. This corresponds to a noise level of 0.1 femtometers. This number is further reduced by post-processing to remove known sources of noise and a median filter. We note that longer PID integration times act as a filter to reduce noise, however, if too much of the signal is filtered, then locking cannot occur.

To more precisely analyze the noise present from the laser, one method would be to construct a fiber-based Mach-Zehnder interferometer, that converts frequency fluctuations to intensity fluctuations. To reduce intensity noise from the laser, one can monitor the output of the interferometer using a balanced detector, which subtracts out the noise due to laser intensity fluctuations. Therefore, the signal from the photodetector will represent the frequency response of our system without contamination from intensity noise from the laser.

We also provide a Bode plot (Figure 3.16) of our system when the laser is locked to a microtoroid. This gives the closed loop frequency response of our system. From Figure 3.16, we can see that our controller responds strongly to laser frequency fluctuations up to repetition rates of ∼ 2 kHz (controller bandwidth), while faster fluctuations cannot be accurately tracked. This shows that our controller stays locked up to a frequency of 2 kHz.

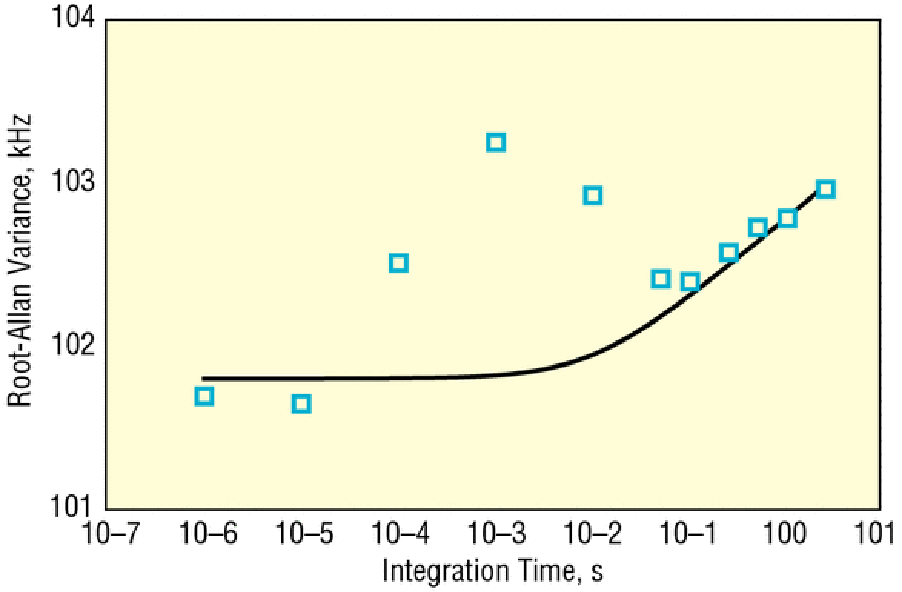

Figure 3.15: Laser linewidth as function of integration time. Here, integration time is the inverse of sampling frequency (repetition rate), and laser frequency fluctuations of ∼ 100 kHz correspond to wavelength fluctuations of ∼ 0.1 fm for our laser with wavelength ∼ 633 nm. Figure reproduced from New Focus Technical Note.

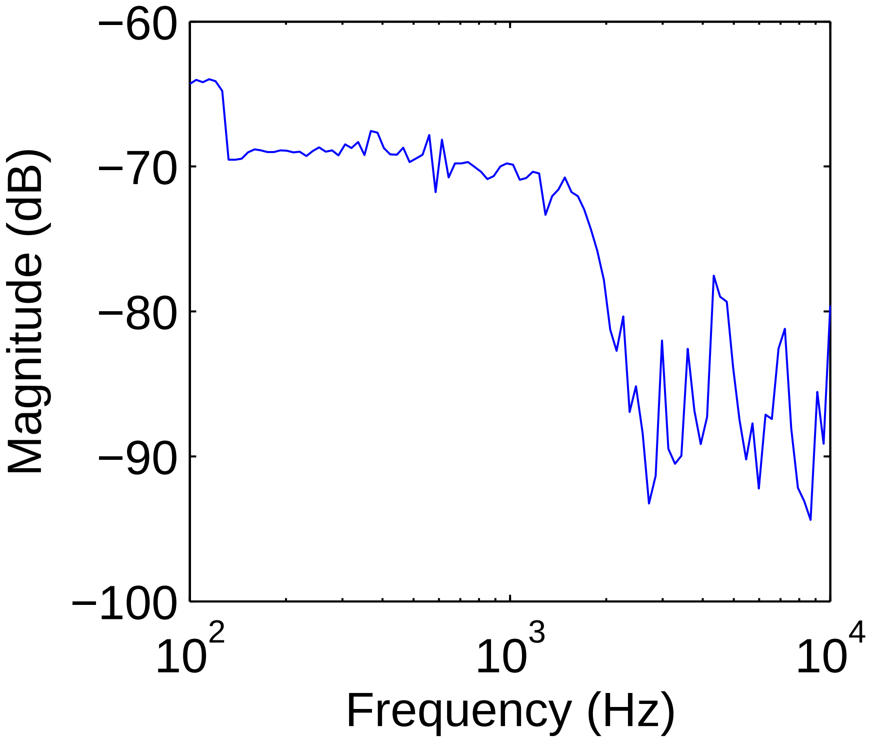

Figure 3.16: Bode plot of microtoroid frequency locked system. The system response drops at 2 kHz, which is the bandwidth of the system as determined by the dither frequency.

Chapter 4

System characterization

4.1 Data processing

4.1.1 Overview

Our data processing occurs in two main steps:

1. filter the data to reduce noise
2. find step (binding) events in our data using a step finding algorithm

In order to obtain the best approach for our system for our system we compared several methods. An overview of our approach is shown in Figure 4.1.

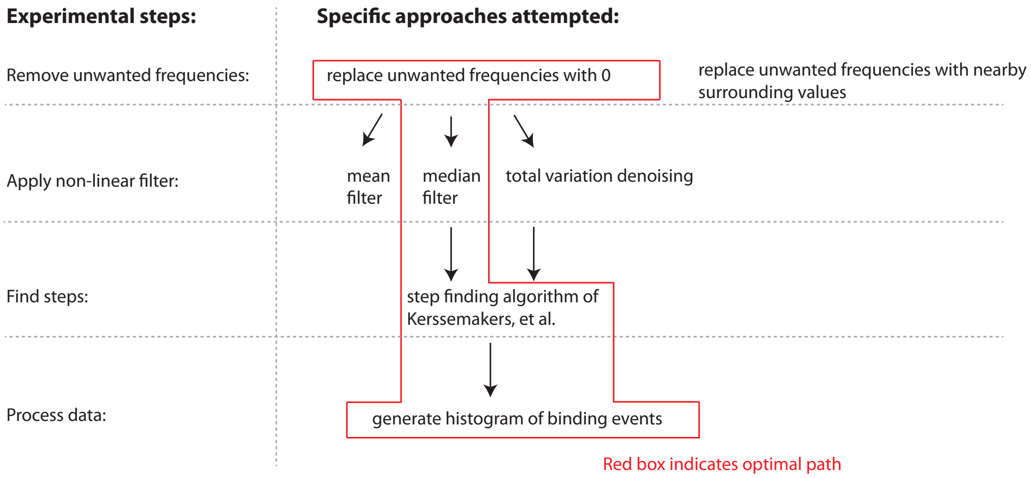

Figure 4.1: An overview of our data processing procedure representing all approaches tested. The optimal paths are shown inside the red box.

4.1.2 Filtering

We digitally filter our data to eliminate known sources of noise. We record the voltage of our feedback controller outputs at 20,000 Hz using a 24-bit National Instruments data acquisition card (NI-PCI-4461). The signal that we record is corrupted by the dither signal, which is at a frequency that we specify and so we may easily filter out. We accomplish this by taking the Fourier transform of the data in MATLAB (see Appendix A) and multiplying it with a matrix that is set to 1 for the values we wish to retain and set to 0 for the values we wish to discard. In this manner, we also filter out 60 Hz electronic line noise and all of its subsequent multiples (120, 180, 240, etc.) (Figure 4.2). We also remove 100 Hz as empirically it was found that the experiments in the lab had 100 Hz noise.

An example of our filtering procedure being performed is shown in Figure 4.3 which represents data from the selective binding of exosomes ($r \sim 20$ nm vesicles) to the microtoroid's surface. These experiments are discussed in more detail in Section 5.3. We pick exosomes to demonstrate our data processing technique as they are large biological molecules with clearly observable steps. We show that the same data processing works for smaller molecules in Section 6. The corresponding time trace for Figure 4.4 is shown in Figure 4.3. Note that while the individual steps appear flat they actually have a slight slope ($m = 0.38$ fm/s) (Figure 4.5(a)) that is the same order of magnitude as the slope seen in linearly filtered buffer data ($m = 0.16$ fm/s) (Figure 4.5(b)). A slope is present in the buffer (no molecule) data due to index of refraction changes caused by heating due to the resonant recirculation of light within the microtoroid [67].

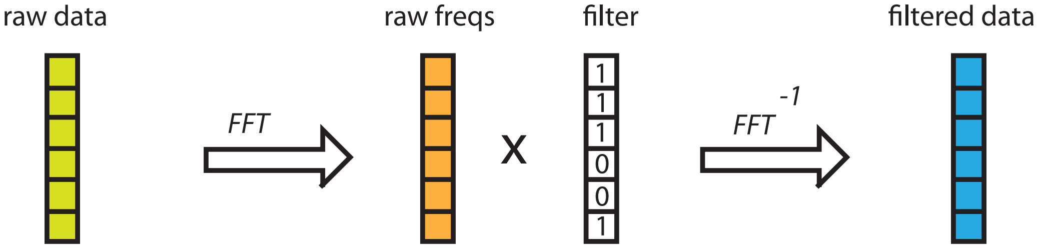

Figure 4.2: Filtering flow chart. Known sources of noise are computationally filtered out in the frequency domain. The × stands for element-wise multiplication.

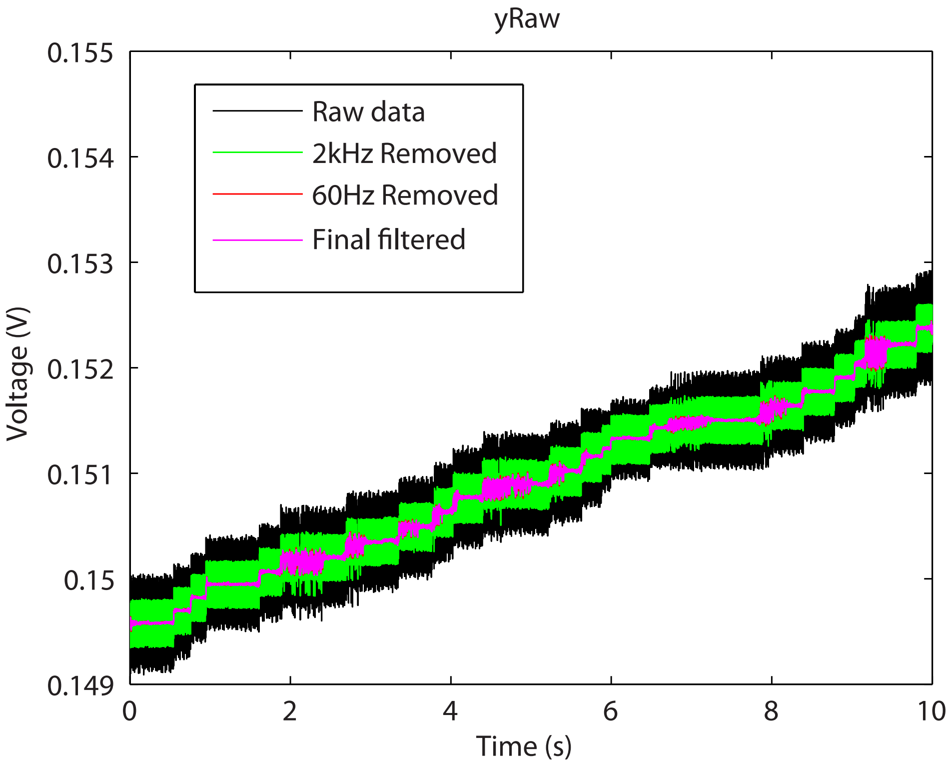

Figure 4.3: An example showing the effect of filtering on a raw data set (black). The data set represents the binding of exosomes to the surface of the microtoroid over a period of 10 seconds. Individual binding events cause a shift (seen as a step event) in the resonance wavelength of the microtoroid. The green trace shows the data after the 2 kHz dither signal has been removed. The red traces represents the data after 60 Hz electronic line noise and its multiples has been removed and magenta represents the final filtered data set.

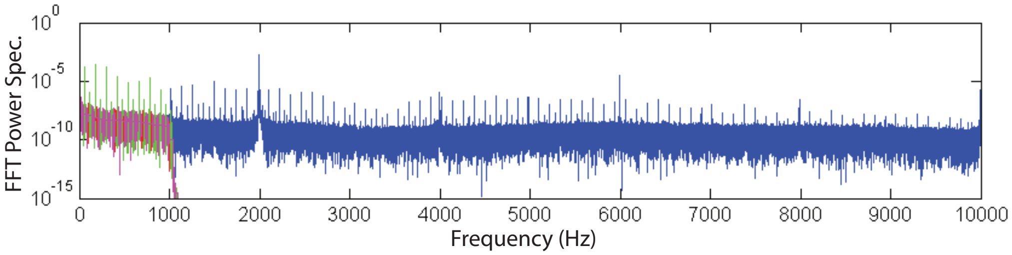

(a) Filtering a raw data set.

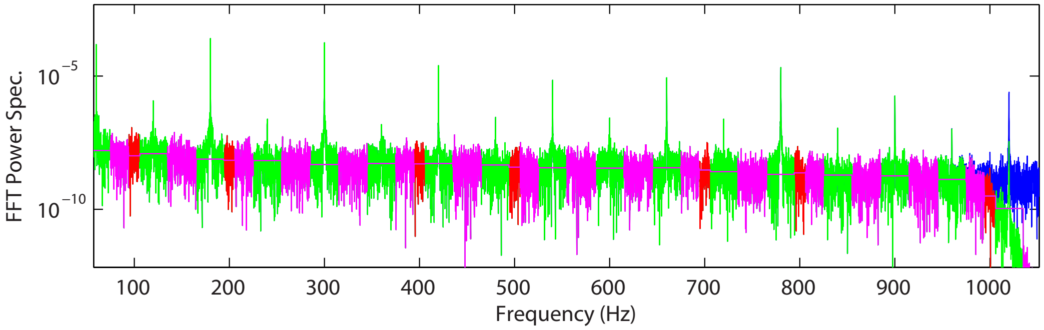

(b) Zoom-in of power spectrum.

Figure 4.4: Filtering a raw data set in frequency space. (a) The green trace shows the power spectrum of the data after the 2 kHz dither signal has been removed. Red represents the FFT after 60 Hz electronic line noise and its multiples has been removed, cyan shows the removal of 100 Hz multiples, and magenta shows the final filtered FFT. Multiples of 100 Hz were removed as it was empirically determined that experiments in the lab had noise at 100 Hz (b) A zoom-in of the power spectrum showing various filters being applied.

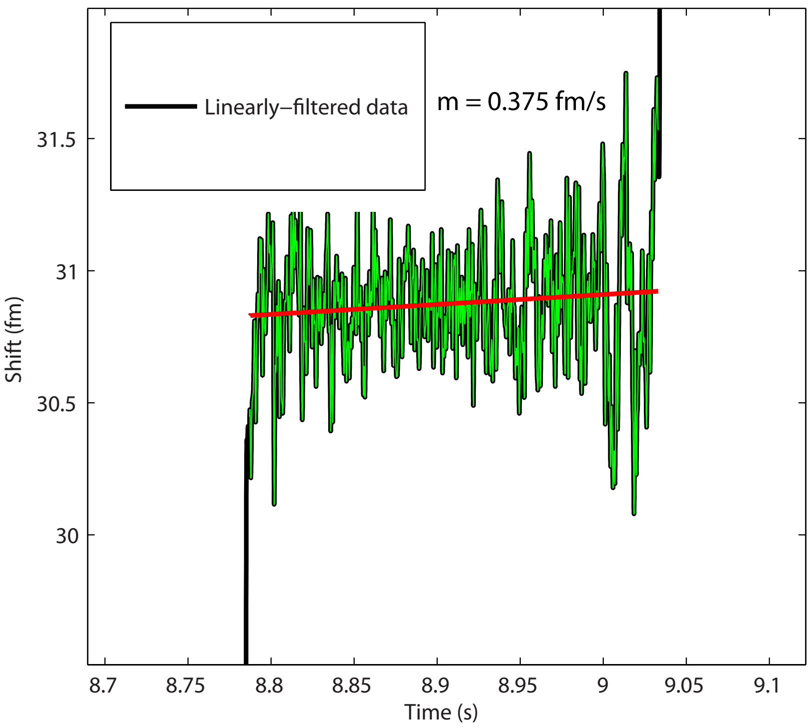

(a) The plateau region of the particle binding data in Figure 4.3 has a slight slope.

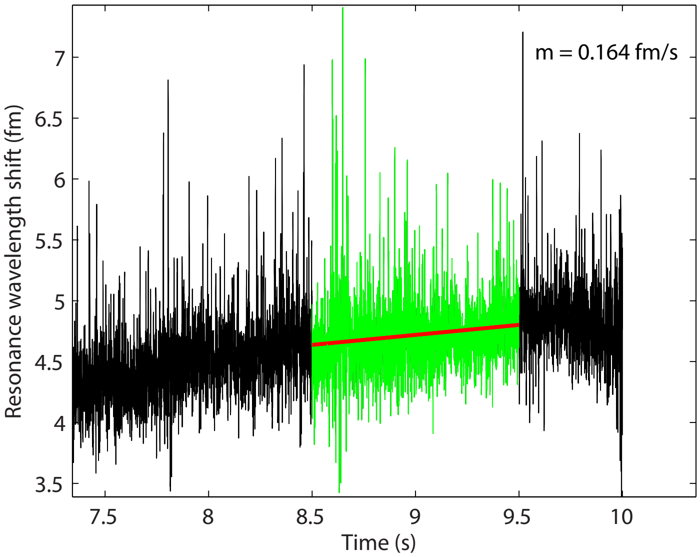

(b) Buffer (no molecule) data has a slight slope as well.

Figure 4.5: (a) Fitting a line (red) to the plateau of a step (particle binding event) demonstrates that the step has a slight slope, $m = 0.38$ fm/s, on the same order (3× different) as the slope seen in buffer data. Black represents linearly filtered data. The green is the fitted region. (b) The buffer data (no molecules) has a slight slope ($m = 0.16$ fm/s) due to index of refraction changes due to a temperature increase from the resonant recirculation of light. This slope is on the same order of magnitude as the slope we see in the plateau regions of our steps. The linearly filtered data is shown in black. The fitted region is green.

For comparison, we also tried replacing unwanted frequencies with values close to the local surrounding values as opposed to zero. An example of this filtering method being performed is shown in Figure 4.4(a). A more clear zoomed in inset of the filter is shown in Figure 4.4(b). A comparison between the final filtered data and the filtered data in Figure 4.3 may be seen in Figure 4.6. As shown in Figure 4.6, replacing unwanted frequencies with zero results in a cleaner trace.

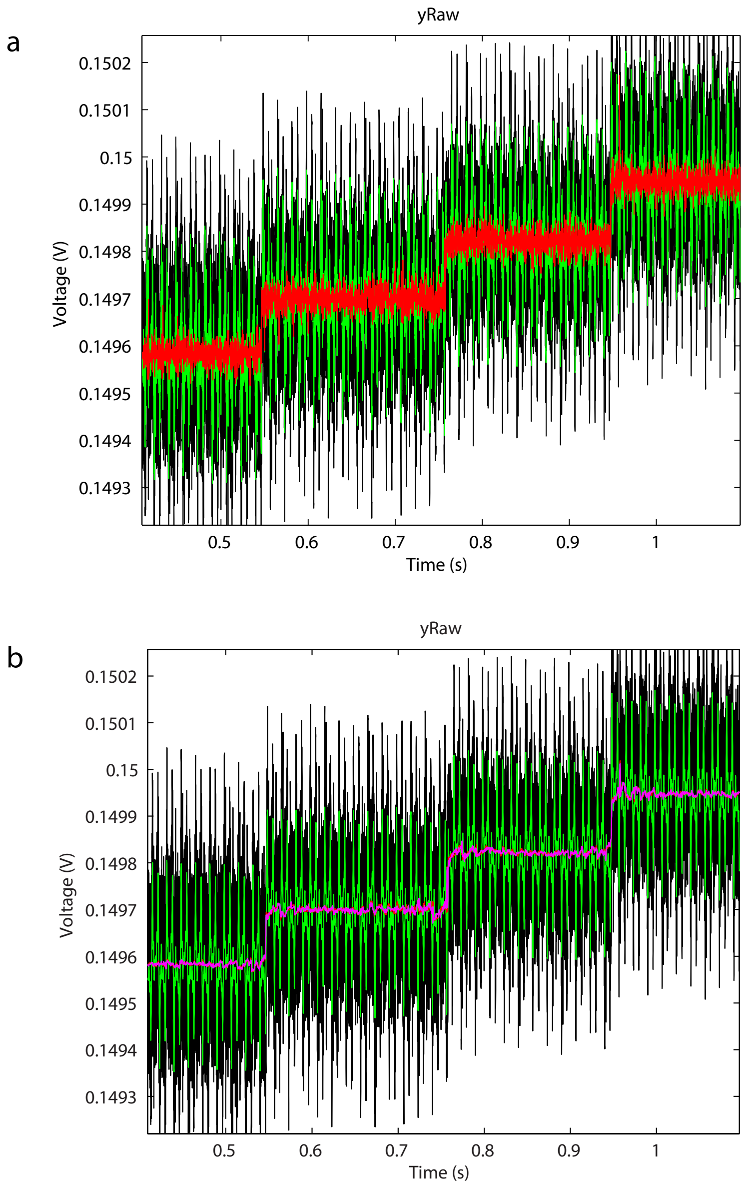

Figure 4.6: Zoomed in comparison between replacing unwanted frequencies with nearby frequencies (a) and replacing unwanted frequencies with zero (b). The green trace shows the data after the 2 kHz dither signal has been removed. Red represents the data after 60 Hz electronic line noise and its multiples has been removed, and magenta shows the final filtered data. Replacing unwanted frequencies with 0 results in better a signal-to-noise ratio.

4.1.3 Median filtering

After removing unwanted frequencies, we can further improve the signal-to-noise ratio by applying a median filter. A median filter takes a sliding window and replaces each data point with the median of the window. This method is often preferred over the moving average as the moving average may smooth out desired steps. To determine the optimal window size for our data, we experimented with several different window sizes. Figure 4.7 shows the data after applying the zero filter with median filters of varying window sizes applied. From Figure 4.7 we conclude that a window size of 1001 points (total data length is 200,000 points or 10 seconds) is optimal.

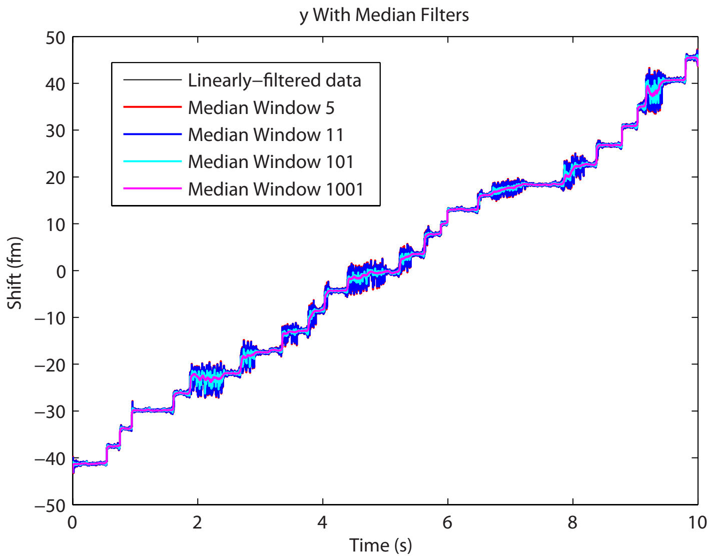

(a) Median filters of varying window sizes being applied to the data.

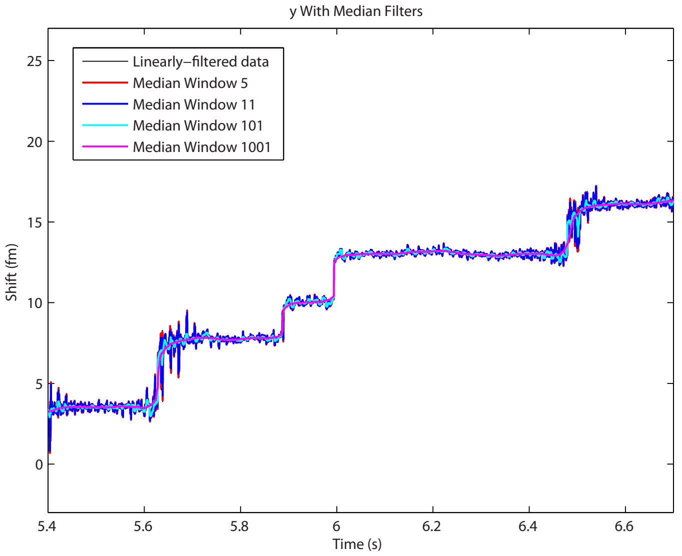

(b) A zoom in of median filters of different window sizes being applied

Figure 4.7: (a) Median filters of varying window sizes being applied to the data (b) A zoom-in of median filters of different window sizes being applied. From this graph, a window size of 1001 seems optimal.

Figure 4.8 shows an overlay of the linearly filtered data before and after the median filter with a window size of 1001 has been performed.

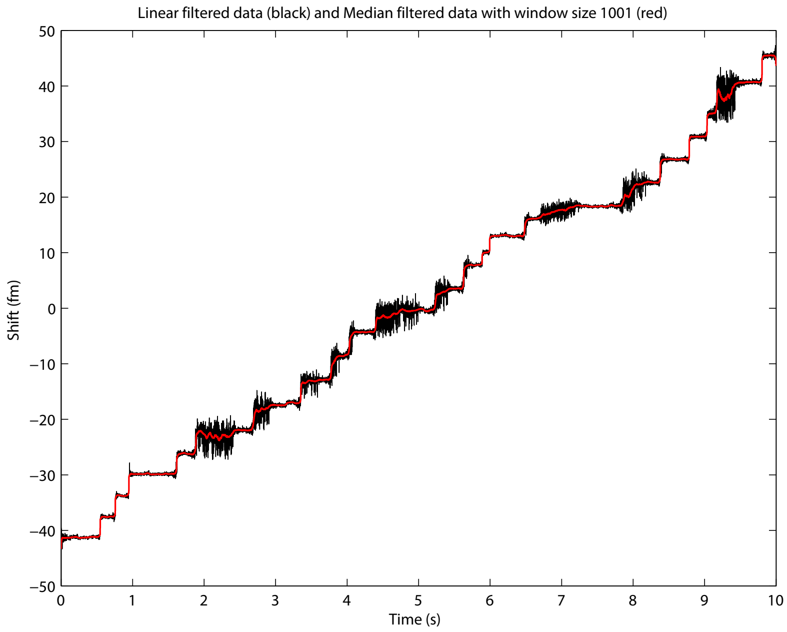

Figure 4.8: A time trace of the data after a median filter of 1001 points has been performed (red).

4.1.4 Total variation denoising

We also examined the effects of applying a noise removal technique known as total variation denoising (TVD) to our data. TVD is a signal processing technique developed by Rudin in 1992 [68] that has been shown to reduce noise while preserving sharp edges. The algorithm works by finding an approximate signal that is close to the original signal but with less variation (noise). TVD has been reported to be better at detecting step like events than either a mean or median filter [69].

In more detail, the algorithm minimizes the sum of two terms: (1) a measure of how close the approximate signal is to the original signal and (2) an expression for the variation. The variation $V(y)$ of a signal may be defined as:

$$V(y) = \sum_n \mid y_{n+1} - y_n \mid \tag{4.1}$$

One measure of how close an approximate signal (y_n) is with the data trace (x_n) is the sum of square errors between the two:

$$E(x, y) = \frac{1}{2}\sum_n (x_n - y_n)^2 \tag{4.2}$$

The sum of these two may be written as:

$$E(x, y) + \lambda V(y) \tag{4.3}$$

where λ is a user-defined parameter known as the regularization parameter that affects that amount of denoising that occurs. If λ is too small, no denoising will occur, however, if λ is too large, a flat line will result (i.e., variation will be minimized, but the approximation signal will look nothing like the input signal). The goal of TVD is to find a y_n such that Equation 4.3 is minimized. For our work we use code provided by Max Little [69]. Figure 4.9 shows the same data as before processed using TVD as opposed to a median filter. Different values of the regularization parameter λ were run to determine the optimal λ. As shown in Figure 4.10 a λ of 5×10^{-4} is the best. Figure 4.11 shows the entire time trace with only λ of 5×10^{-4}. Comparing the results of TVD with that of the median filter Figure 4.12, it appears as though the median filter gives slightly better performance.

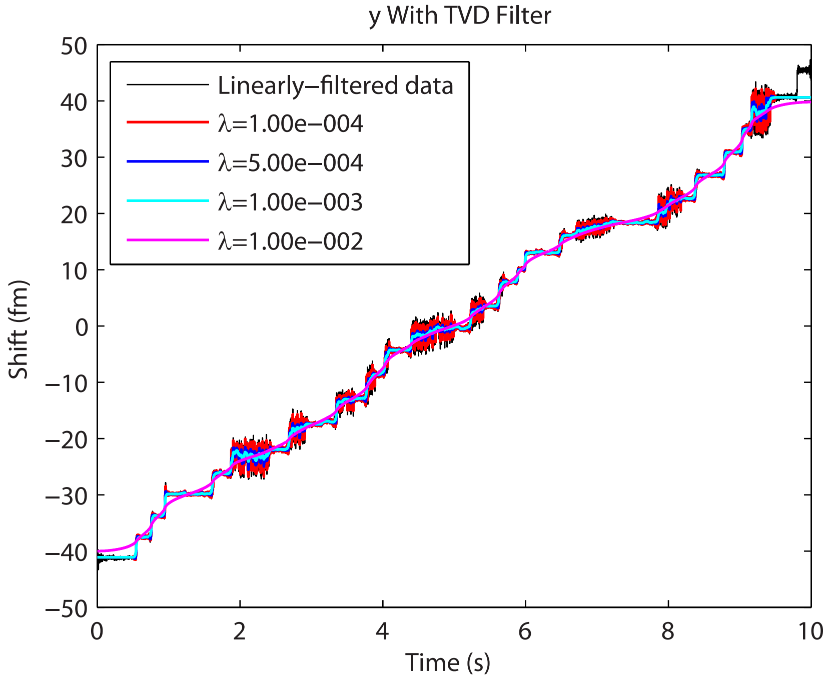

Figure 4.9: Total variation denoising algorithm run for a variety of different λ. The data was only fit from 0.5 to 9.5 seconds because Gibbs phenomena (ringing artifacts seen at discontinuities when a Fourier transform is taken [70]) at the beginning and the end interfered with the total variation filtering.

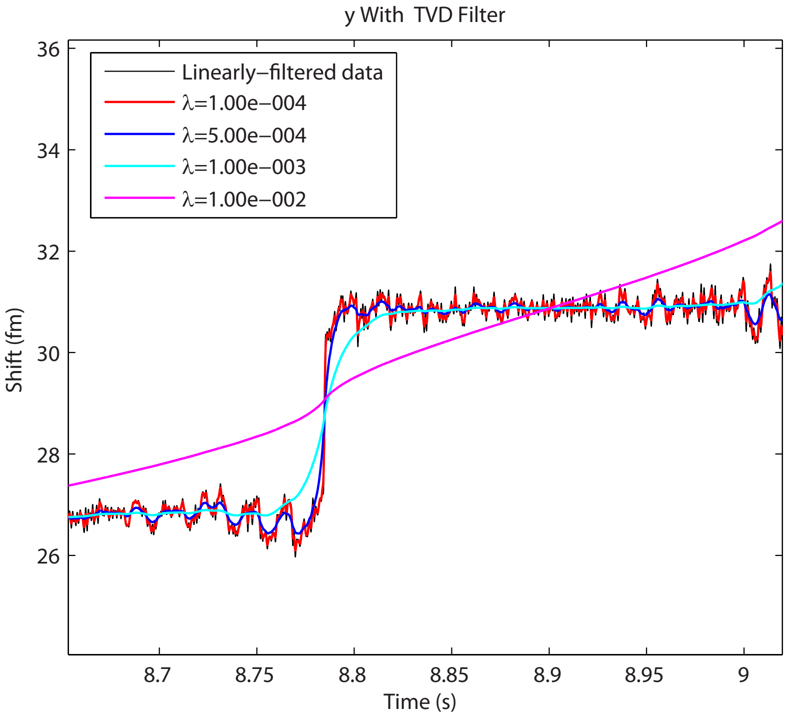

Figure 4.10: Raw data (black) of the resonance wavelength shift of the microtoroid over time as particles bind superimposed with the results of running the total variation denoising algorithm for a variety of different λ (shown in different colors). λ is a free parameter that determines how much denoising occurs. From the graph one can see that a λ of 5×10^{-4} most effectively minimizes the noise within the plateau of the step while preserving the step edge.

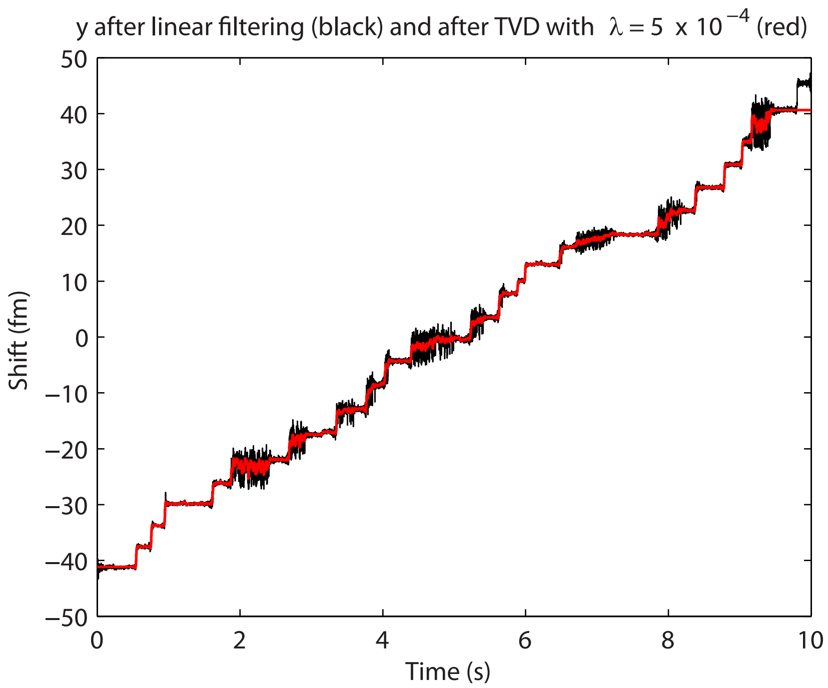

Figure 4.11: Total variation denoising algorithm shown with only λ of 5×10^{-4}.

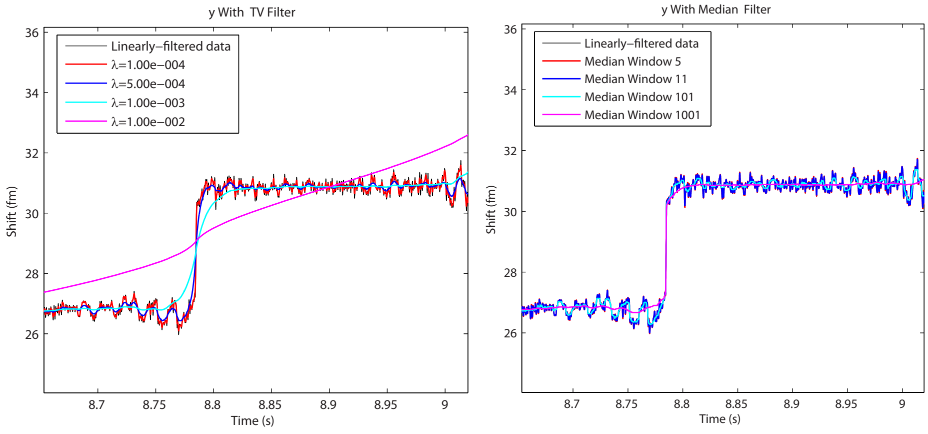

(a) (b)

Figure 4.12: A comparison of TVD results (a) with median filter results (b) The median filter gives slightly cleaner steps.

4.1.5 Step finding

4.1.5.1 Step finding algorithm

To determine step height, duration, and location in an un-biased manner, we used the step-finding algorithm of Kerssemakers, et al., [71] that was originally developed to examine the step-like elongation dynamics of microtubules. In comparisons of step-detection methods, this algorithm performs better than most other common methods in terms of percent found and percent correct steps [72]. The algorithm works by first fitting one large single step to the data and then fitting another step to the plateau of the first step. The size and location of this step is based upon minimizing the χ^2 goodness of fit value between the step and the original data. The χ^2 value is defined as:

$$\chi^2 = \sum \frac{(O - E)^2}{E^2}, \tag{4.4}$$

where O is observed value or the original data and E is the expected value of the step [73]. Steps are then fit to each of the plateaus of the new step, and the process known as splitting continues for a large number of user specified steps (generally around 200). For each of these splits, the size and location of the steps are determined by again minimizing the χ^2 goodness of fit value between the steps and the data. After this χ^2 goodness of fit value is calculated, false steps are fit in between the step locations and another χ^2 value is calculated for these steps. If the original steps are false, the χ^2 value for both the first set of steps and the second, false set (or counter fit), would be equivalent, i.e., their ratio would equal one. This is what occurs for a line with noise, but no underlying steps. If, however, the original steps are true, the χ^2 value of the first set of steps would be less than the χ^2 value for the false steps, and their inverse ratio would be greater than one. For each 'split' of the data, this χ^2 ratio is calculated and plotted. The split with the highest χ^2 ratio corresponds to number of steps that most accurately fits the underlying data. This process is outlined in Figure 4.13 and Figure 4.14. As shown in Figure 4.13 there is good concurrence between the final step fit and what a human operator would call by eye.

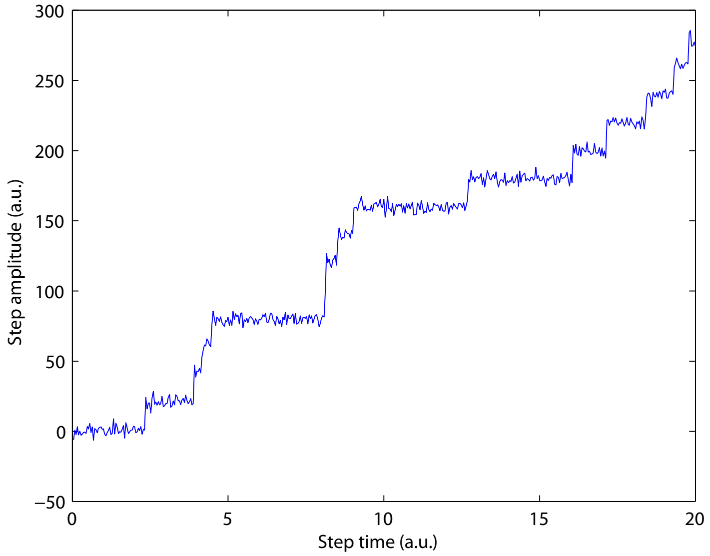

(a) Simulated data with random Gaussian noise of σ=3

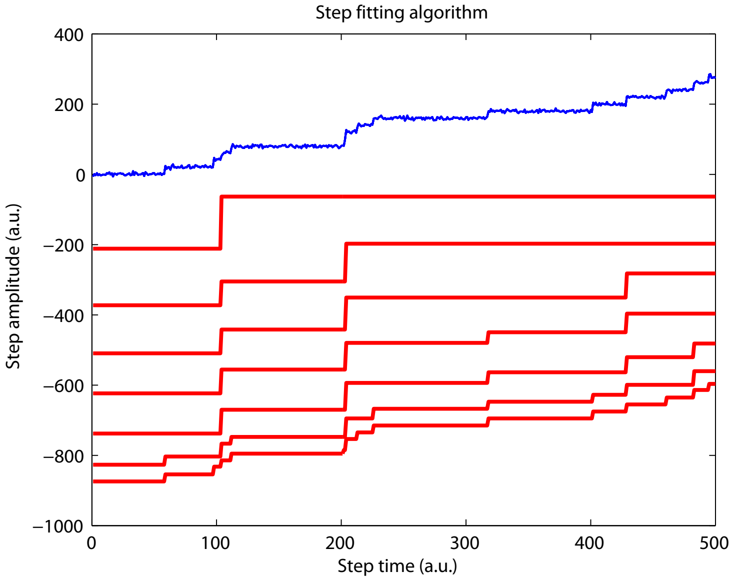

(b) The 'splitting' procedure. The data is first split into one large step. Steps are then fit to the plateau of the initial step. At each iteration a chi-squared value is calculated.

Figure 4.13: Outline of step fitting algorithm. Throughout the figure simulated data (blue) is used.

4.1.5.2 Discussion

We present the step traces (Figure 4.15) and their corresponding histograms for linearly filtered (Figure 4.16), median filtered, (Figure 4.17) and TVD filtered (Figure 4.18) data. Figure 4.19 shows the TVD data shown in Figure 4.18 with a Gaussian function (red) overlay. For each filtering type,

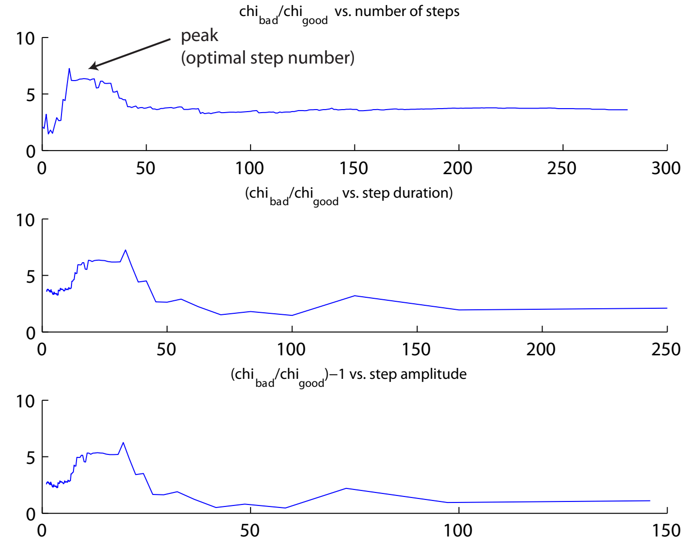

(c) Chi-squared values are calculated and plotted for a large range of step numbers. The peak occurs at the optimal value or in this case for 13

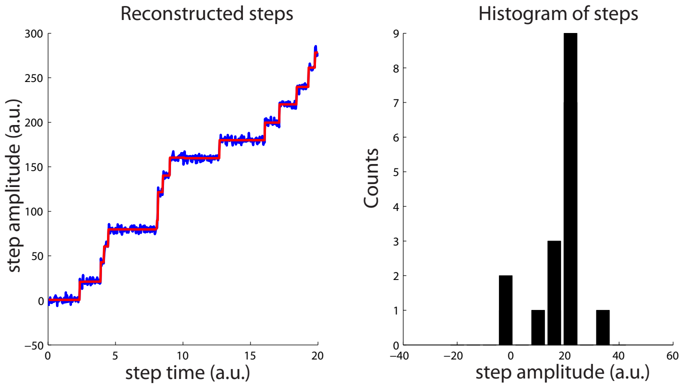

(d) The program is re-run using the optimal number of steps as the step guess and a histogram is created.

Figure 4.14: Outline of step fitting algorithm (cont'd).Throughout the figure simulated data (blue) is used.

several initial step guesses are shown. As seen in Figures 4.16, 4.17, and 4.18, the step finding algorithm does a good job in picking out steps even in just the linearly filtered case. In all three figures, the peak location remains roughly the same, however, the peak appears strongest with the TVD. This is good evidence that steps are not being artificially created by any of these filtering methods.

'Steppedness' curves as a function of step number are presented in Figure 4.20. Figure 4.21, shows ‘steppedness’ curves as a function of step duration. As shown in Figure 4.21, the step duration number remains the same, however, the χ^2 ratio which is a measure of how statistically significant the data is highest for the median filter. The same effect may be seen when looking at the ‘steppedness’ curves for step amplitude (Figure 4.22). We present the step fit with an initial guess of 60 steps for the TVD filtered data in Figure 4.15(a). A larger initial step guess ensures that all the steps are captured. The steps fit the data with a approximately $\sim 90\%$ accuracy compared to what a human operator would call by eye. Looking at the step fit for the median filtered data (Figure 4.15(a)), we see that although the step fit (red line) does not appear to follow the data as well as in the TVD case, the two step fits are very similar. Figure 4.15(c) reinforces the notion that the step finding program works reasonably well even in the case of the data being simply linearly filtered (unwanted frequencies removed). Although there is a greater number of spurious steps, the histogram peak location remains the same as in the median and TVD filtered data. For comparison purposes, we present the results of performing the step finding algorithm on buffer data (no molecules) in Figures 4.23 and 4.24. As shown in Figure 4.23, there is not really a clear peak in the step fit plot, indicating a low step fit value and therefore probability that statistically significant steps exist. This may be also be seen when the algorithm is run on just a sloped line with simulated noise (Figures 4.25(a) and 4.25(b)). For consistency, the sloped line with noise was processed using the same linear and median filtering procedures as actual data. We note that we for comparison with theory, we are concerned only with the maximum step amplitude [18].

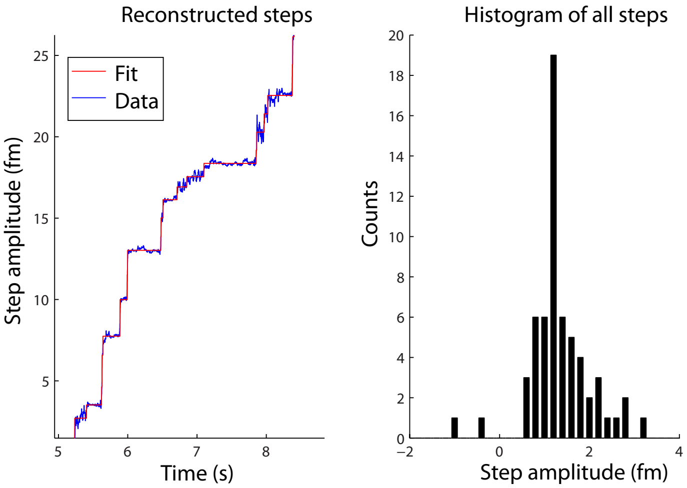

(a) Step fit after applying TVD filter.

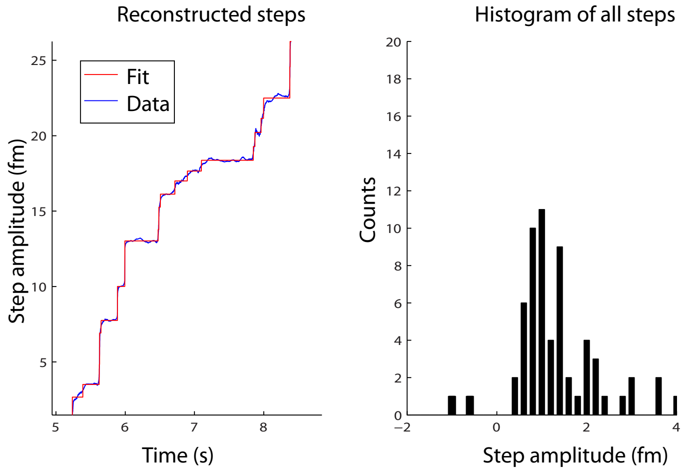

(b) Step fit after applying median filter.

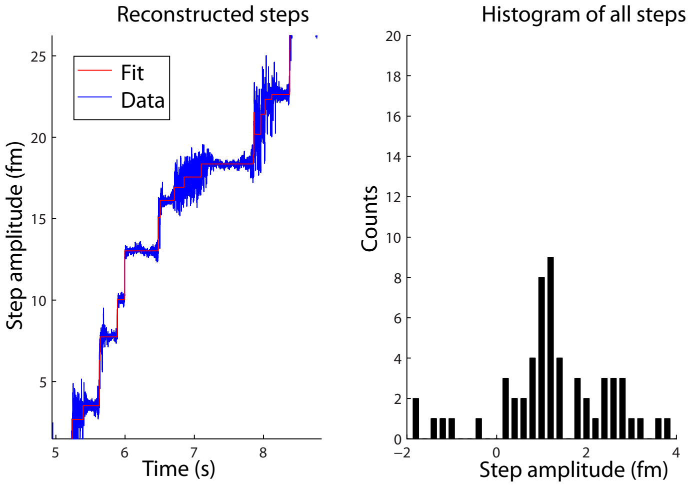

(c) Step fit after applying linear filter.

Figure 4.15: (a) Step fit and corresponding histogram after applying TVD filter (red) fit (blue) data. (b) Step fit after applying median filter and corresponding histogram (c) Step fit and corresponding histogram after applying just a linear filter (removal of known sources of noise without applying subsequent median or TVD filters). Although the step-fit less accurately predicts step location and height as only the first step of our data processing procedure is being performed, the maximum step amplitude is similar to what is seen in (b) indicating the robustness of the median filtering approach.

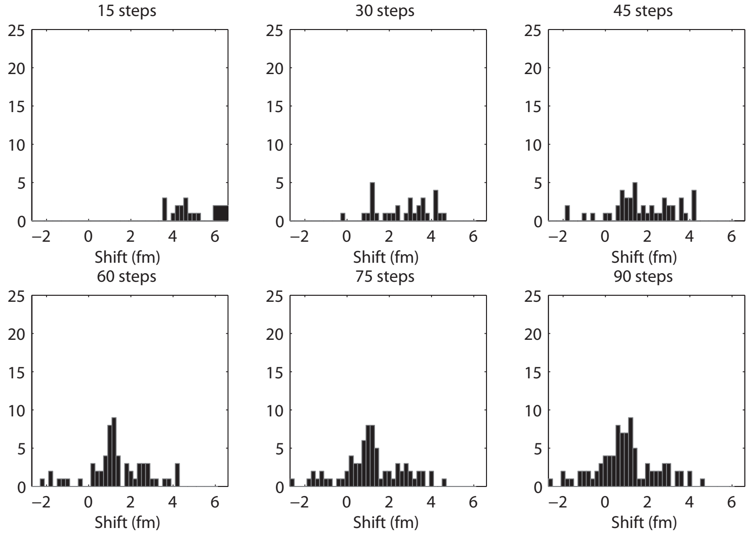

Figure 4.16: Histograms created from data processed with just a linear filter (replacing frequencies with zero). For different initial step guesses, the maximum step amplitude of each histogram is similar to the maximum step amplitude of the histograms from Figure 4.17 (data that has additionally been median filtered). This shows that the maximum step-height value is robust to the filtering method.

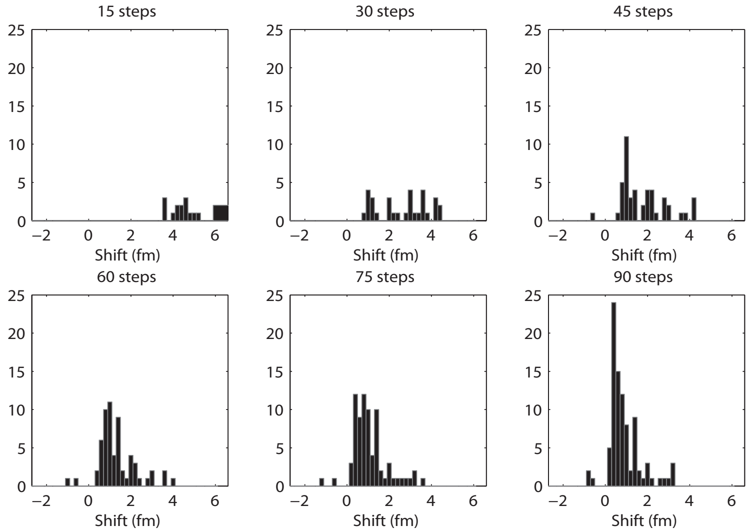

Figure 4.17: Histograms created from data processed with a median filter.

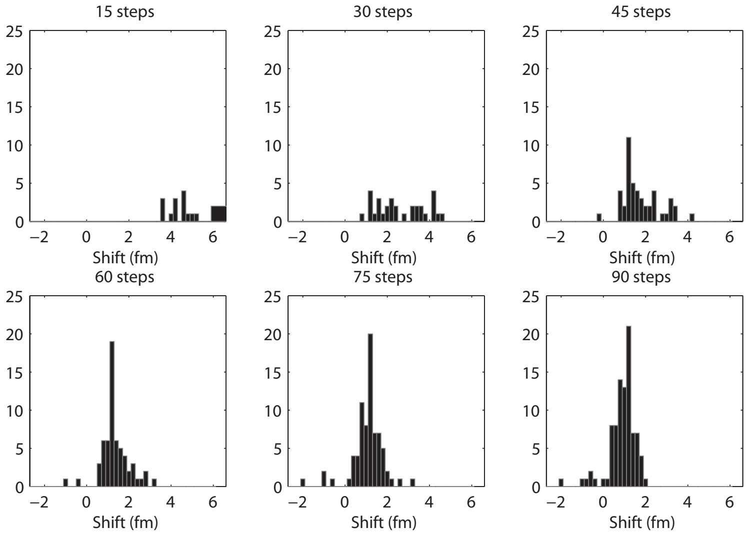

Figure 4.18: Histograms created from data processed with a TVD filter.

Table 4.1: Maximum step amplitude histograms

Initial Step Guess	Max. step amp., median filter hist. (fm)	Max. step amp., TVD filter hist. (fm)
45	4.2	4.2
60	4	3.2
75	3.6	3.2
90	3.2	2

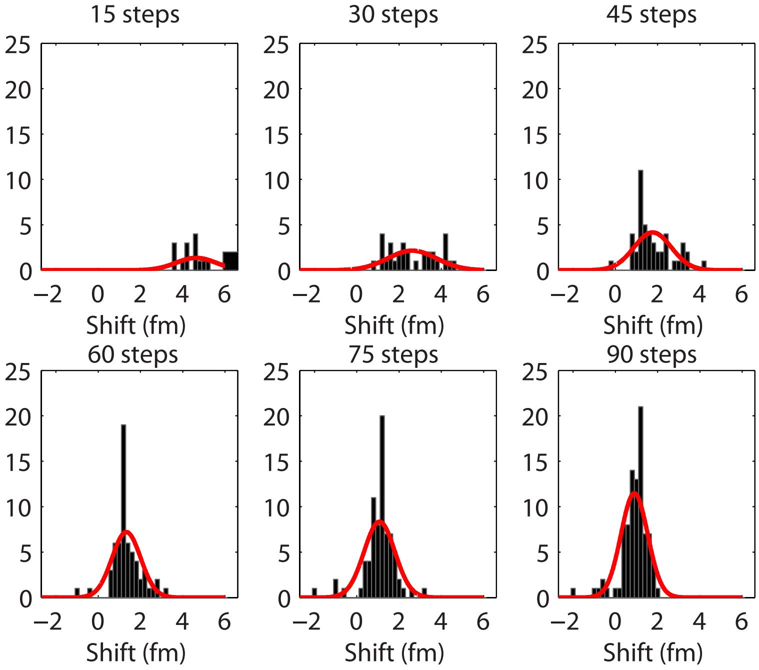

Figure 4.19: TVD histograms with Gaussian curve overlays.

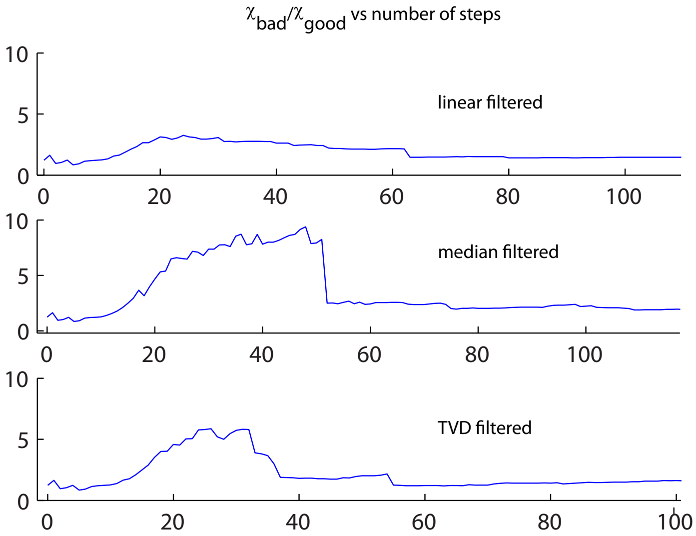

Figure 4.20: Step number step fit quality curves for linearly, median, and TVD filtered data. A peak is still present for the linearly filtered data, however, it becomes much sharper with the TVD filtered data.

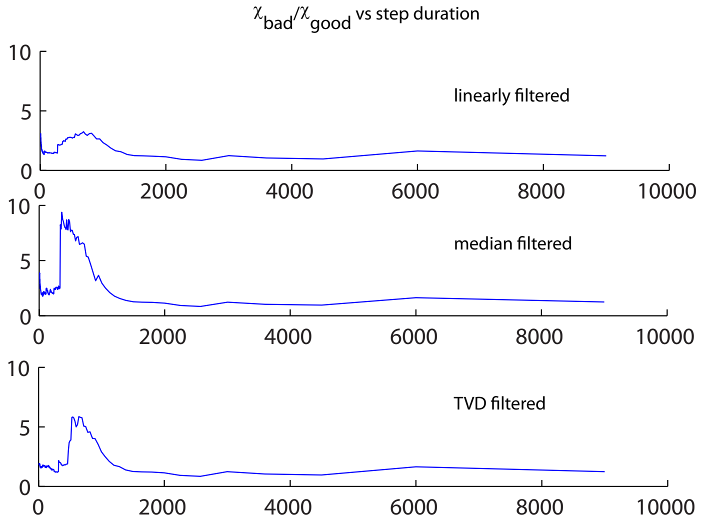

Figure 4.21: Step fit quality curves for linearly, median, and TVD filtered data with x-axis being step duration.

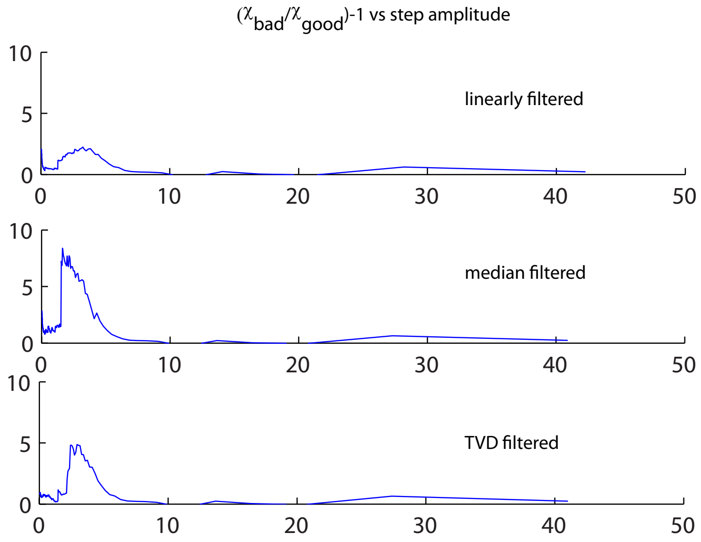

Figure 4.22: Step fit quality curves for linearly, median, and TVD filtered data with x-axis being step amplitude.

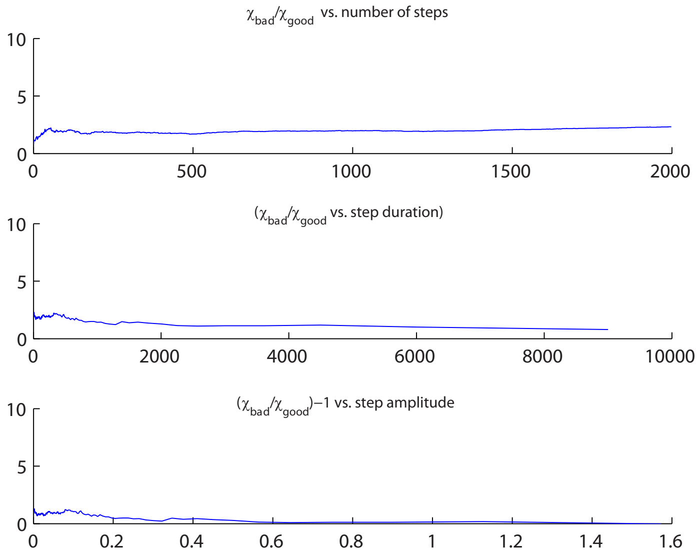

Figure 4.23: Step fit quality plot for pure buffer (no molecules) data. A low value for the step fit, indicates low probability that steps exist.

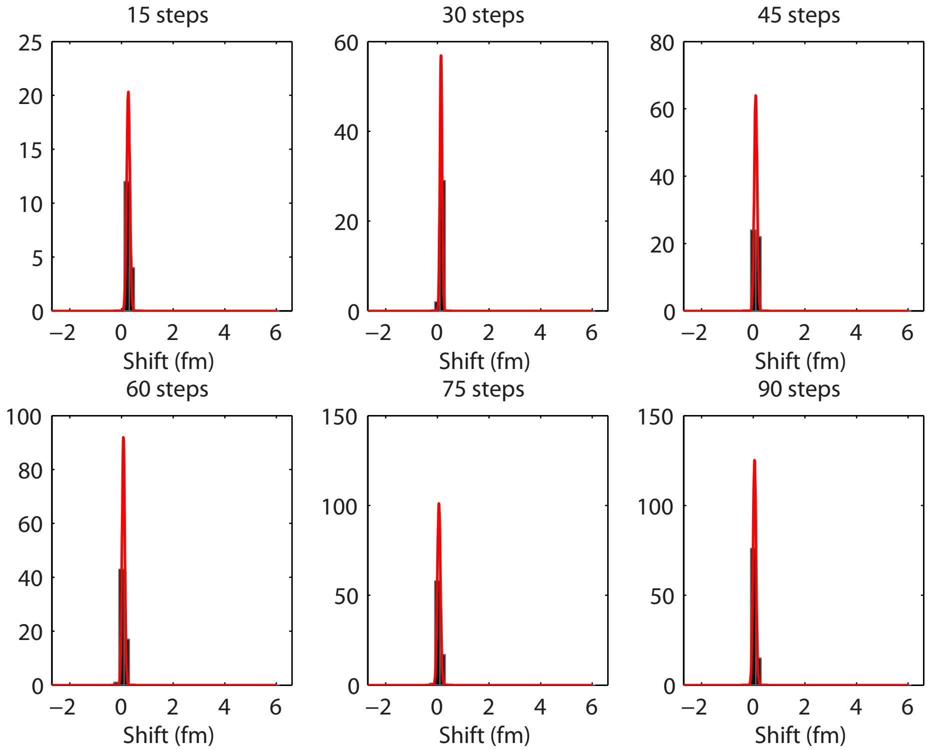

Figure 4.24: Histograms created from the step fit for pure buffer data. The fitting program returns steps, but they are of low statistical significance.

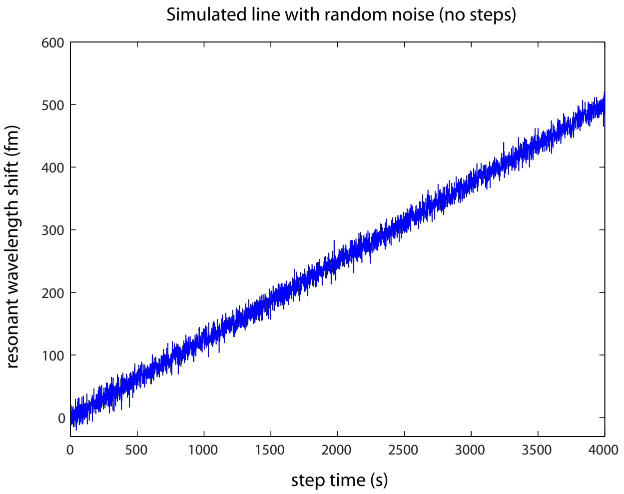

(a) Line with random noise (no steps).

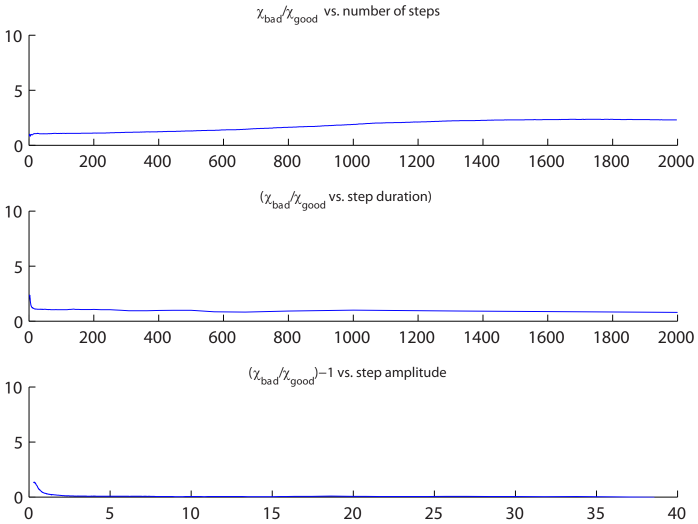

(b) Step fit quality plot for a sloped line with random noise.

Figure 4.25: (a) Simulated data of a sloped line with random Gaussian noise (no steps). This simulated data was processed using the same linear and median filtering procedures as actual data. (b) Step fit quality plot for a sloped line with random noise. The lack of a clear peak indicates that it is unlikely that statistically significant steps exist.

4.1.6 Effect of median filter

Understanding the effect of a median filter on the frequency domain is challenging, as a median filter is a nonlinear time-domain filter that does not have a frequency domain representation. We tested the effect of the median filter using simulation (Figure 4.26). For the simplest case we observed two steps separated by a small interval. These simulations took the raw steps, added a 2 kHz dither, low-pass filtered the signal at 1 kHz, and then median filtered the signal with a window of 1001 points. The amplitudes and time scales were all chosen to match the experimental parameters. As shown below, the results of these simulations are that the cutoff for preserving a step is that the two steps be separated by the low pass filter frequency cutoff (in this case 1 ms). The median filter does not limit the time resolution here. We note that in the case of a step-up followed by a rapid step-down, the median filter treats this event as a spike and removes it. Therefore, in some cases the median filter removes steps resulting in missed events.

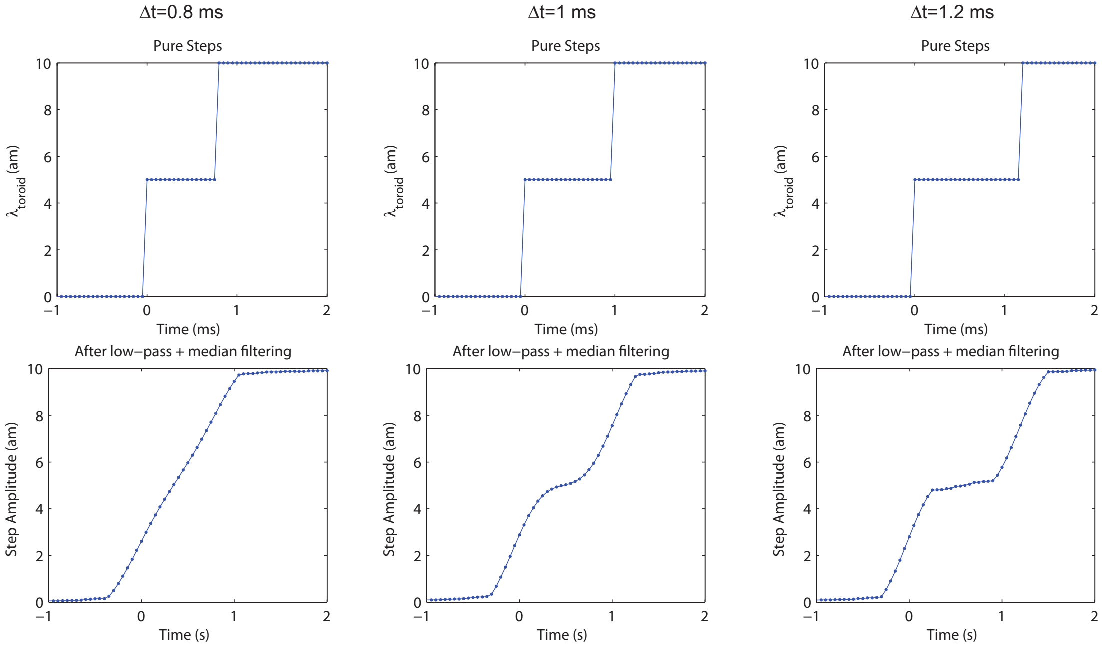

Figure 4.26: MATLAB simulation showing the effect of a median filter of size 1001 (50 ms) on the time resolution of the system. Steps were generated that were separated by a small interval Δt. As shown in the simulation, the time resolution is limited by the low pass and not the median filter. Steps separated by $\geq$ the low pass filter frequency of 1 kHz are clearly found.

4.1.7 Summary and conclusions regarding filtering and step finding methods

In summary, we tested several different means of data analysis. We discovered that multiplying the FFT in the frequency domain with a vector of 1's and 0's to mask the unwanted frequencies performed better than replacing the unwanted frequencies with values similar to its surrounding values. After removing unwanted frequencies (linear filtering) we further improved the signal to noise ratio of our system by examining two non-linear filters: a median filter and an algorithm known as total variation denoising. Both gave similar results, confirming the robustness of our data and its analysis. We tested both non-linear filters using a variety of window sizes and regularization parameters to determine the optimal input values. From there we used the χ^2 minimization algorithm of Kerssemakers [71] to fit steps to our data and generate a histogram of binding events. These histograms fit a Gaussian distribution with a clear peak as expected.

4.2 Single particle detection

4.2.1 Experimental protocol

We first start by seeing if our system can detect individual simple particles such as beads. We introduce bead solutions in deionized water at picomolar (pM) concentrations into our sample cell (Figure 4.27) under stopped flow conditions to minimize noise due to mechanical vibrations between the optical fiber and the microtoroid that occur during fluid injection [74]. First the sample is injected using a syringe pump (Harvard Apparatus), we then wait 30 seconds and then record our data. Our initial injection volume is enough to completely exchange the fluid in our open sample cell at least three times. As a control we also inject a solution of pure water (no beads). To minimize temperature effects, we thermally equilibrate all of our solutions and syringes in a room temperature water bath for at least one hour prior to injection. Immediately prior to injection into the sample cell, all solutions were briefly vortexed and sonicated for one minute.

4.2.2 Bead detection results

We first detect large $r = 100$ nm diameter polystyrene latex beads and gradually work our way down to $r = 2.5$ glass beads. $r = 2.5$ nm polystyrene latex beads are not available as polystyrene is a liquid at room temperature at this size. Figure 4.28B shows an example of detecting individual $r = 100$ nm diameter beads at pM concentration. For comparison, Figure 4.28A shows an example of what

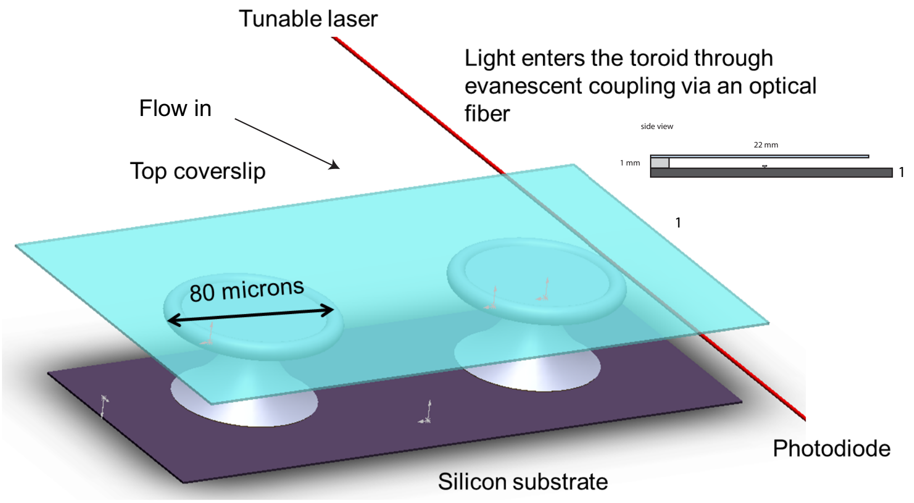

Figure 4.27: Sample cell schematic. Light is evanescently coupled into a microtoroid using an optical fiber (red). The toroid chip (silicon substrate) is mounted on a stainless steel sample holder (shown in the side view). A glass coverslip (light blue) is cantilevered out over the microtoroids by being glued on top of a microscope slide fragment (shown in side view) that has been cut to fit the dimensions of the stainless steel sample holder. Image rendered in SolidWorks.

the data looked like before implementing the feedback control system. As shown in Figure 4.29(a), the corresponding control of water (no beads), does not show similar step events. The step fit and corresponding histogram is shown in Figure 4.29(b). Figure 4.30 and Figure 4.31 show the time traces for all bead sizes. We note that our current results as shown in Figure 4.31 do not show a step size variation with laser power. It either does not exist or is within the error of our measurement. A summary of the bead detection data is shown in Figure 4.32. Based on our signal-to-noise ratio at $r = 2.5$ nm, this suggests that we can detect single small molecules (e.g., calculating based on its mass, the size of an interleukin-2 molecule is ~ 4 nm).

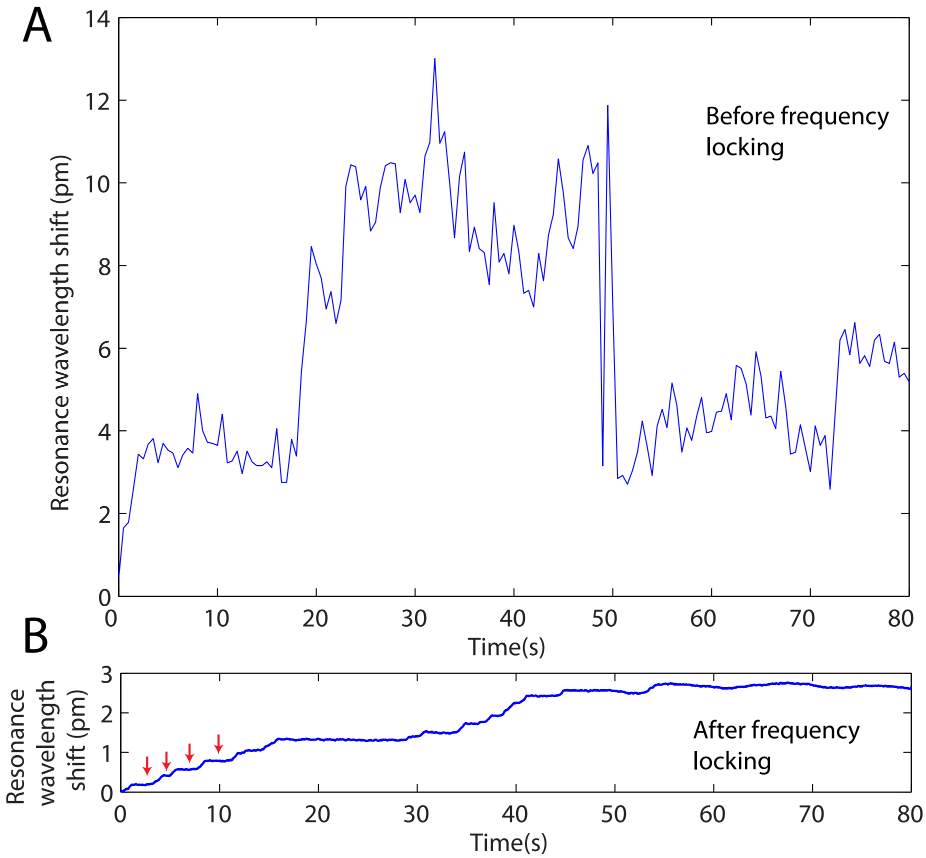

Figure 4.28: (A) Signal from $r = 110$ nm beads before the implementation of frequency locking. We note that our data before we implement frequency locking has lower signal-to-noise than as shown in [50] as this data was taken without the addition of a balanced detector which reduces noise due to laser power fluctuations (B) Detection of $r = 100$ nm beads after frequency locking. The noise is much less in (B).

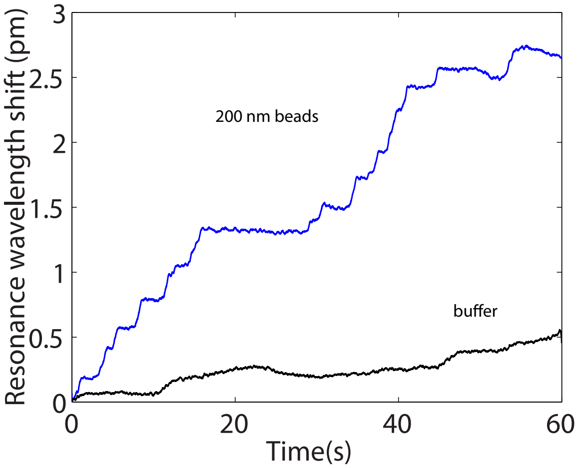

(a) $r = 100$ nm bead detection and buffer.

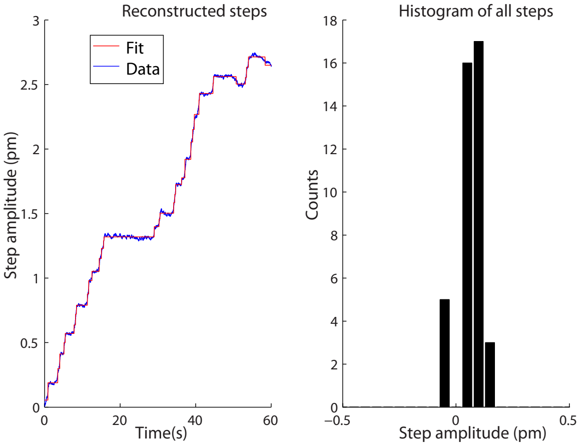

(b) 200 nm bead detection data.

Figure 4.29: (a) Detection of $r = 100$ nm beads in water (blue) binding to the surface of the microtoroid over one minute. As beads bind, the resonance wavelength of the microtoroid changes appearing as a step-event in the graph. The corresponding control (shown in black) of water (no beads) does not show similar step events. The results of fitting steps to buffer are shown in Figure 4.24. (b) $r = 100$ nm bead detection data (blue) and corresponding step-fit (red) and step-amplitude histogram.

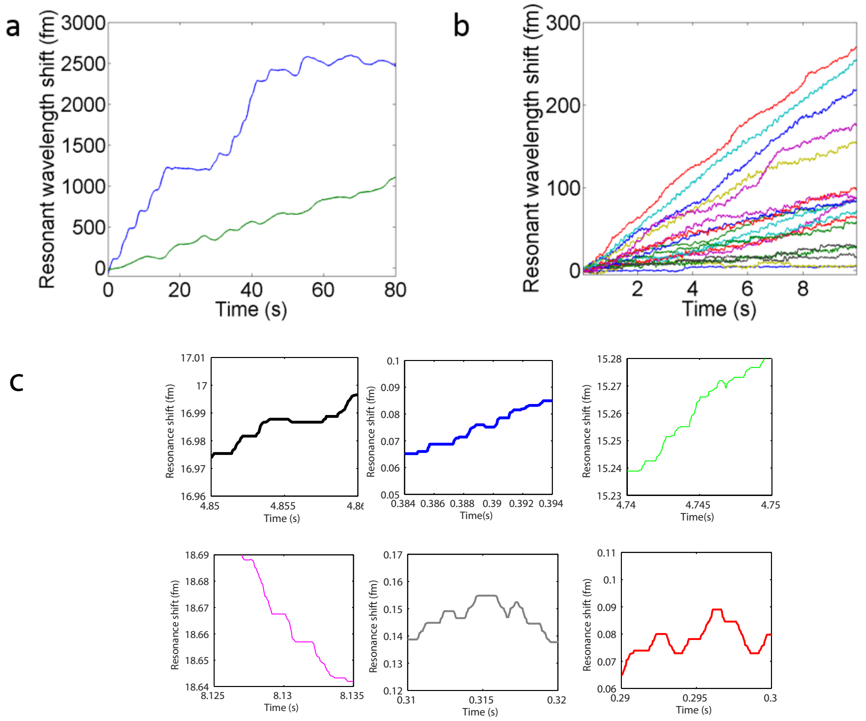

Figure 4.30: Nanoparticle detection data for $r = 2.5$, $r = 20$, and $r = 100$ nm diameter nanoparticles. Additional $r = 10$ nm nanoparticle data is shown in Figure 4.31 (a) Zoom-in of resonant wavelength shift over time of the microtoroid as $r = 100$ nm polystyrene latex nanoparticles bind to the microtoroid's surface. Each trace represents an experiment performed on a different toroid. (b) Zoom-in of resonant wavelength shift over time of the microtoroid as $r = 20$ nm polystyrene latex nanoparticles bind to the microtoroid's surface. (c) Zoom-in of resonant wavelength shift over time of the microtoroid as $r = 2.5$ nm glass nanoparticles bind to the microtoroid's surface.

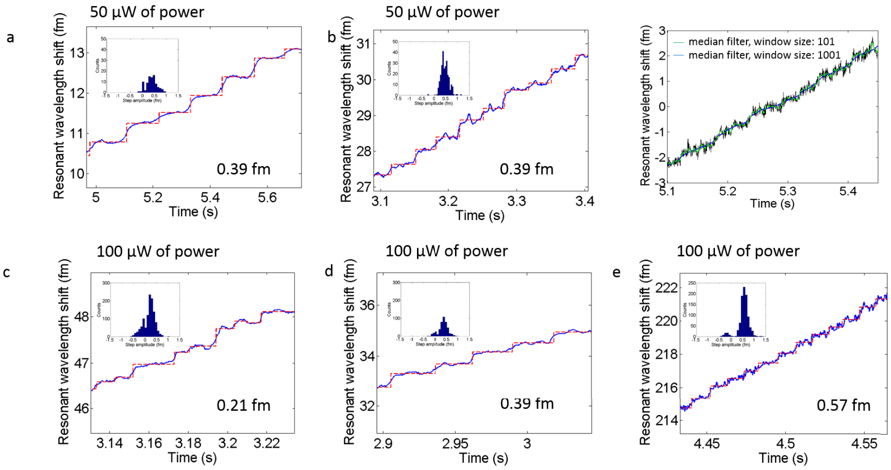

Figure 4.31: $r = 10$ nm nanoparticle detection by the microtoroid at different input coupling powers shows no detectable difference in step amplitude. (a)–(c) Zoom-in of $r = 10$ nm nanoparticle detection experiments performed at 100 μW of input power. The resonant wavelength shift over time of the microtoroid as the nanoparticles bind to the microtoroid's surface is shown in blue. The step-fit is shown as a red dashed line. The insets show histograms of the step amplitude. The mean step amplitude is reported in the lower right hand corner of each graph. (d)–(e) Zoom-in of $r = 10$ nm nanoparticle detection experiments performed at 50 μW of input power. The resonant wavelength shift over time of the microtoroid as the nanoparticles bind to the microtoroid's surface is shown in blue. The step-fit is shown as a red dashed line. The insets show histograms of the step amplitude. No observable difference in step amplitude was noticed between the two different powers. The mean step amplitude is reported in the lower right hand corner of each graph. For consistency, a median filter window size of 1001 was used in all experiments throughout the paper, however, for visualization purposes in (a), (b), (c), and (e), median window filter sizes of 101, 101, 101, and 11, respectively, were chosen. This does not significantly alter found step heights and locations but was done because for these specific cases due to differences in arrival times of the nanoparticles, a median widow size of 1001 tends creates an overly rounded step-appearance (f). (f) Data from (e), (shown in black) plotted with a median window filter size of 101 (green) and a median window filter size of 1001 (blue). Increasing the median window filter size to 1001 does not alter the step height and location, but creates an overly rounded appearance. These experiments were performed on the same microtoroid.

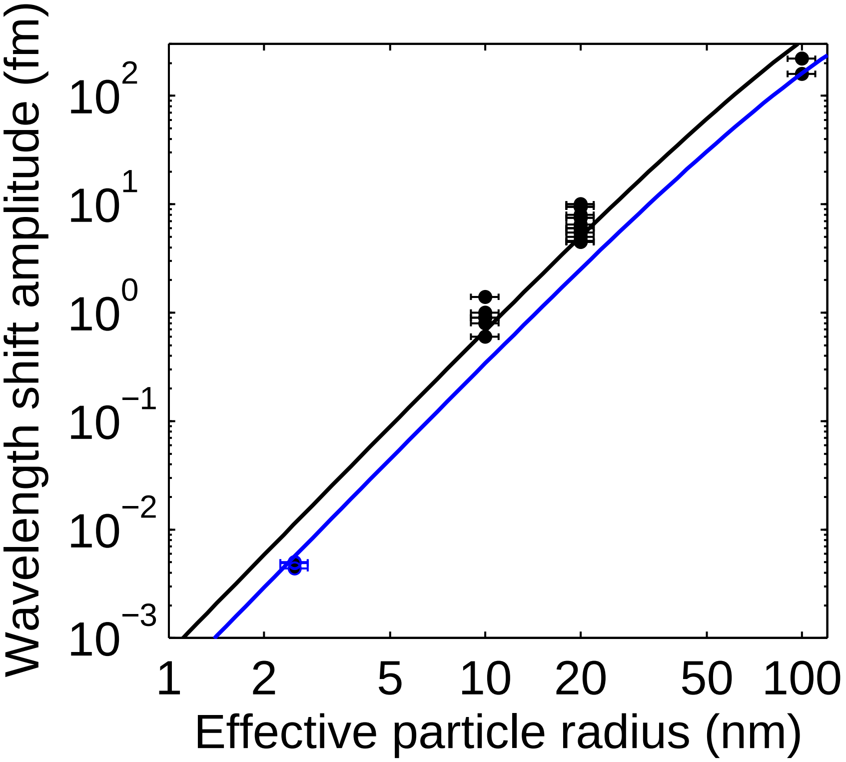

Figure 4.32: Summary of bead detection data. The data points represent maximum step amplitudes found from binding histograms for each particle size. Errors bars represent the known polydispersity of our samples. Solid lines represent reactive sensing principle theoretical predictions for different dielectric constants (D). The dielectric constant of polystyrene is 3.7 and the dielectric constant for silica is 1.85. The detection of $r = 2.5$ nm nanoparticles suggests that we are within the size regime of detecting single protein molecules (e.g., Human IL-2 is $r \sim 2$ nm).

Chapter 5

Biological detection

5.1 Surface functionalization

5.1.1 Linker synthesis

A major concern in biological detection is the need for selectivity as well as sensitivity [45, 75]. One challenge is the covalent linkage of biorecognition elements to the microtoroid's surface without lowering its quality factor [45, 56, 75, 76]. Many conventional attachment chemistries can scatter or absorb the light, thus lowering the toroid's performance. After several iterations, we eventually settled on a silane-PEG-maleimide linker (custom synthesized by Alex Goldberg and Brian Stoltz) to bind elements to the surface of the microtoroid (Figure 5.1). We examined both incubating our devices with a linker solution and vapor depositing the linker to the surface of the microtoroid as means of attaching the linker to the toroid without degrading the sensor performance.

5.1.2 Fluorescent images of linker binding

If proteins are being covalently bound to the toroid we should be able to see this trying to bind fluorescent proteins to the microtoroid and imaging the microtoroid with microscope capable of fluorescent detection. Therefore to demonstrate linker binding to the toroid's surface, we immersed the toroids in a fluorescent (Fluorescein isothiocyanate, FITC) antibody solution (FITC-human IgG Fc fragment, 40μM) for 2 hours with gentle nutation. Afterwards, the toroids were gently rinsed with deionized (DI) water and dried with a N_2 stream. A negative control of incubating 10 toroids (two

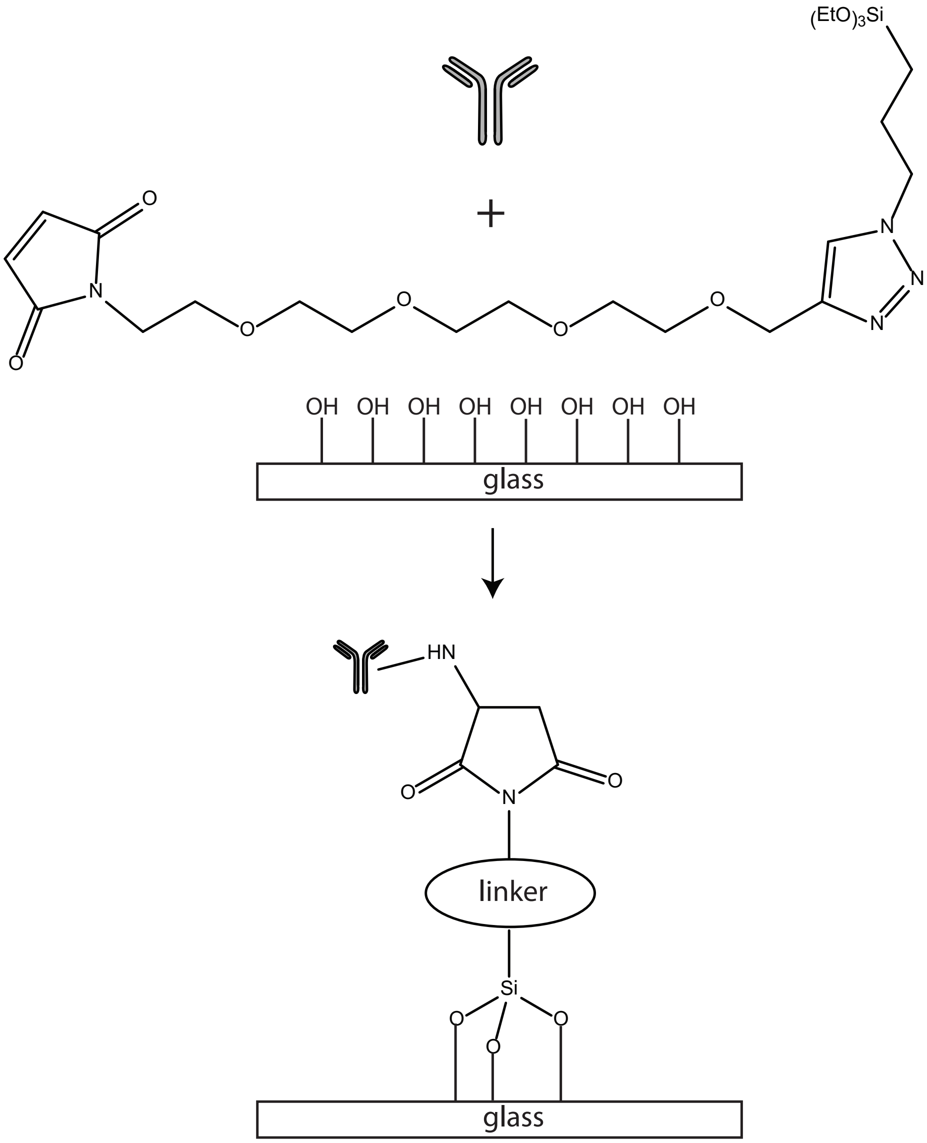

Figure 5.1: Linker schematic showing how an antibody plus the linker binds to the surface of the microtoroid. Figure was rendered using ChemBioDraw Ultra.

of which were imaged), with the antibody solution (no linker) showed low background fluorescence (Figure 5.3)B. Changing the nutation (rocking motion) direction every half hour causes uniform binding of the antibody fragment around the toroid’s rim (Figure 5.2).

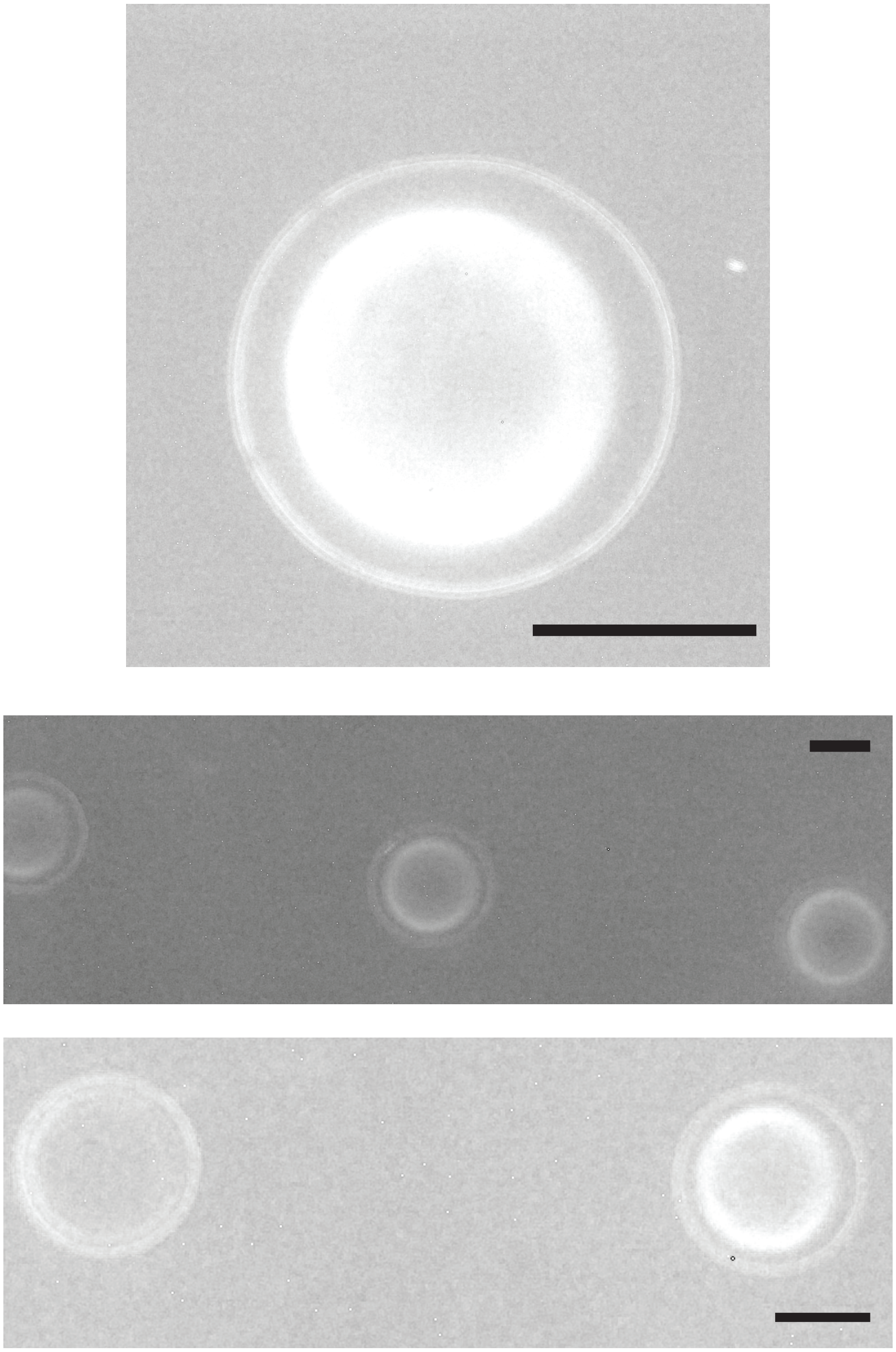

Figure 5.2: Demonstration that proteins are successfully bound to the surface of the microtoroid. These fluorescent microscope images show FITC-Fc bound to a linker bound to the surface of the microtoroid (top view). The images are of the same sample, just taken at different magnifications. The white glow is from the FITC and indicates that the protein is present on the toroid's surface. Scale bars are 45 μm.

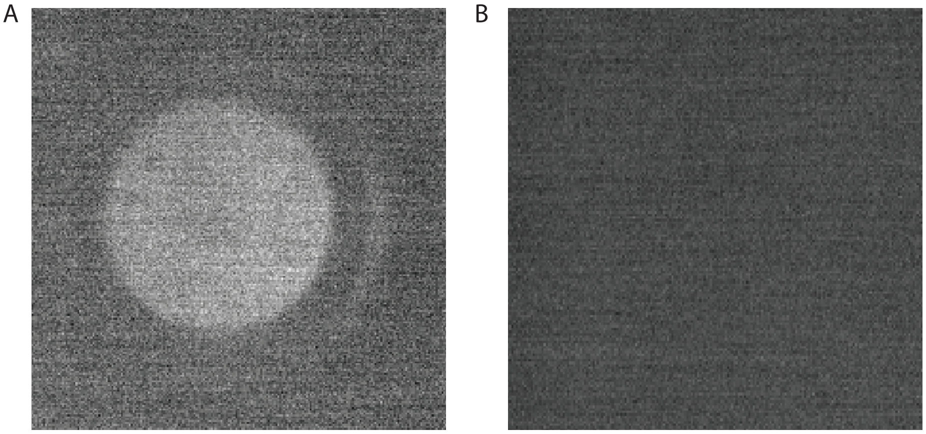

Figure 5.3: (A) FITC-Fc bound to linker bound to surface of the microtoroid (top view). (B) Negative control (fluorescent antibody incubation, no-linker). Images were taken at the same exposure level.

5.1.3 X-ray photoelectron spectroscopy (XPS) results

We further confirm the presence of the linker on our device using X-ray photoelectron spectroscopy (XPS). XPS is a technique that involves aiming a focused beam of x-rays at a sample under ultra-high vacuum conditions and measuring the energy of the photo-emitted electrons from the top few nanometers of the surface using an electron energy analyzer and electron collection lens [77]. Doing a surface scan for Oxygen (Figure 5.4), we can see a clear secondary peak in the solution deposited linker sample that is not present in the bare toroid case. This peak exists with a lesser amplitude in the vapor deposited linker sample shown in black, thus indicating that the linker was successfully vapor deposited as well. Vapor deposition enables a cleaner, more uniform coating of the microtoroid thus allowing us to maintain higher quality factors. We note that although vapor deposition of the linker allows for a more uniform coating of the microtoroid, the exosome detection data presented in this thesis was performed with linkers that were solution deposited. In the future vapor depositing the linkers would be a good way to improve the experiments. We have done the preliminary experiments to show that it works, however, we have not gotten a chance to apply it to detection experiments.

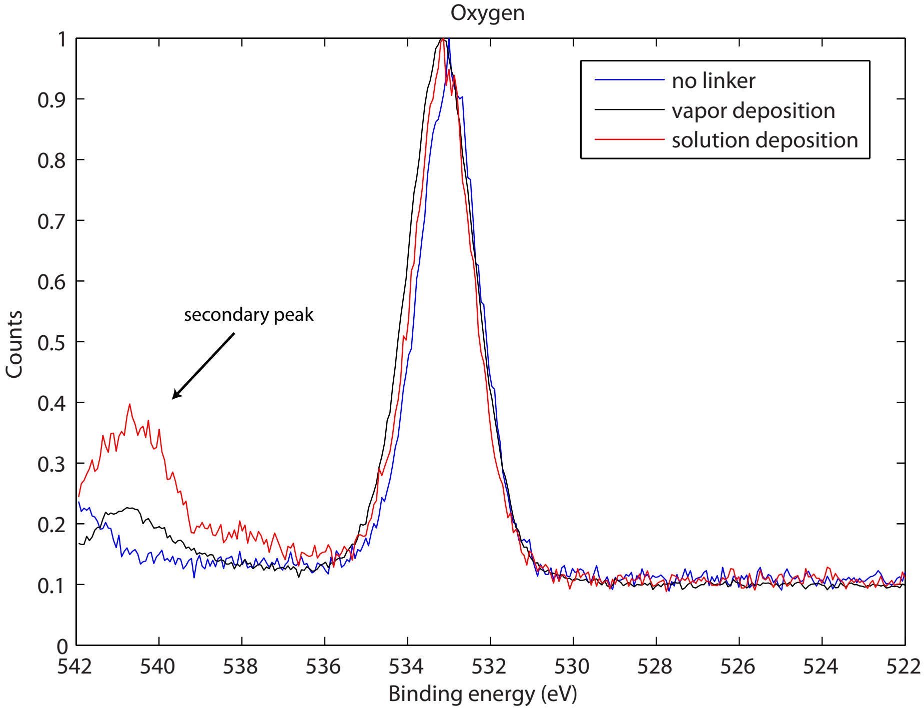

Figure 5.4: XPS data demonstrating that the linker binds in both the solution deposited case and the vapor deposited case. A clear peak from the linker at around 541 nm exists in the vapor (black) and solution (red) deposited sample. This same peak does not exist in the bare toroid sample (shown in blue), indicating that the peak is due to the presence of the linker. XPS data was taken at the Molecular Materials Research Center (MMRC, Beckman Institute, Caltech)

5.1.4 microRaman spectroscopy results

To further demonstrate that the linker binds uniformly around the rim of the microtoroid we performed surface microRaman spectroscopy at four 1-2 μm points along the top of microtoroid's rim (Figure 5.5(a)) on a sample that had part of the linker bound. A sample of just the linker was first run to get the Raman spectrum of the linker. The spectra are nearly identical at all four regions. We note that the first version of the linker that we used had two parts that were clicked together. The microRaman spectroscopy was performed on a toroid that had only the first half of the linker bound. This linker was a silyl azide. This experiment was performed to establish that the first part of the linker had bound successfully to the toroid.

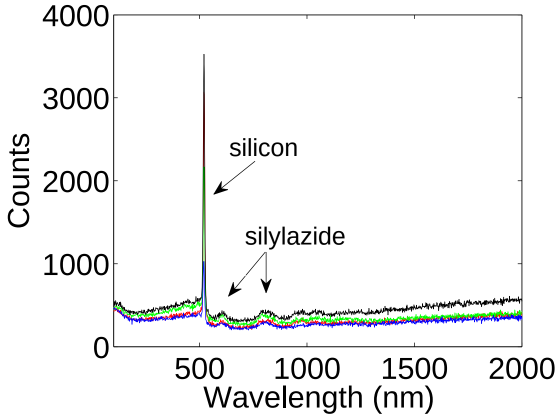

(a) Surface microRaman spectroscopy results.

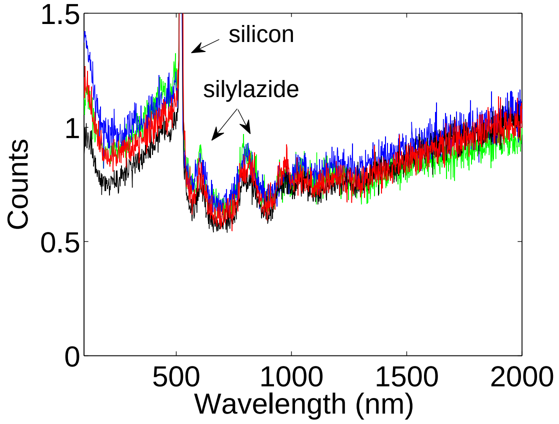

(b) Surface microRaman spectroscopy results normalized by the background value at 2 μms.

Figure 5.5: MicroRaman spectroscopy data showing uniform linker binding around the microtoroid's rim. (a) MicroRaman spectroscopy data. A 1 μm spot size was imaged at noon (red), 3 o'clock (green), 6 o'clock (blue), and 9 o'clock (black) on the toroid's surface (looking from the top). The colors represent the location on the toroid's surface that was imaged. A clear peak is shown at $\sim$ 520 nm for silicon and two smaller peaks are shown for the silylazide linker indicating the presence of the linker. (b) MicroRaman spectroscopy data normalized by the background value at 2 μms far away from any particular peak. The curves are similar at each location indicating that the linker has bound uniformly. Data was taken with the help of Prof. George Rossman (Geological and Planetary Sciences, Caltech).

5.2 Ribosome detection

To test our system with biological molecules we introduced a purified ribosome containing solution under stopped flow conditions to the microtoroid. Ribosomes were picked as they are relatively large (r $\sim$ 10–12.5 nm) and so should give clean, discrete steps (Figure 5.6). These particular ribosomes were synthesized by Saccharomyces cerevisiae (species of yeast) and were provided by the Deshaies lab at Caltech. Ribosomes are composed of RNA and proteins [78]. They are important as they link amino acids together to form proteins. As such they play a key role in the central dogma of molecular biology (from DNA to RNA to protein). Discrete step events corresponding to the binding of individual ribosomes to the microtoroid's surface may be seen in Figure 5.7. The maximum step amplitudes seen in Figure 5.7 correspond to what we expect to see for similarly sized beads.

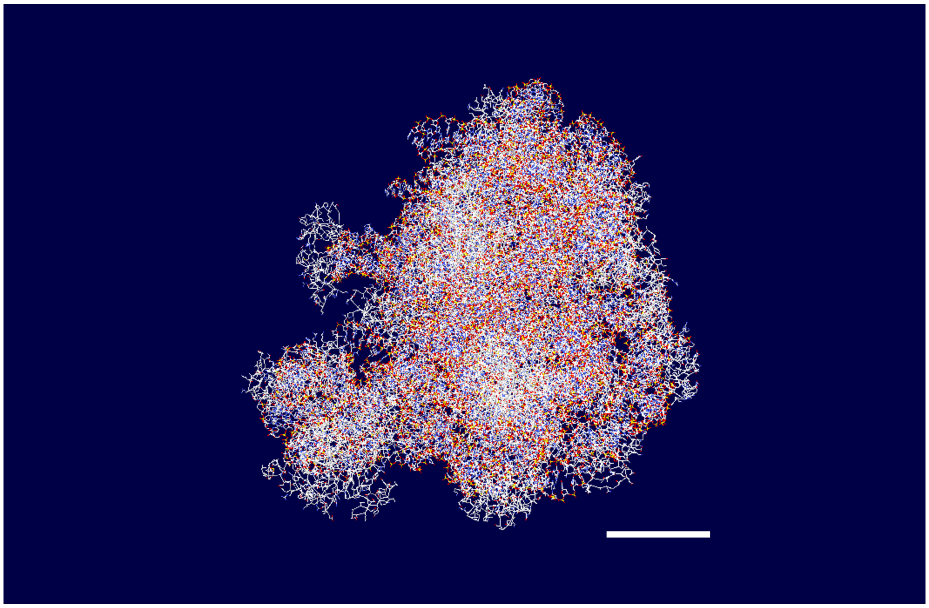

Figure 5.6: Model of ribosome complex from Saccharomyces cerevisiae. Image was created using CPK (Corey-Pauling-Koltun) coloring in Swiss-PDBviewer from a composite of protein data base (PDB) entries 1S1H (40S ribosomal subunit) and 1S1I (60S ribosomal subunit). Scale bar is 5 nm.

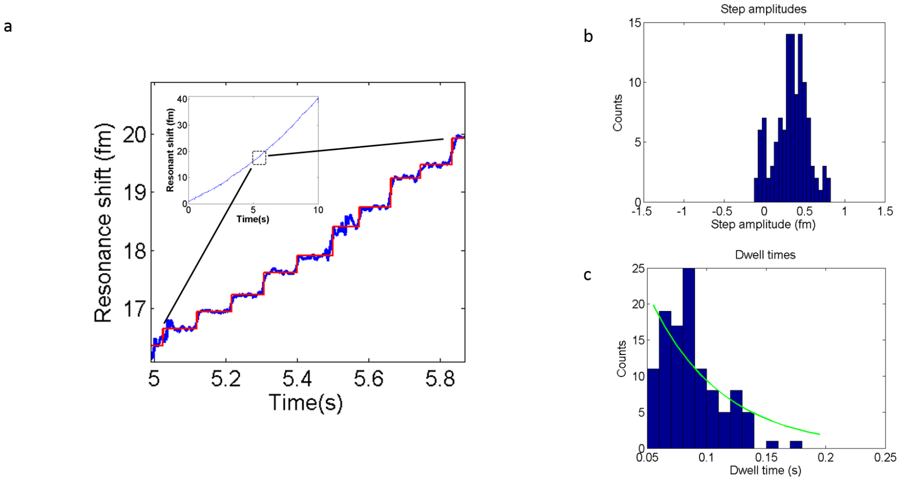

Figure 5.7: Individual yeast ribosome detection. (a) The resonant wavelength shift (blue trace) over time of the microtoroid as ribosomes bind to the microtoroid's surface. The step-fit is shown in red. (inset) Zoom-out of the toroid response over the full recording range of 10 seconds. (b) Histogram of step amplitudes. The maximum step amplitude of ~ 0.8 fm corresponds to a size of $r = 12.6$ nm as predicted by our nanoparticle detection data thus suggesting that the binding of individual ribosomes is being observed. Negative step amplitudes correspond to unbinding events. (c) Histogram of the time in between steps (dwell times). As expected for single-particle binding, the dwell time distribution follows an exponential fit (green). Ribosomes were provided courtesy of Ray Deshaies.

5.3 Exosomes as a non-invasive tumor biopsy assay

We can also use the microtoroid to detect individual exosomes (Figure 5.8). Recent work from a number of labs has demonstrated that tumor cells in culture and in vivo create exosomes, small vesicular bodies that can be collected from the tissue culture medium and the serum of the patient. While there are still debates about the potential role(s) of exosomes in cancer, such as inducing immune tolerance, their presence offers an exciting opportunity to obtain a profile of tumor surface antigens and even a sampling of tumor RNA markers by analyzing serum samples. This would be particularly attractive in the active management of cancer therapy as it exploits the circulation of the blood to sample tumor surfaces without the need to find or access the tumors. It also offers an opportunity to guide the most informative molecular imaging ligands for use in PET by permitting the surface labels expressed by different subclones of the tumor to be detected.

Due to their small (r *sim* 15–45 nm) size, exosomes are below the detection limit of bright field microscopy. As such, several optical methods have been used instead to detect and characterize exosomes. These include dynamic light scattering (DLS) combined with nanoparticle tracking analysis, and fluorescence techniques such as flow cytometry, fluorescence correlation spectroscopy, and stimulated emission depletion (STED) microscopy [79]. Non-fluorescent sensing techniques such as DLS are often preferred as labels (depending on their nature and quantity required), can be expensive, difficult to generate, and for small analytes, might perturb the molecular events under study. Dynamic light scattering, however, lacks both the molecular specificity and the sensitivity needed to detect ultra-low concentrations of analyte which would prove useful for early diagnosis, eliminate the need for large sample volumes, and speed analysis.

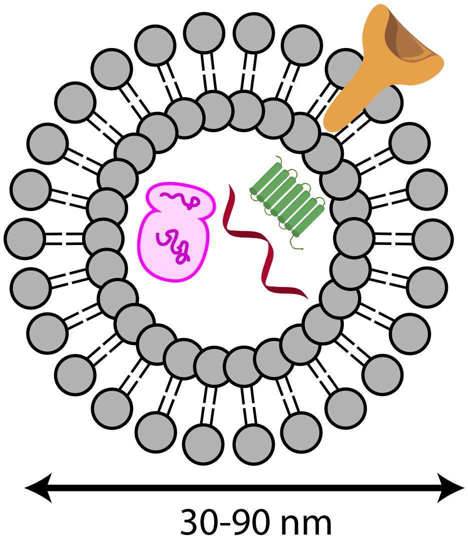

Figure 5.8: Cartoon of an exosome. Within the exosome are mRNA, miRNA, and cellular proteins [78]. Figure drawn using ChemBioDraw Ultra.

5.3.1 Data from exosomes grown in culture

We first begin by examining exosomes from human mesenchymal stem cells that were grown in culture and purified (in collaboration with Andrew Raubitschek, City of Hope). Anti-CD81, a marker that binds exosomes, was first covalently bound to the surface of the toroid, the sample cell was flushed two times with 0.9% saline and the exosome containing solution was introduced under stopped flow conditions following the procedures previously outlined in Section 4.2.1. Figure 5.9

shows the binding of individual exosomes to the microtoroid's surface. The slightly sloped rise between the plateaus of each step is a factor of the controller response and may be adjusted to have a more vertical appearance.

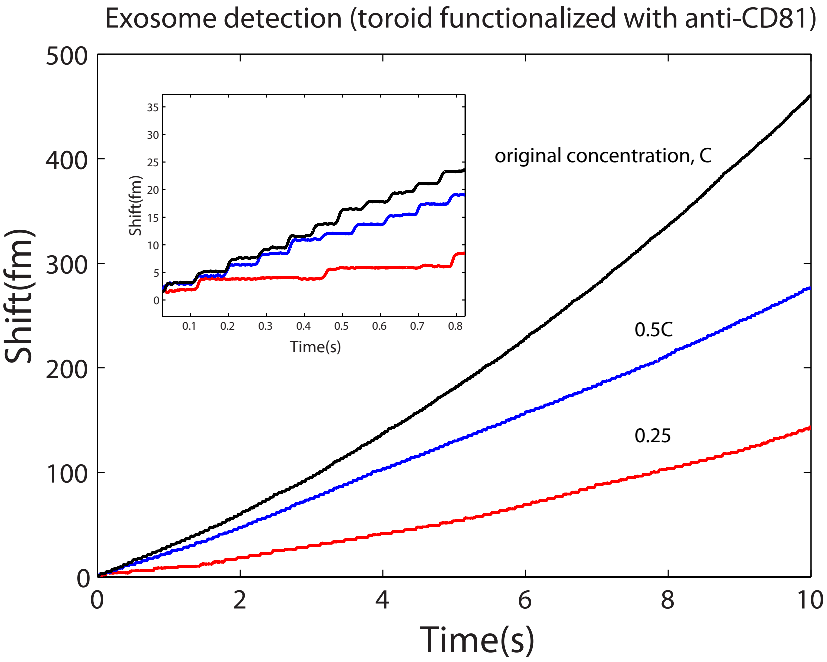

Figure 5.9: Toroid response from three different concentrations of an exosome-containing solution. Exosomes from human mesenchymal stem cells that were grown in culture were purified and diluted in saline and flowed over the surface of the toroid at different concentrations. Discrete binding events were observed corresponding to the binding of individual exosomes. The number of binding events scaled inversely with the dilution of the exosome solution, further suggesting that the binding events observed were indeed from individual exosomes. Exosomes provided courtesy of Andrew Raubitschek, City of Hope.

5.3.2 Data from human tumors implanted in mice

To test the toroid's ability as a molecular exosome sensor for medical diagnosis, athymic (nude) mice were implanted with Daudi (Human Burkitts Lymphoma) tumor cells for 5 weeks at which point the mice were euthanized as the tumors had grown too large. Each week blood was drawn from the tail vein of the mouse and frozen. One microliter of blood from each week was diluted a million-fold in saline and sequentially flowed over the toroid. Prior to injection, the surface of the toroid was functionalized with a custom linker and sensitized with anti-CD81, an exosome specific antibody. As seen in Figure 5.10, each week shows an increase an exosome level as detected by the microtoroid. At week 0, very little response is seen as expected. Zooming into the data trace for week 5 (Figure 5.11, inset), one can see discrete step like events corresponding to the binding of

Table 5.1: Mouse tumor data: Fit parameter a (steady state value, fm)

	Week 0	Week 1	Week 2	Week 3	Week 4	Week 5
Mouse 1	nil	4.72	8.33	8.37	12.03	17.19
Mouse 2	nil	7.00	7.44	7.72	20.75	33.59
Mouse 3	nil	6.49	4.49	21.49	22.54	46.83
Mouse 4	nil	4.56	11.18	N/A	N/A	N/A
Mouse 5	nil	5.10	7.25	7.27	25.22	50.14
SEM[1]	nil	0.49	1.07	3.43	2.85	7.49

[1] Standard error of the mean

individual exosomes. The amplitude of these events corresponds to the shift one would expect to see from particles 40. nm in diameter. We fit the data trace for each week an exponential function to determine the initial slope and steady state value of the toroid response curves. These fit parameters are useful to quantify how exosome levels change in a mouse the longer a tumor has been there. A summary of the fit parameters for all five mice are given in Tables 5.1, 5.2, and 5.3. The values presented in Tables 5.1, 5.2, and 5.3 are also plotted in Figures 5.12(a), 5.12(b), and 5.12(c).

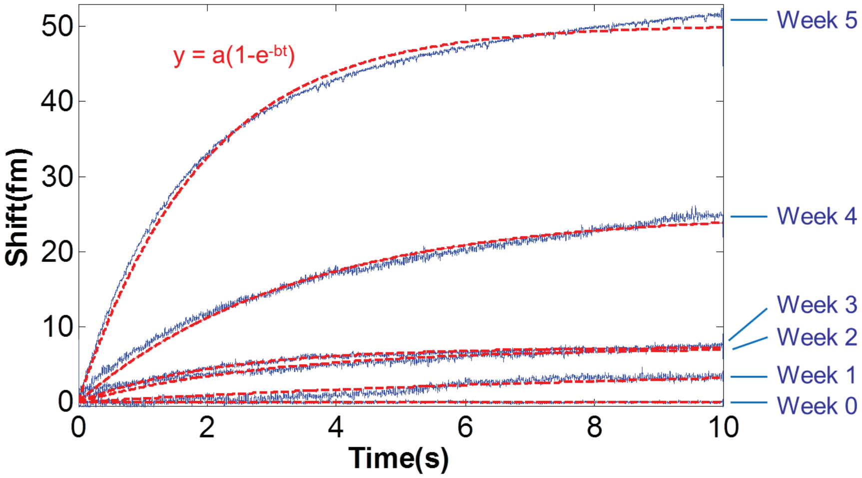

Figure 5.10: Exosome detection for a non-invasive tumor biopsy assay. A tumor was implanted in the mouse and each week blood taken from the mouse and diluted 1:10^6 in buffer. For each week we see an increase in the response from the sensor corresponding to increasing exosome levels. No signal was obtained from week 0. The data traces are fit with a simple exponential (dashed red line).

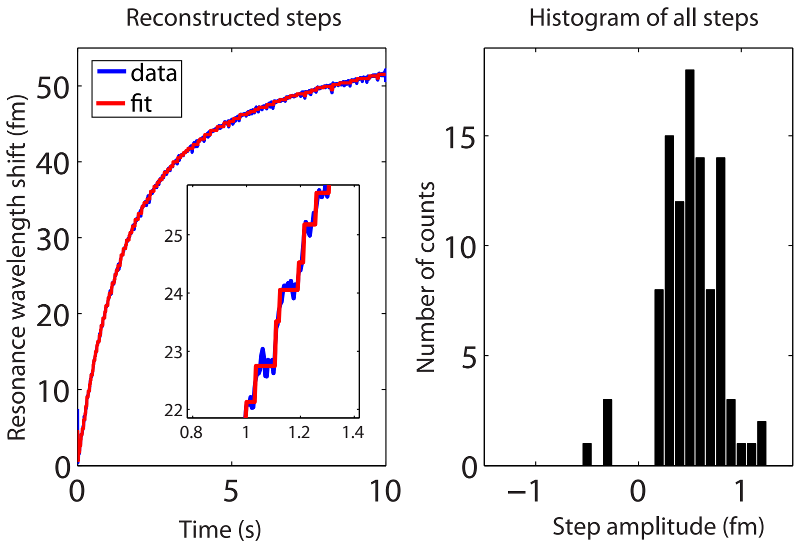

Figure 5.11: Toroid response data to a solution containing blood from a mouse with a tumor implanted in it for five weeks. A Zoom in of week 5 and corresponding step-fit and histogram of step heights is provided as well. Individual steps corresponding to the binding of individual exosomes may be seen. Negative step amplitudes represent step down or unbinding events.

Table 5.2: Mouse tumor data: Fit parameter $1/b$ (rise time (s))

	Week 0	Week 1	Week 2	Week 3	Week 4	Week 5
Mouse 1	nil	4.24	4.23	3.31	2.93	1.57
Mouse 2	nil	4.45	3.29	3.00	2.55	2.23
Mouse 3	nil	6.63	2.69	4.22	2.98	1.85
Mouse 4	nil	10.00	9.56	N/A	N/A	N/A
Mouse 5	nil	nil	3.03	2.14	3.40	1.90
SEM[1]	nil	1.34	1.28	0.43	0.17	0.13

[1] Standard error of the mean

5.3.3 Comparison to Nanosight

For comparison, the same samples were run on a Nanosight, a commercially available instrument that detects particles based on standard light scattering and nanoparticle tracking. Although particles

Table 5.3: Mouse tumor data: Initial slope (ab)

	Week 0	Week 1	Week 2	Week 3	Week 4	Week 5
Mouse 1	nil	1.11	1.97	2.53	4.10	10.92
Mouse 2	nil	1.57	2.26	2.57	8.14	15.07
Mouse 3	nil	0.98	1.67	5.09	7.56	25.26
Mouse 4	nil	0.46	1.17	N/A	N/A	N/A
Mouse 5	nil	nil	2.39	3.40	7.42	26.39
SEM[1]	nil	0.23	0.21	0.73	1.09	3.69

[1] Standard error of the mean

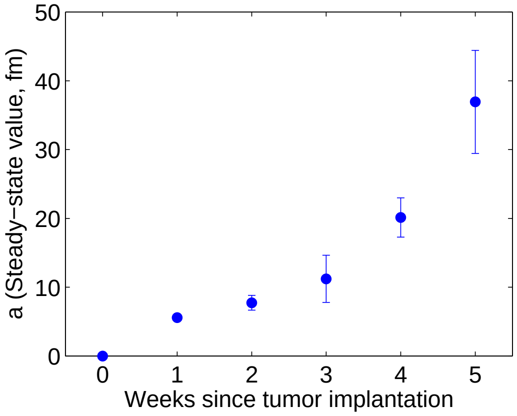

(a) Steady state values

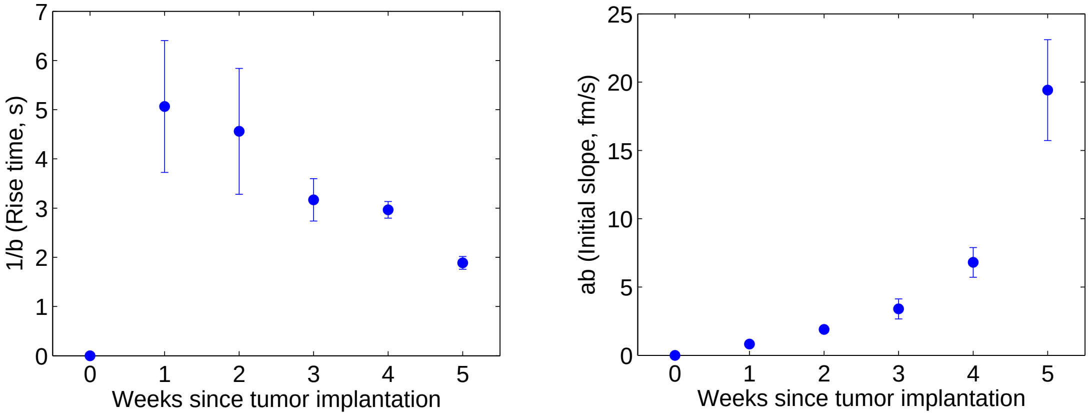

(b) Rise times

(c) Initial slope values

Figure 5.12: Compiled exosome detection results from all mice reflect tumor progression. (A) Fitted steady-state values increase monotonically, reflecting higher exosome concentrations at late stages. (B) Rise times decrease monotonically, although the trend is not as pronounced as in (A). The value for week zero is recorded as zero, as the trace was effectively flat. (C) Initial slope increases monotonically as more exosomes bind to the toroid per unit time.

are detected with the Nanosight, because it lacks molecular specificity, the clean data traces showing an increase in exosome concentration over time are not seen (Figure 5.13(a)). Table 5.4 shows a compilation of the total number of particles/mL for each mouse over each week calculated by the Nanosight. Serum samples were diluted 1:1000 (vs. $1:10^6$ for the microtoroid) in saline before running on the Nanosight. The Nanosight cannot detect particles at a $1:10^6$ dilution. As seen in Table 5.4, the standard error of the total particle concentration at each week across each mouse is significantly more than the standard error of parameters such as the initial slope calculated from the data taken on the microtoroid. We note that both number and size of the particles that are able to be detected are important. Size information is useful as it gives us additional information to determine what particles have bound. The number of particles (i.e., concentration data) is relevant as the ability to detect low concentrations of molecules is important in scenarios where reagents are limited and/or costly or unpleasant for the patient to provide in large quantities (e.g., human blood). Being able to detect low concentrations of molecules also has implications for early detection of disease.

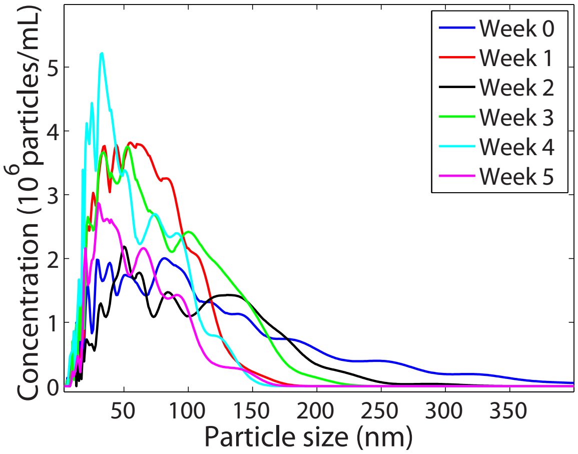

(a) Number of particles found/mL using the Nanosight.

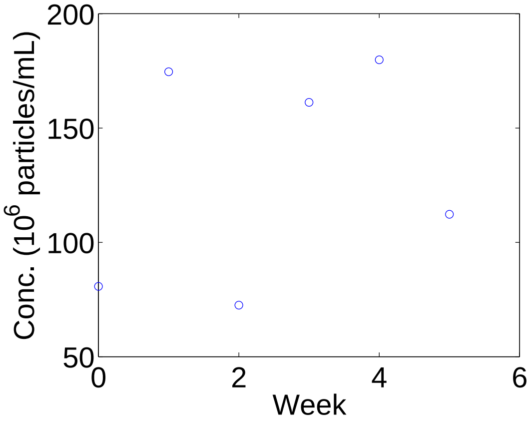

(b) Number of 20–70 nm particles found/mL using the Nanosight.

Figure 5.13: Nanosight data for Figure 5.10. (a) Concentration of particles found vs. size of particles found. Each week the tumor was implanted is represented in a different color. There are particles in the sample, but as there is no molecular sensitivity, the Nanosight cannot give the clean data of the microtoroid (i.e., there is no clear trend between concentration of particles found and week the tumor has been implanted). (b) Plotting the number of particles found in the exosome size regime (20–70 nm), shows no correlation with the week the tumor was sampled. Data was taken on a Nanosight 500 (usage courtesy of Mark Davis' lab).

Table 5.4: Nanosight data: Total number of particles/mL

	Week 0	Week 1	Week 2	Week 3	Week 4	Week 5
Mouse 1	$4.50 \text{x} 10^7$	$2.54 \text{x} 10^8$	$7.80 \text{x} 10^7$	$1.49 \text{x} 10^8$	$1.00 \text{x} 10^8$	$2.40 \text{x} 10^8$
Mouse 2	$2.83 \text{x} 10^8$	$4.20 \text{x} 10^8$	$2.38 \text{x} 10^8$	$3.43 \text{x} 10^8$	$1.37 \text{x} 10^8$	$1.05 \text{x} 10^8$
Mouse 3	$2.32 \text{x} 10^8$	$3.00 \text{x} 10^6$	$2.40 \text{x} 10^8$	$3.79 \text{x} 10^8$	$2.44 \text{x} 10^8$	$3.34 \text{x} 10^8$
Mouse 4	$1.52 \text{x} 10^8$	$6.60 \text{x} 10^7$	$2.82 \text{x} 10^8$	$1.14 \text{x} 10^8$	$1.66 \text{x} 10^8$	$1.54 \text{x} 10^8$
Mouse 5	$2.91 \text{x} 10^8$	$3.23 \text{x} 10^8$	$2.29 \text{x} 10^8$	$3.59 \text{x} 10^8$	$3.03 \text{x} 10^8$	$1.84 \text{x} 10^8$
SEM[1]	$4.61 \text{x} 10^7$	$7.82 \text{x} 10^7$	$3.51 \text{x} 10^7$	$5.66 \text{x} 10^7$	$3.69 \text{x} 10^7$	$3.93 \text{x} 10^7$

[1] Standard error of the mean

Chapter 6

Single molecule detection

6.1 Detection of human IL-2 and mouse IgG

Highly sensitive biodetection is important for many applications such as high throughput drug discovery studies, as it can dramatically reduce the amount of analyte needed and speed the assays [15, 55]. A variety of applications in medical diagnostics (e.g., detecting trace amounts of tumor specific antigens to monitor the re-occurrence of cancer [80]) and public health (e.g., detecting bacteria or viruses [21]) would benefit from improved speed and sensitivity. If the sensitivity can be pushed to the single-molecule level, fundamental studies become more direct and decisive, permitting, for example, studies of molecular conformations [15, 55].

We attempt to see whether we can detect single molecules at attomolar concentrations by looking at the binding of human interleukin-2 (Figure 6.1) (Pierce Biotechnology) and mouse immunoglobulin G (Jackson Immunoresearch) to the surface of the toroid. IL-2 has a molecular weight of 15.5 kDa and mouse immunoglobulin G has a molecular weight of approximately 150–160 kDa. For size comparison their structures are shown in Figure 6.2.

Figure 6.3 shows IL-2 binding at three different concentrations. The same parameters for median window size were used as was deemed best in Section 4.1. We summarize data for initial slopes for three repeats of three different concentrations in Table 6.1. As expected, initial slope increases with concentration. We note that over the full time course of the experiment (10 seconds), we see an overall shift in the resonance frequency, indicating more binding than unbinding events. We found

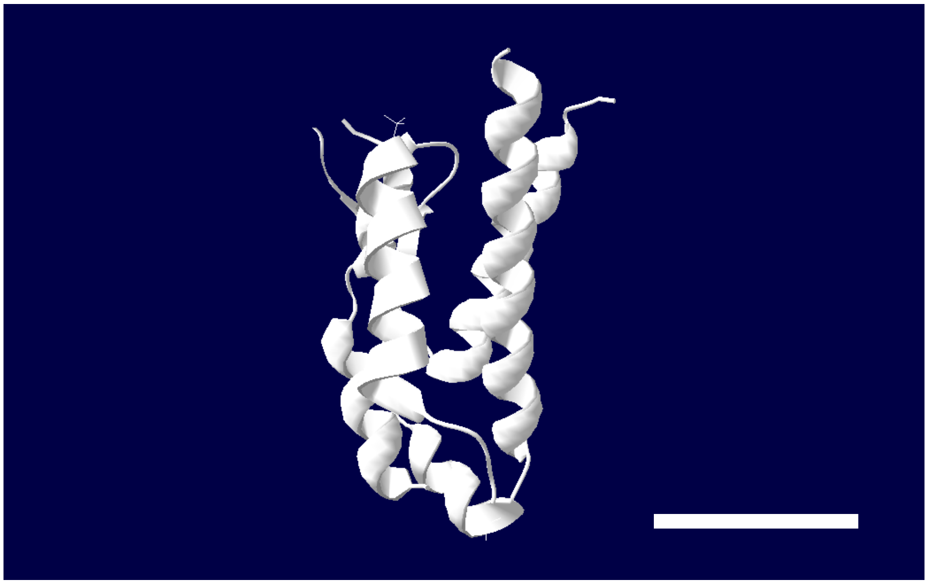

Figure 6.1: Structure of human IL-2. Image was created using in Swiss-PDBviewer from protein data base (PDB) 1M47. Scale bar is 4 nm.

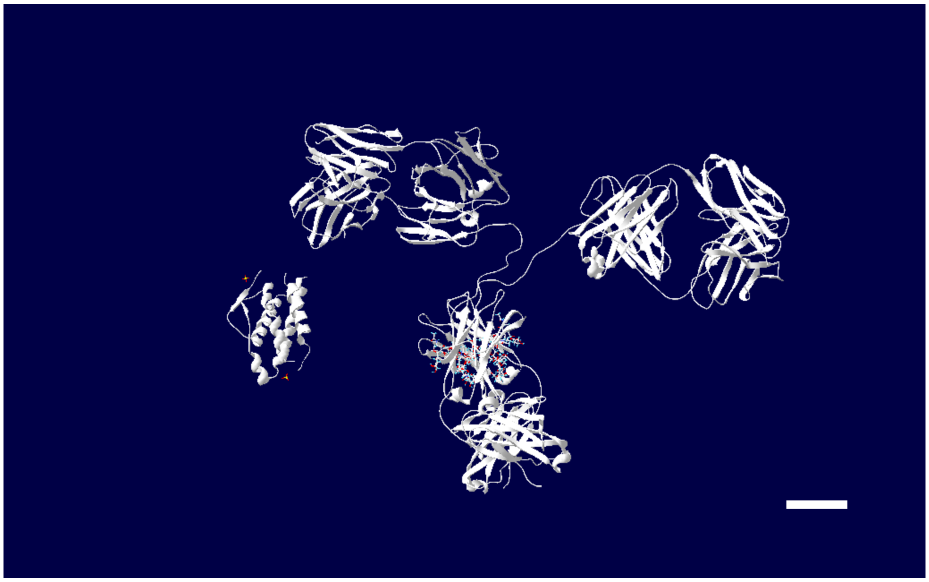

Figure 6.2: Structure of mouse immunoglobulin (right structure) in relation to human IL-2 (left structure). Image was created using in Swiss-PDBviewer from protein data base (PDB) entries MA231 and 1M47. Scale bar is 4 nm.

the quality factors for the microtoroid to be very similar across different concentrations ($\sim 10^5$ in water) and did not notice a dependence of slope on quality factor. In our experiments we use moderate ($\sim 10^5$ in water) Q-values (Table 6.2). These lower Q-factors are chiefly a result of the optical fiber being positioned in direct contact with the microtoroid in the over-coupled regime. In this regime, the optical fiber is too close to the microtoroid and so the amount of light entering the toroid decreases due to scattering off of the optical fiber. This procedure was chosen to minimize noise due to the optical fiber fluctuating against the toroid during the experiment. In addition, it is often difficult to adjust the coupling of the optical fiber with the toroid to achieve optimal Q because when experiments are performed in water, moving the optical fiber through liquid increases the likelihood that it will break. The highest Q-values would have been obtained when the tapered fiber is positioned within a wavelength of the toroid, but not directly touching. We note that the loaded Q-values in air, were higher $\sim 10^6$–10^7. Although it was possible to manufacture toroids of higher quality factors, the experiments worked with lower quality toroids, and so every toroid could be utilized with little regard for quality factor. The coupled power into the microtoroid was determined to be $\sim$ 10–100 μW.

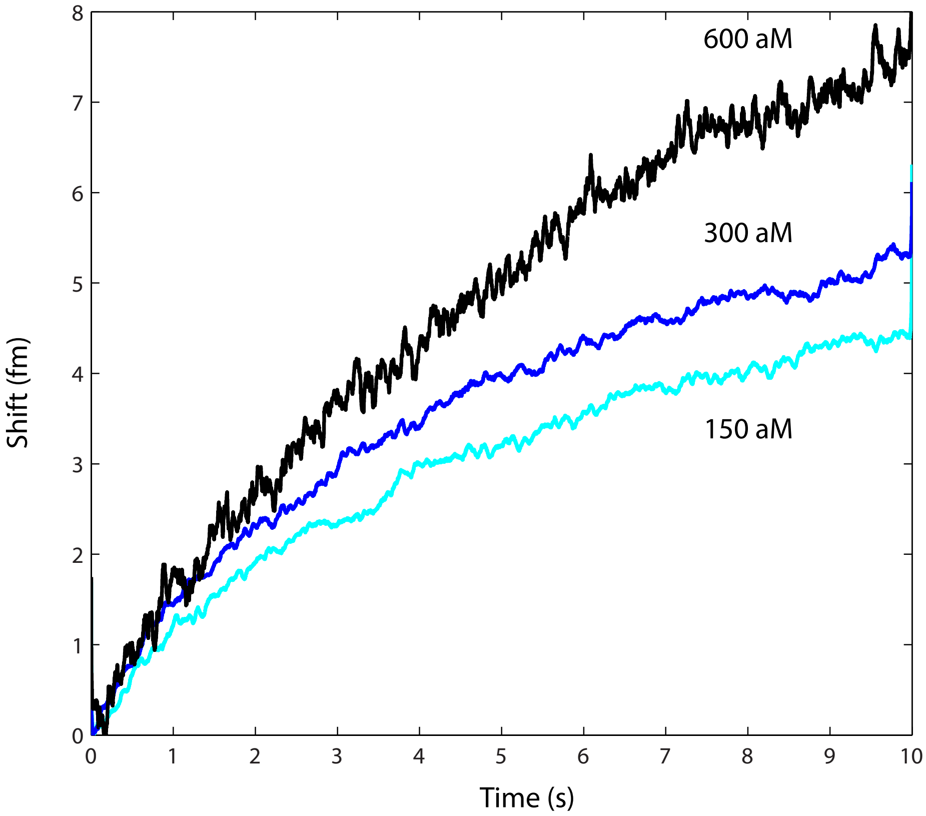

Figure 6.3: Microtoroid detection data of IL-2 at three different concentrations. We note that our binding data is not corrected for a temperature red-shift as it would be difficult to know what percent of the shift was due to binding and what percent of the shift was due to heating. As expected, the initial slope of each curve scales with concentration.

Table 6.1: IL-2 binding data: Initial slope (fm/s)

	Trial 1	Trial 2	Trial 3
150 aM	1.58	1.11	1.49
300 aM	3.66	1.42	2.01
600 aM	3.73	1.52	2.58

Table 6.2: IL-2 binding data: Q-value

	Trial 1	Trial 2	Trial 3
150 aM	6×10^5	1×10^5	1×10^5
300 aM	–	1×10^5	2×10^5
600 aM	2×10^5	2×10^5	1×10^5

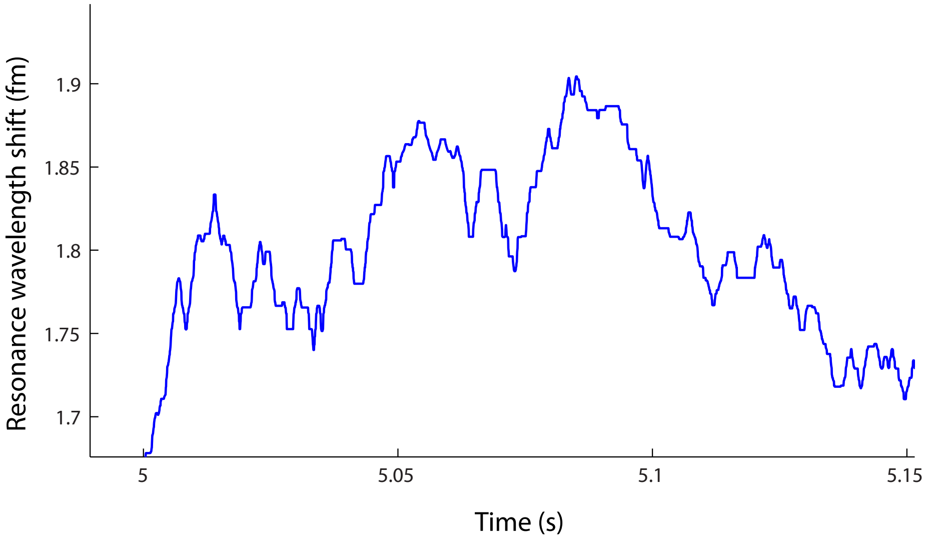

Figure 6.4: Resonance wavelength shift over time as mouse IgG molecules bind to the surface of the microtoroid.

We also examined under stopped flow conditions the detection of 600 aM of mouse IgG (150–160 kDa) which was diluted in PBS without Calcium and Magnesium. The corresponding time trace is shown in Figure 6.4. The Q for the mouse IgG data was fairly similarly across runs and was calculated to be ∼ 1.2x10^5 (Table 6.3). Maximum step amplitude data for mouse IgG is summarized in Figure 6.5.

Table 6.3: Mouse IgG binding data: Q-value

Run	Q-value
1	1×10^5
2	1×10^5
3	1×10^5
4	–

For the specific detection of human interleukin-2, antibodies (Anti-Human Interleukin-2, Pierce Biotechnology) were attached to the toroid's surface using a silane linker. Our results (Figure 6.6 and 6.7), over a range of sizes, show discrete, step-like, binding events with a step amplitude that corresponds well with the 'reactive' model prediction, suggesting that we are detecting single particles and not clusters. As with the nanoparticle detection data, the time delay between bioparticle binding events follows an exponential distribution. As for the mouse IgG data, the maximum step amplitudes

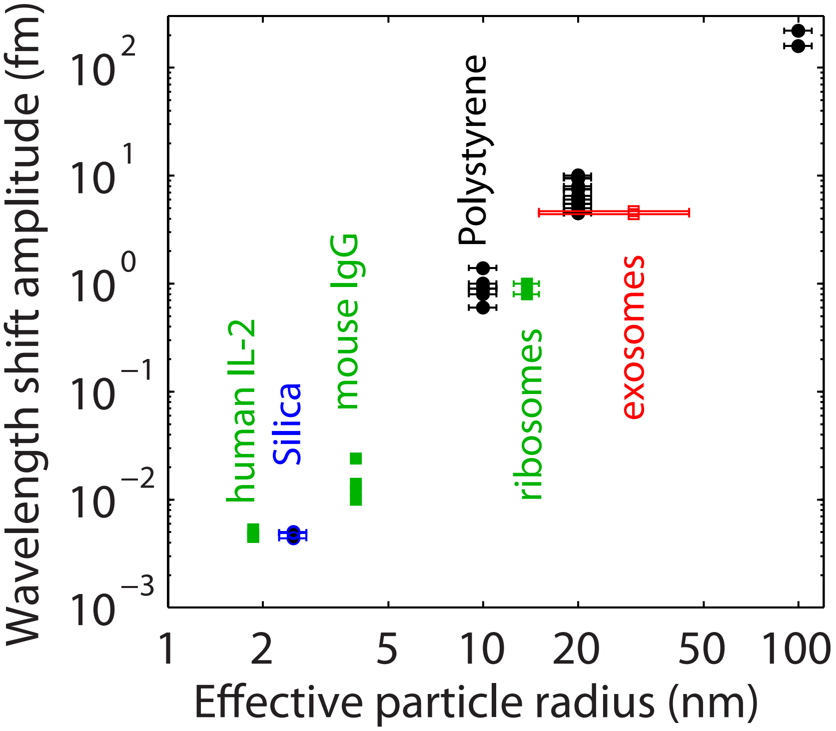

Figure 6.5: The maximum wavelength shift is plotted for a wide range of particle sizes with radii from 2–100 nm. For human IL-2 and mouse IgG, an effective particle radius was calculated based on spheres having the same molecular weights as the individual molecules.

found for the IL-2 experiments is summarized in Figure 6.5.

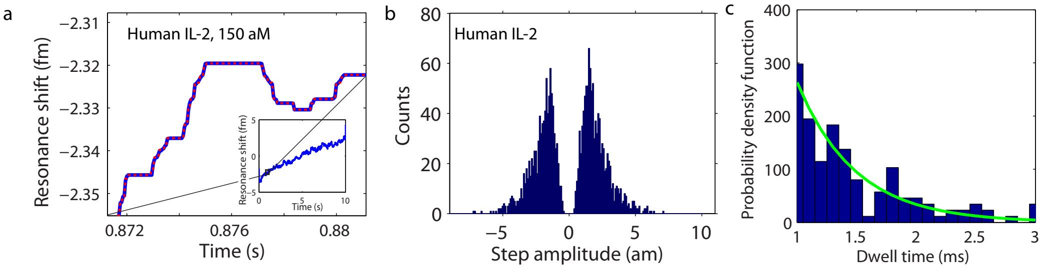

Figure 6.6: (a) The resonant wavelength shift (blue trace) over time of the microtoroid as human IL-2 molecules bind to the microtoroid's surface. The step-fit is shown in red. (inset) Zoom-out of the toroid response over the full recording range of 10 seconds. (b) Histogram of step amplitudes. Negative step amplitudes correspond to unbinding events. (c) Histogram of the time in between steps (dwell times). As expected for single-particle binding, the dwell time distribution follows an exponential fit (green).

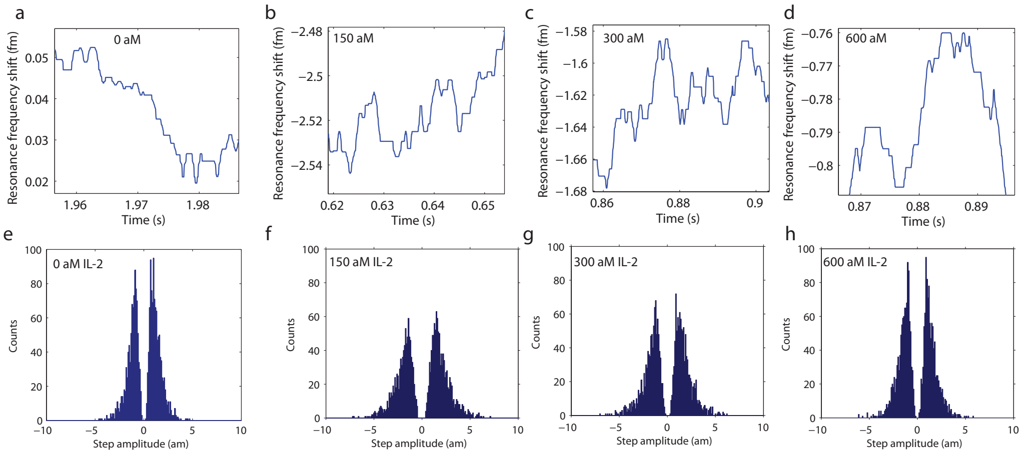

Figure 6.7: IL-2 detection data at four different concentrations. (a)–(d) Zoom-in of IL-2 step traces. Shown in blue is the resonance wavelength shift over time of the microtoroid as molecules bind to the microtoroid's surface. (e)–(h) Corresponding step amplitude histograms for (a)–(d). The buffer histogram is narrower than the histograms for the positive IL-2 concentrations, although the difference is very slight, indicating that these measurements are likely right at our sensitivity threshold. For increasing positive IL-2 concentrations, the buffer histograms show increasing numbers of steps, as expected. In the pure buffer case, the increased number of steps is an artifact of the step-finder where in the absence of larger steps, it finds a large number of small steps corresponding to buffer fluctuations.

6.2 Theoretical basis for particle detection

We note that this section was written by Stephen Arnold (NYU). Our experimental results yield a frequency shift upon protein binding that is not dependent on the circulating power over the range used in our experiments. This excludes the importance of a non-linear mechanism. In addition, the shifts being measured here are much smaller than the linewidth ($\sim$ 1 part in 10^5), which essentially eliminates the coupling between clockwise and counterclockwise modes. Fiber coupling only stimulates one of these circulating modes so a single protein-binding event corresponds to the interaction between a polarizable protein and a traveling wave resonator. **Theory for this circumstance was proposed in the past [18] but has not been tested at the single protein level because the experimental signals in the past have been masked by noise.** The current frequency locking technique overcomes past experimental limitations. In [18] the theory proposed that the shift in the photonic energy within the cavity is equivalent to the energy required for the reactive

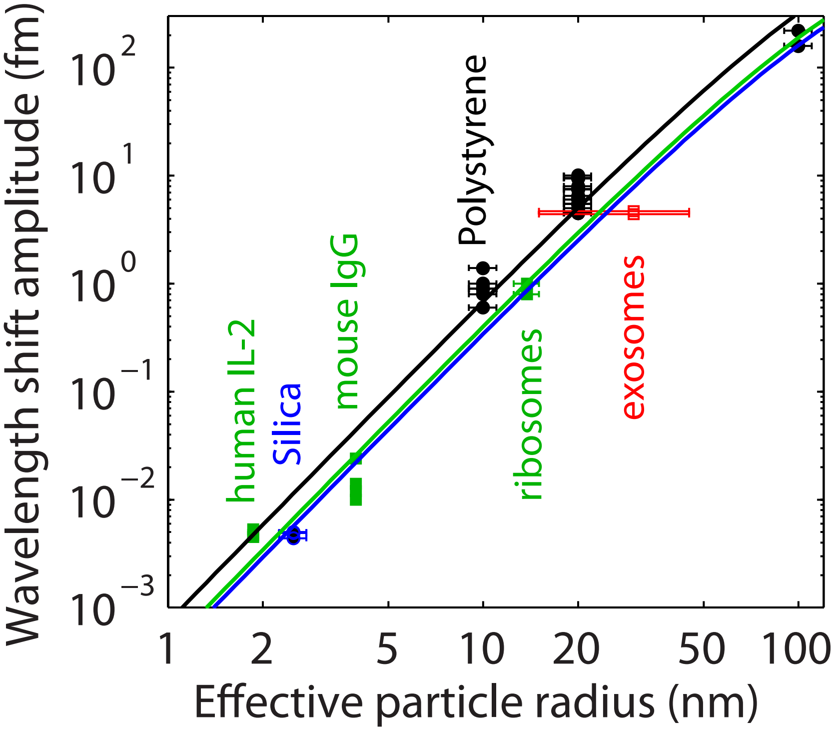

Figure 6.8: A wide range of particle sizes with radii from 2–100 nm were detected. For human IL-2 and mouse IgG, an effective particle radius was calculated based on spheres having the same molecular weights as the individual molecules. The solid lines are theoretical predictions based on the reactive sensing principle.

field to polarize the protein (Reactive Sensing Principle, RSP). It was computed as a first order perturbation, in which the field on the resonator surface is not modified by the binding event. On this basis the fractional frequency shift is the ratio of the energy required for the reactive field to polarize a protein, divided by the photonic energy in the cavity. Expressed in terms of the shift in the free space wavelength of a laser locked to resonance, this becomes:

$$\Delta\lambda = \frac{\alpha_{ex} E_0^2(r_p)}{2\int \varepsilon_r(r_c) E_0^2(r_c) dV}\lambda, \tag{6.1}$$

where ϵ_r is the relative permittivity of the cavity, and α_{ex} is the excess polarizability (with units of volume). For a spherical nanoparticle or protein α_{ex} is expressed as a dielectric factor D times the cube of an equivalent radius, $\alpha_{ex} = Da^3$. For a microspherical resonator Eq. 6.1 can be evaluated analytically, however for a toroid it is more convenient to recast the equation in terms of parameters

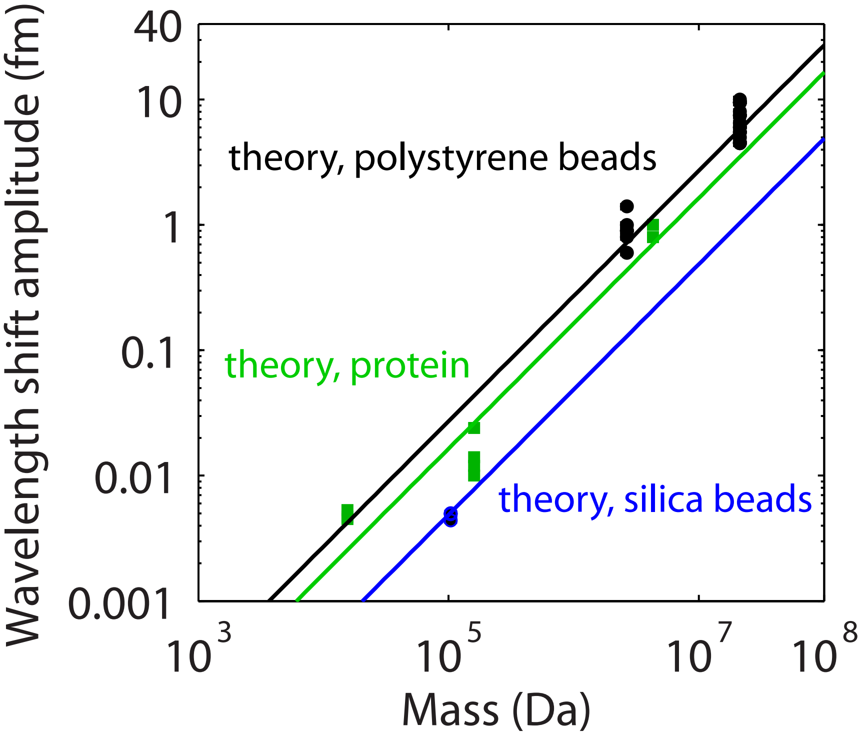

Figure 6.9: Wavelength shifts as a function of molecular weight for the same particles as shown in (a). Again, the experimental findings (points) agree well with theoretical predictions for different materials (solid lines).

that can be calculated numerically [81]. This involves dividing the numerator and denominator by the maximum intensity in the cavity, E^2_{max}. In this intensity normalized form the integral in the denominator is termed the optical mode volume, V_m. The most unique shift is for binding events at the equator (with the center of the protein at r_e from the center of the torus), where the shift for the lowest order mode is greatest. Eq. 6.1 becomes:

$$(\Delta\lambda)_{\max} = \frac{Da^3\left[E_0^2(r_e)/E^2{}_{\max}\right]}{2\,V_m}\lambda. \tag{6.2}$$

The particle's center is at r_e from the center of the torus, where $E_0^2(r_e)/E^2_{max} = 0.22\exp(-a/L)$, with $L \approx 120\mu m$. For the spherical nanoparticles the dielectric factor $D = 4\pi\, n_m{}^2(n_p^2 - n_m{}^2)/(n_p^2 + 2\,n_m{}^2)$, where n_m and n_p are the refractive indices of the medium (water) and nanoparticle, respectively. Each nanoparticle material in aqueous solution gives a different D ($D_{polystyrene} = 3.70$, $D_{protein} = 2.17$, $D_{SiO_2} = 1.85$), which explains the three lines in Figure 6.8. Agreement between theory and experiments in Figure 6.8, clearly validates the reactive mechanism. Next is the question of whether this mechanism can enable an estimate of molecular weight in solution.

Polarizability can be related to particle mass. This is especially the case for protein as evidenced from refractive index measurements in solution as concentration, c, is varied. As protein is dispersed into solution the refractive index of the solution increases. The change in the refractive index dn for a slight increase in concentration dc determines the differential refractive index dn/dc. For protein dn/dc = 0.185 cm^3/g, and varies by only about ∼1%. By treating the protein as a polarizable object, the polarizability can be shown to be directly proportional to the molecular weight of the protein M,

$$M = \frac{N_A \alpha_{ex}}{2n\varepsilon_0 \frac{dn}{dc}}, \tag{6.3}$$

where N_A is Avogadro's number, and n is the refractive index of water. By solving Eq. 6.2 for polarizability ($\alpha_{ex} = Da^3$), and substituting the result in Eq. 6.3, the molecular weight is:

$$M \approx \frac{c_p V_m}{\left[E_0^2(r_e)/E^2{}_{\max}\right]} \frac{(\Delta\lambda)_{\max}}{\lambda} \tag{6.4}$$

For silica and polystyrene we use dn/dc values of 0.05 [82] and 0.256 cm^3/g [83], respectively. We note that Equations 6.2 & 6.4 assume that isotropic particles bind to the equator. Anisotropic molecules produce shifts that are sensitive to their orientation relative to the polarization of the WGM. In cases where our assumption is not appropriate, an orientation factor is needed [84]. Figure 6.9 shows good agreement between the known molecular weights of our measured protein and Eq. 6.4, which provides further proof that we are detecting single protein molecules.

6.3 Conclusions

We have detected nanoparticles over a large range of sizes and have validated the applicability of FLOWER to bio-detection using exosomes, ribosomes, mouse immunoglobulin G, and human interleukin-2.

FLOWER has three main advantages:

1. Detection is in real time, as compared with scanning techniques.
2. The detection rate is much greater than what is possible using local plasmon enhancers without Q degradation.
3. Light forces are much more effective for drawing analyte to the sensor as compared with the scanning technique.

Our results support the ‘reactive’ model that suggests that the main contribution of the frequency shift upon particle binding is caused by the energy required for the reactive (evanescent) field to polarize the particle. With theory and experiment in good agreement, FLOWER provides a means for detecting single molecules in solution and identifying their molecular weights, thus paving the way for optically estimating the mass of single molecules in solution, fundamental studies in biophysics, and applications such as high throughput drug discovery and early detection of diseases.

Appendix A

Other projects

A.1 Integration with microfluidics

Several technological developments would make the toroids more robust and more reliable. These include: (1) integrating the microtoroid within a microfluidic system so that it is capable of performing multiple experiments in parallel with small sample volumes, (2) developing a stable linkage for biorecognition elements to the microtoroids surface without lowering the quality factor, and (3) making the microtoroid less sensitive to environmental perturbations. For high-throughput experimentation, integrating microtoroids with microfluidics is desirable. This poses a challenge, however, as light is launched into the toroid through an optical fiber that is extremely fragile, separate from the device, requires positioning with micrometer accuracy, and must exit to connect to the laser and the photodetector. Our way to meet this challenge is to fashion the microfluidic chip in two PDMS pieces, with the top half performing the traditional fluidic functions, and the bottom half serving as support (Figure A.1). Notches at both ends accommodate the optical fiber, which are sealed after positioning with UV-curable epoxy. Any further mechanical positioning of the fiber can be accomplished by gently squeezing the PDMS. Figure A.2 shows photographs of a microtoroid integrated within such a fluidic device. We are presently working on extending this design to accommodate multiple toroids for multiplexed detection.

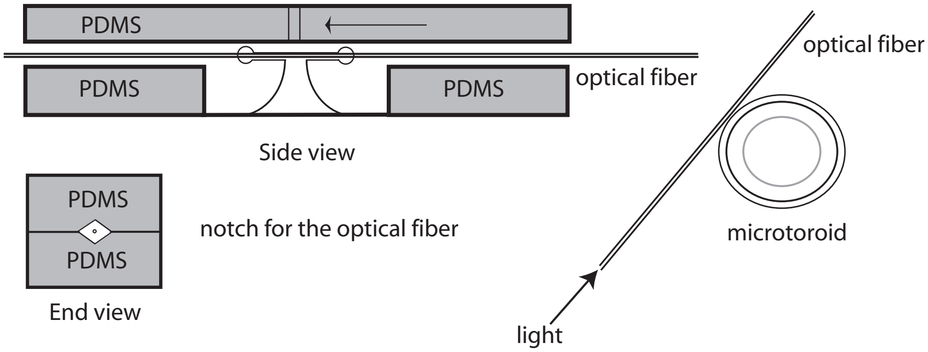

Figure A.1: Schematic of toroidal integration with microfluidics. The PDMS is fashioned in two halves, with the top half containing valves and channels for fluid handling. The notch for the optical fiber is sealed after fiber alignment.

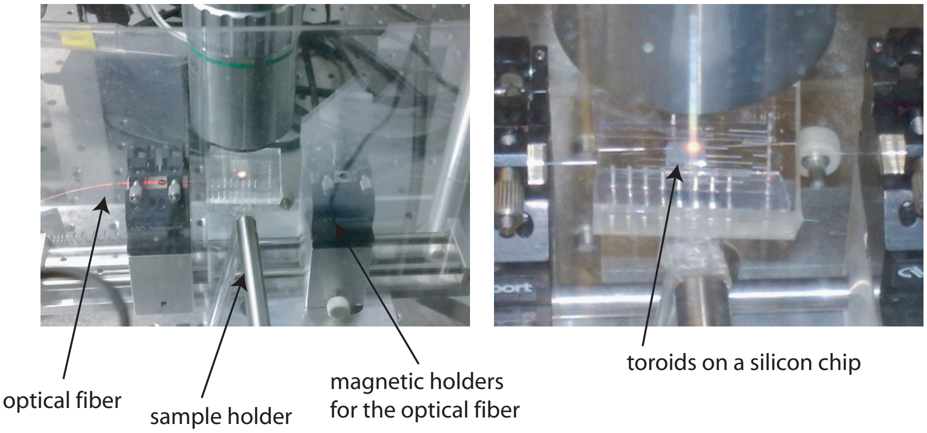

Figure A.2: Photographs of a microtoroid integrated with an optical fiber inside a microfluidic device. The successful incorporation of the optical fiber taper within a microfluidic device is the main hurdle towards integrating microtoroids with soft lithography based fluidics. The red light coming from the optical fiber and toroid is the laser light, indicating that the microtoroid was successfully coupled to the optical fiber taper.

A.2 Building a more robust biosensor

We have made the microtoroid less sensitive to environmental factors such as mechanical vibrations and temperature variations by exploiting mode splitting. Mode splitting is based on the interference between the two possible directions of light propagation (clockwise and counterclockwise) within the toroid. Usually these two modes have the same (degenerate) frequency, but a scattering site such as a nanoparticle or a biomolecules can perturb differentially these two modes, splitting the resonance into two separate peaks (Figure A.4A-C). Because these two peaks are from the same toroid, and experience the same environment, their absolute wavelengths should shift similarly; the distance between the peaks should be sensitive to the analyte but insensitive to environmental fluctuations [85]. Mode splitting has been used to robustly sense and size nanoparticles [85, 86]. Figure A.3 shows an example of mode splitting used for biodetection. A microtoroid with a double resonance peak in a pure buffer solution (Figure A.4A, separated by 46 MHz) was exposed to a solution containing IL-2, resulting in an increased distance between the two peaks (Figure A.4B). After the molecules were removed from the toroids surface, using an acidic solution, the peak-to-peak distance decreased (Figure A.4C).

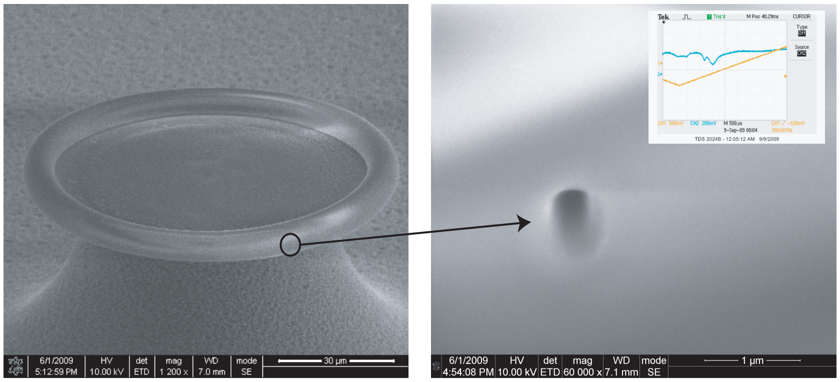

Figure A.3: Creating microtoroids optimized for mode splitting. A focused ion beam is used to generate a small dimple on the rim of the toroid. This small dimple acts as a scattering site which generates a resonance doublet (inset, blue line).

Since naturally randomly occurring resonance doublets are rare, we have created microtoroids with pre-existing resonance doublets by engineering a scattering site on the rim using a focused ion beam (Figure A.3). The scattering site breaks the symmetry of the microtoroid and results in a split resonance (Figure A.3, right (inset, blue line)). We are currently examining the performance of microtoroids with induced splits in this way.

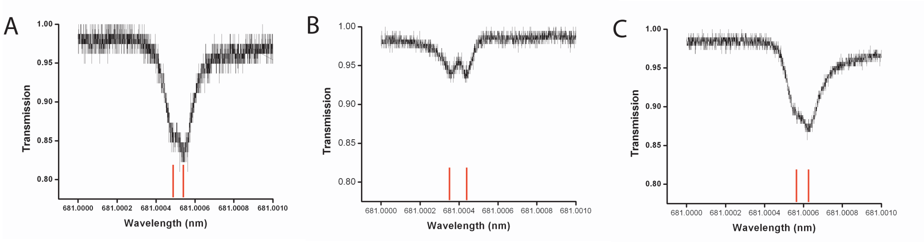

Figure A.4: As molecules bind and unbind to the microtoroid, the peak to peak distance correspondingly increases and decreases. (A) In buffer (Q $\sim$ 6.7x10^7), the distance between the two peaks (location marked by red lines) is 46 MHz. (B) The toroid is functionalized for the specific detection of IL-2 and IL-2 is flowed in. Following the addition of IL-2, the distance between the two peaks increases to 277 MHz. (C) IL-2 is unbound due to the addition of an acidic solution after which the distance between the two peaks decreases to 92 MHz.

Appendix B

Matlab programs

```
%% User settings
 clear all;
 close all;
%data = load('D:\3661839\Gd\Caltech\Data\031313\2b.txt');
%  data = load('D:\3661839\Gd\Caltech\Data\022513\600e.txt');
%  data = load('D:\3661839\Gd\Caltech\Data\030513\150.txt');
data = load('150.txt');
Fsamp = 20e3; %Sampling frequency in Hz
filterByZeroMult = true;

%% Load Data
yRaw = data(:,2).';
NRaw = length(yRaw);
dt = 1/Fsamp;
tRaw = dt*(0:NRaw-1);

figure(1);
plot(tRaw,yRaw,'k');
title('yRaw');
xlabel('Time (s)');
ylabel('Voltage (V)');

```

```
%% Remove linear bias for better linear filtering
coeffs = polyfit(tRaw,yRaw,1);
linBias = (coeffs(1)*tRaw + coeffs(2));
yPreFilt = yRaw - linBias;

%% Compute FFT
Y = fft(yPreFilt);
dF = Fsamp/NRaw;
f = dF*(0:NRaw-1);

%% Plot data frequency content
fNyq = Fsamp/2;

figure(2);
subplot(311);
semilogy(f,abs(Y).^2/NRaw);
xlim([0,fNyq]);
xlabel('Freqency (Hz)');
ylabel('FFT Power Spec.');

subplot(312);
plot(f,unwrap(angle(Y)));
xlim([0,fNyq]);
xlabel('Freqency (Hz)');
ylabel('arg(FFT)');

subplot(313);
semilogy(abs(Y).^2/NRaw);
xlim([0,NRaw/2]);
xlabel('Index');
ylabel('FFT Power Spec.');

%% Remove 2kHz Dither
Y_posF = Y(1:NRaw/2);
```

```
Y_negF = fliplr(Y(NRaw/2+1:end));
f_subNyq = dF*(0:NRaw/2-1);

%Filter using low-pass:
    cutoff = 1e3; %Hz
    sharpness = 100;
    if filterByZeroMult
        filterFunc = ones(1,NRaw/2);
        filterFunc(f_subNyq > cutoff) = 0;
    else
        filterFunc = (1 + exp(sharpness*(f_subNyq/cutoff - 1))).^(-1);
    end

    Y_posF = Y_posF.*filterFunc;
    Y_negF = Y_negF.*filterFunc;



%Filter out specific bands only:
%     ditherCenters = 2e3:2e3:fNyq; %Hz
%     ditherBW = 70; %Radius to remove line noise at each center (Hz);
%     subCentSpacing = 60; %Hz -- for removing nonlinear mixing between line noise ...
    and dither
%     numSubCent = 7;
%     subBW = 8; %Hz
%
%     numDitherCenters = length(ditherCenters);
%     for q=1:numDitherCenters
%         if filterByZeroMult
%             ampPosF = 0;
%             phPosF = 1;
%             ampNegF = 0;
%             phNegF = 1;
%         else
```

```
%             ampPosF = median(abs(Y_posF( (abs(f_subNyq-ditherCenters(q)) < ...
    2*ditherBW) & ...
%                 (abs(f_subNyq-ditherCenters(q)) > ditherBW) )));
%             phPosF = mean(angle(Y_posF( (abs(f_subNyq-ditherCenters(q)) < ...
    2*ditherBW) & ...
%                 (abs(f_subNyq-ditherCenters(q)) > ditherBW) )));
%
%             ampNegF = median(abs(Y_negF( (abs(f_subNyq-ditherCenters(q)) < ...
    2*ditherBW) & ...
%                 (abs(f_subNyq-ditherCenters(q)) > ditherBW) )));
%             phNegF = mean(angle(Y_negF( (abs(f_subNyq-ditherCenters(q)) < ...
    2*ditherBW) & ...
%                 (abs(f_subNyq-ditherCenters(q)) > ditherBW) )));
%         end;
%
%         Y_posF( abs(f_subNyq-ditherCenters(q)) < ditherBW ) = ...
%             ampPosF * exp(1i*phPosF);
%         Y_negF( abs(f_subNyq-ditherCenters(q)) < ditherBW ) = ...
%             ampNegF * exp(1i*phNegF);
%
%         %Filter out nonlinear mixing between dither frequency and line
%         %frequency
%         for s = -numSubCent : 1 : numSubCent
%             if filterByZeroMult
%                 ampPosF = 0;
%                 phPosF = 1;
%                 ampNegF = 0;
%                 phNegF = 1;
%             else
%                 ampPosF = median(abs(Y_posF( (abs(f_subNyq-...
%                     (ditherCenters(q)+s*subCentSpacing)) < 2*subBW) & ...
%                     (abs(f_subNyq-(ditherCenters(q)+s*subCentSpacing)) > subBW) )));
%                 phPosF = mean(angle(Y_posF( (abs(f_subNyq-...
%                     (ditherCenters(q)+s*subCentSpacing)) < 2*subBW) & ...
```

```
%                     (abs(f_subNyq-(ditherCenters(q)+s*subCentSpacing)) > subBW) )));
%
%                 ampNegF = median(abs(Y_negF( (abs(f_subNyq-...
%                     (ditherCenters(q)+s*subCentSpacing)) < 2*subBW) & ...
%                     (abs(f_subNyq-(ditherCenters(q)+s*subCentSpacing)) > subBW) )));
%                 phNegF = mean(angle(Y_negF( (abs(f_subNyq-...
%                     (ditherCenters(q)+s*subCentSpacing)) < 2*subBW) & ...
%                     (abs(f_subNyq-(ditherCenters(q)+s*subCentSpacing)) > subBW) )));
%             end
%             Y_posF( abs(f_subNyq-(ditherCenters(q)+s*subCentSpacing)) < subBW ) ... = ...
%                 ampPosF * exp(1i*phPosF);
%             Y_negF( abs(f_subNyq-(ditherCenters(q)+s*subCentSpacing)) < subBW ) ... = ...
%                 ampNegF * exp(1i*phNegF);
%         end
%     end

Y_dithFilt = [Y_posF fliplr(Y_negF)];

figure(2);
subplot(311); hold on;
semilogy(f,abs(Y_dithFilt).^2/NRaw,'g'); hold off;
ylim([1e-15,1]);

subplot(312); hold on;
plot(f,unwrap(angle(Y_dithFilt)),'g'); hold off;

subplot(313); hold on;
semilogy(abs(Y_dithFilt).^2/NRaw,'g'); hold off;

y_dithFilt = real(ifft(Y_dithFilt));

figure(1);
```

```
hold on;
plot(tRaw,y_dithFilt+linBias,'g'); hold off;

%% Remove line noise
Y_posF = Y_dithFilt(1:NRaw/2);
Y_negF = fliplr(Y_dithFilt(NRaw/2+1:end));
f_subNyq = dF*(0:NRaw/2-1);

lineCenters = 60:60:fNyq; %Hz
lineBW = 8; %Radius to remove line noise at each center (Hz); (used 6 for exosomes)

numLineCenters = length(lineCenters);
for q=1:numLineCenters
    if filterByZeroMult
        ampPosF = 0;
        phPosF = 1;
        ampNegF = 0;
        phNegF = 1;
    else
        ampPosF = mean(abs(Y_posF( (abs(f_subNyq-lineCenters(q)) < 2*lineBW) & ...
            (abs(f_subNyq-lineCenters(q)) > lineBW) )));
        phPosF = mean(angle(Y_posF( (abs(f_subNyq-lineCenters(q)) < 2*lineBW) & ...
            (abs(f_subNyq-lineCenters(q)) > lineBW) )));

        ampNegF = median(abs(Y_negF( (abs(f_subNyq-lineCenters(q)) < 2*lineBW) & ...
            (abs(f_subNyq-lineCenters(q)) > lineBW) )));
        phNegF = mean(angle(Y_negF( (abs(f_subNyq-lineCenters(q)) < 2*lineBW) & ...
            (abs(f_subNyq-lineCenters(q)) > lineBW) )));
    end

    Y_posF( abs(f_subNyq-lineCenters(q)) < lineBW ) = ...
        ampPosF * exp(1i*phPosF);
    Y_negF( abs(f_subNyq-lineCenters(q)) < lineBW ) = ...
        ampNegF * exp(1i*phNegF);
```

```
end

Y_lineFilt = [Y_posF fliplr(Y_negF)];

figure(2);
subplot(311); hold on;
semilogy(f,abs(Y_lineFilt).^2/NRaw,'r'); hold off;

subplot(312); hold on;
plot(f,unwrap(angle(Y_lineFilt)),'r'); hold off;

subplot(313); hold on;
semilogy(abs(Y_lineFilt).^2/NRaw,'r'); hold off;

y_lineFilt = real(ifft(Y_lineFilt));

figure(1);
hold on;
plot(tRaw,y_lineFilt+linBias,'r'); hold off;

%% Remove 100 Hz multiples noise
Y_posF = Y_lineFilt(1:NRaw/2);
Y_negF = fliplr(Y_lineFilt(NRaw/2+1:end));
f_subNyq = dF*(0:NRaw/2-1);

lineCenters = 100:100:fNyq; %Hz
lineBW = 6; %Radius to remove line noise at each center (Hz);

numLineCenters = length(lineCenters);
for q=1:numLineCenters
    if filterByZeroMult
        ampPosF = 0;
        phPosF = 1;
        ampNegF = 0;
```

```
        phNegF = 1;
    else
        ampPosF = mean(abs(Y_posF( (abs(f_subNyq-lineCenters(q)) < 2*lineBW) & ...
            (abs(f_subNyq-lineCenters(q)) > lineBW) )));
        phPosF = mean(angle(Y_posF( (abs(f_subNyq-lineCenters(q)) < 2*lineBW) & ...
            (abs(f_subNyq-lineCenters(q)) > lineBW) )));

        ampNegF = median(abs(Y_negF( (abs(f_subNyq-lineCenters(q)) < 2*lineBW) & ...
            (abs(f_subNyq-lineCenters(q)) > lineBW) )));
        phNegF = mean(angle(Y_negF( (abs(f_subNyq-lineCenters(q)) < 2*lineBW) & ...
            (abs(f_subNyq-lineCenters(q)) > lineBW) )));
    end
    Y_posF( abs(f_subNyq-lineCenters(q)) < lineBW ) = ...
        ampPosF * exp(1i*phPosF);
    Y_negF( abs(f_subNyq-lineCenters(q)) < lineBW ) = ...
        ampNegF * exp(1i*phNegF);
end

Y_100Filt = [Y_posF fliplr(Y_negF)];

figure(2);
subplot(311); hold on;
semilogy(f,abs(Y_100Filt).^2/NRaw,'c'); hold off;

subplot(312); hold on;
plot(f,unwrap(angle(Y_100Filt)),'c'); hold off;

subplot(313); hold on;
semilogy(abs(Y_100Filt).^2/NRaw,'c'); hold off;

y_100Filt = real(ifft(Y_100Filt));

figure(1);
hold on;
```

```
plot(tRaw,y_100Filt+linBias,'c'); hold off;

%% Remove 3.5 kHz broad peak
%Use this line if rest of cell is disabled:
%Y_allFilt = Y_100Filt;

Y_posF = Y_100Filt(1:NRaw/2);
Y_negF = fliplr(Y_100Filt(NRaw/2+1:end));
f_subNyq = dF*(0:NRaw/2-1);

% lineCenters = 6000:6000:fNyq; %Hz
% lineBW = 4000; %Radius to remove line noise at each center (Hz);
lineCenters = 3500:3500:fNyq; %Hz
lineBW = 1000; %Radius to remove line noise at each center (Hz);

numLineCenters = length(lineCenters);
for q=1:numLineCenters
    ampPosF = mean(abs(Y_posF( (abs(f_subNyq-lineCenters(q)) < 2*lineBW) & ...
        (abs(f_subNyq-lineCenters(q)) > lineBW) )));
    phPosF = mean(angle(Y_posF( (abs(f_subNyq-lineCenters(q)) < 2*lineBW) & ...
        (abs(f_subNyq-lineCenters(q)) > lineBW) )));

    Y_posF( abs(f_subNyq-lineCenters(q)) < lineBW ) = ...
        ampPosF * exp(1i*phPosF);
%     Y_posF( abs(f_subNyq-lineCenters(q)) < lineBW ) = 0;

    ampNegF = median(abs(Y_negF( (abs(f_subNyq-lineCenters(q)) < 2*lineBW) & ...
        (abs(f_subNyq-lineCenters(q)) > lineBW) )));
    phNegF = mean(angle(Y_negF( (abs(f_subNyq-lineCenters(q)) < 2*lineBW) & ...
        (abs(f_subNyq-lineCenters(q)) > lineBW) )));

    Y_negF( abs(f_subNyq-lineCenters(q)) < lineBW ) = ...
        ampNegF * exp(1i*phNegF);
%     Y_negF( abs(f_subNyq-lineCenters(q)) < lineBW ) = 0;
```

```
end

Y_allFilt = [Y_posF fliplr(Y_negF)];

%% Plot final filtered data:
figure(2);
subplot(311); hold on;
semilogy(f,abs(Y_allFilt).^2/NRaw,'m'); hold off;

subplot(312); hold on;
plot(f,unwrap(angle(Y_allFilt)),'m'); hold off;

subplot(313); hold on;
semilogy(abs(Y_allFilt).^2/NRaw,'m'); hold off;

y_allFilt = real(ifft(Y_allFilt));

figure(1);
hold on;
plot(tRaw,y_allFilt+linBias,'m'); hold off;

legend('Raw data','2kHz Removed','60Hz Removed','100Hz Removed','Final filtered')


meanCenter = mean(y_allFilt+linBias);
yUnshift_fm  = 31000*(y_allFilt+linBias-meanCenter);
figure(3);
plot(tRaw,yUnshift_fm,'k');
title('y Filtered');
xlabel('Time (s)');
ylabel('Shift (fm)');

%%Do a moving average
% yMA = smooth(yUnshift_fm,1001);
```

```
% figure(3); hold on;
% plot(tRaw,yMA,'r'); hold off;
%
% ysample = yMA((tRaw > 4.8) & (tRaw < 4.9));
% std(ysample)


%% Apply nonlinear fitting:
%Total variation filter
% %     mfSizes = [1e-4 5e-4 1e-3 1e-2];
%     mfSizes = 5e-4;
%     mfColors = ['r','b','c','m','y','b'];
%     numMFs = length(mfSizes);
%
%     y_preTV = y_allFilt+linBias;
%     y_preTV(tRaw < .5) = mean(y_preTV( (tRaw≥.5) & (tRaw<0.51)));
%     y_preTV(tRaw > 9.5) = mean(y_preTV( (tRaw>9.49) & (tRaw≤9.5)));
%
%     lmax = tvdiplmax(y_preTV);
%     [y_mf, E, status] = tvdip(y_preTV,lmax*mfSizes,1,1e-3,1000);
%     y_mf = y_mf.';

%Median Filter:
     %mfSizes = [5,11,101,1001];
    mfSizes = 1001;
    mfColors = ['r','b','c','m','y','b'];
    numMFs = length(mfSizes);
    y_mf = zeros(numMFs,NRaw);
    for m = 1:numMFs
        if mfSizes(m) ≤ 1001
            y_mf(m,:) = medfilt1(y_allFilt+linBias,mfSizes(m));
        else
            y_mf(m,:) = medfilt1(y_allFilt+linBias,mfSizes(m),NRaw/100);
        end
```

```
    end

figure(3); hold on;
for m=1:numMFs
    if m == numMFs
        linwid = 1;
    else
        linwid = 1;
    end
    plot(tRaw,31000*(y_mf(m,:)-meanCenter),mfColors(m),'LineWidth',linwid);
end
hold off;
% legend('Linearly-filtered ...
    data',sprintf('\\lambda=%0.2e',mfSizes(1)),sprintf('\\lambda=%0.2e',mfSizes(2)),sprintf('\\lambda=
% legend('Linearly-filtered data',sprintf('Median Window ...
    %d',mfSizes(1)),sprintf('Median Window %d',mfSizes(2)),sprintf('Median Window ...
    %d',mfSizes(3)),sprintf('Median Window %d',mfSizes(4)));
title('y With Median or TV Filters');
xlabel('Time (s)');
ylabel('Shift (fm)');

%% Write output:
timeInterval = [5,5.5]; %s
keeps = 1; %keep every nth point

fileNames = cell(1,numMFs+1);
for m=1:numMFs
    if m==0 %Save the version with just linear filtering (no Median)
        yOut = 31000*(y_allFilt+linBias-meanCenter);
        fileName = 'FilteredNoMF.txt';
    else
      yOut = 31000*(y_mf(m,:)-meanCenter);
        fileName = ['FilteredMF' num2str(mfSizes(m)) '.txt'];
    end
```

```

    yOut = yOut(1:keeps:end);
    tOut = tRaw(1:keeps:end);

    M = [];
    M(:,1)= tOut((tOut ≥ timeInterval(1)) & (tOut ≤ timeInterval(2)))';
    M(:,2)=yOut((tOut ≥ timeInterval(1)) & (tOut ≤ timeInterval(2)))';
    dlmwrite(fileName, M, 'delimiter', '\t', 'precision', 6);

    fileNames{m+1} = fileName;
end



%% Do steps finder
data = cell(1,numMFs);
indexes = cell(1,numMFs);
lijst = cell(1,numMFs);
properties = cell(1,numMFs);
initval = cell(1,numMFs);
for m=1:numMFs
    figure(4);
    [data{m+1}, indexes{m+1},lijst{m+1},properties{m+1},initval{m+1}]=...
        Steps_Find(fileNames{m+1});
    fprintf('Done step pre—scanning for filter %d of %d.\n',m,numMFs);
end

%% Do second part of steps finder
% stepNumbers = [500,1000];
stepNumbers = [200,300,400];
numStepNums = length(stepNumbers);

stepInfo = cell(numMFs+1,numStepNums);
for m = 1:numMFs
```

```
    for s = 1:numStepNums
        figure(); %5
        stepInfo{m+1,s}=Steps_Evaluate(data{m+1},indexes{m+1},lijst{m+1},...
            properties{m+1},initval{m+1},stepNumbers(s));
        fprintf('Done with step set %d of %d.\n',s,numStepNums);
    end
    fprintf('Done step finding for filter %d of %d.\n',m,numMFs);
end

%% Plot results
% binCenters = -3 : 0.2 : 6;
% binCenters = -.2 : 0.007 : .2;
binCenters = -.02 : 0.001 : .02;

for m = 1:numMFs
    figNum = 50+m;
    figure(figNum);
    for s = 1:numStepNums
        stepAmplitudes = stepInfo{m+1,s}(5,:);
        [muhat,sigmahat] = normfit(stepAmplitudes);
        xtest = linspace(binCenters(1),binCenters(end),1000);
        ytest = length(stepAmplitudes)*(binCenters(2)-binCenters(1))/...
            sigmahat/sqrt(2*pi) * exp(-(xtest-muhat).^2./(2*sigmahat^2));

        subplot(2,3,s);
        hist(stepAmplitudes,binCenters);
        hold on;
        plot(xtest,ytest,'r','LineWidth',2);
        hold off;
        h = findobj(gca,'Type','patch');
        set(h,'FaceColor','k','EdgeColor',[0.4,0.4,0.4])
        xlabel('Shift (fm)');
%         if m == 0
%             title(sprintf('No med filt; %d steps',stepNumbers(s)));
```

```
%         else
%             title(sprintf('Med filt %d; %d steps',mfSizes(m),stepNumbers(s)));
%         end
        if m == 0
            title(sprintf('%d steps',stepNumbers(s)));
        else
            title(sprintf('%d steps',stepNumbers(s)));
        end
        xlim([0.9*binCenters(1),1.1*binCenters(end)]);
%         ylim([0,25]); %22 or 13
    end
end
```

Appendix C

Paper draft

Bibliography

[1] Matthew Cooper. *Label-free biosensors: techniques and applications.* Cambridge University Press, 2009.

[2] Alexander E Knight. *Single molecule biology.* Academic Press, 2009.

[3] Tomas Hirschfeld. Optical microscopic observation of single small molecules. *Applied optics*, 15(12):2965–2966, 1976.

[4] Ido Braslavsky, Benedict Hebert, Emil Kartalov, and Stephen R Quake. Sequence information can be obtained from single DNA molecules. *Proceedings of the National Academy of Sciences*, 100(7):3960–3964, 2003.

[5] Yoshiyuki Suzuki and Kunihiko Suzuki. Specific radioactive labeling of terminal N-acetylgalactosamine of glycosphingolipids by the galactose oxidase–sodium borohydride method. *Journal of lipid research*, 13(5):687–690, 1972.

[6] Kerry J Vahala. Optical microcavities. *Nature*, 424(6950):839–846, 2003.

[7] Kerry Vahala. *Optical microcavities.* World Scientific Publishing Company, 2004.

[8] Thomas P Burg, Michel Godin, Scott M Knudsen, Wenjiang Shen, Greg Carlson, John S Foster, Ken Babcock, and Scott R Manalis. Weighing of biomolecules, single cells and single nanoparticles in fluid. *Nature*, 446(7139):1066–1069, 2007.

[9] YT Yang, Carlo Callegari, XL Feng, KL Ekinci, and ML Roukes. Zeptogram-scale nanomechanical mass sensing. *Nano letters*, 6(4):583–586, 2006.

[10] Eric Stern, James F Klemic, David A Routenberg, Pauline N Wyrembak, Daniel B Turner-Evans, Andrew D Hamilton, David A LaVan, Tarek M Fahmy, and Mark A Reed. Label-free immunodetection with CMOS-compatible semiconducting nanowires. *Nature*, 445(7127):519–522, 2007.

[11] P Bergveld. Development of an ion-sensitive solid-state device for neurophysiological measurements. *Biomedical Engineering, IEEE Transactions on*, (1):70–71, 1970.

[12] Matthew Fivash, Eric M Towler, and Robert J Fisher. BIAcore for macromolecular interaction. *Current opinion in biotechnology*, 9(1):97–101, 1998.

[13] Rebecca L Rich and David G Myszka. Advances in surface plasmon resonance biosensor analysis. *Current opinion in biotechnology*, 11(1):54–61, 2000.

[14] Lord Rayleigh. CXII. The problem of the whispering gallery. *Philosophical Magazine Series 6*, 20(120):1001–1004, Dec 1910.

[15] Frank Vollmer and Stephen Arnold. Whispering-gallery-mode biosensing: label-free detection down to single molecules. *Nature methods*, 5(7):591–596, 2008.

[16] A Serpengüzel, S Arnold, and G Griffel. Excitation of resonances of microspheres on an optical fiber. *Optics Letters*, 20(7):654–656, 1995.

[17] A Serpengüzel, Steve Arnold, Giora Griffel, and James A Lock. Enhanced coupling to microsphere resonances with optical fibers. *JOSA B*, 14(4):790–795, 1997.

[18] S Arnold, M Khoshsima, I Teraoka, S Holler, and F Vollmer. Shift of whispering-gallery modes in microspheres by protein adsorption. *Optics Letters*, 28(4):272–274, 2003.

[19] F Vollmer, D Braun, A Libchaber, M Khoshsima, I Teraoka, and S Arnold. Protein detection by optical shift of a resonant microcavity. *Applied Physics Letters*, 80(21):4057–4059, 2002.

[20] Giora Griffel, Stephen Arnold, Dogan Taskent, Ali Serpengüzel, John Connolly, and Nancy Morris. Morphology-dependent resonances of a microsphere-optical fiber system. *Optics Letters*, 21(10):695–697, 1996.

[21] VR Dantham, S Holler, V Kolchenko, Z Wan, and S Arnold. Taking whispering gallery-mode single virus detection and sizing to the limit. *Applied Physics Letters*, 101(4):043704–043704, 2012.

[22] Frank Vollmer, Stephen Arnold, Dieter Braun, Iwao Teraoka, and Albert Libchaber. Multiplexed DNA quantification by spectroscopic shift of two microsphere cavities. *Biophysical Journal*, 85(3):1974–1979, 2003.

[23] Stephen Arnold. Microspheres, Photonic Atoms and the Physics of Nothing Light can become trapped within tiny, transparent spheres. The surprising properties that result may turn" microsphere photonics" into an important new technology. *American Scientist*, 89(5):414–421, 2001.

[24] Hai-Cang Ren, Frank Vollmer, Stephen Arnold, and Albert Libchaber. High-Q microsphere biosensor-analysis for adsorption of rodlike bacteria. *Opt. Express*, 15(25):17410–17423, 2007.

[25] Adam L Washburn, Matthew S Luchansky, Adrienne L Bowman, and Ryan C Bailey. Quantitative, label-free detection of five protein biomarkers using multiplexed arrays of silicon photonic microring resonators. *Analytical chemistry*, 82(1):69–72, 2009.

[26] Ryan C Bailey, Adam L Washburn, Abraham J Qavi, Muzammil Iqbal, Martin Gleeson, Frank Tybor, and L Cary Gunn. A robust silicon photonic platform for multiparameter biological analysis. In *SPIE OPTO: Integrated Optoelectronic Devices*, pages 72200N–72200N. International Society for Optics and Photonics, 2009.

[27] Xudong Fan, Ian M White, Siyka I Shopova, Hongying Zhu, Jonathan D Suter, Yuze Sun, and Gilmo Yang. Optofluidic ring resonator biological and chemical sensors. *Practical Applications of Microresonators in Optics and Photonics*, page 385, 2010.

[28] Matthew S Luchansky and Ryan C Bailey. Silicon photonic microring resonators for quantitative cytokine detection and T-cell secretion analysis. *Analytical chemistry*, 82(5):1975–1981, 2010.

[29] Matthew S Luchansky, Adam L Washburn, Teresa A Martin, Muzammil Iqbal, L Cary Gunn, and Ryan C Bailey. Characterization of the evanescent field profile and bound mass sensitivity of a label-free silicon photonic microring resonator biosensing platform. *Biosensors and Bioelectronics*, 26(4):1283–1291, 2010.

[30] Matthew S Luchansky, Adam L Washburn, Melinda S McClellan, and Ryan C Bailey. Sensitive on-chip detection of a protein biomarker in human serum and plasma over an extended dynamic range using silicon photonic microring resonators and sub-micron beads. *Lab on a Chip*, 11(12):2042–2044, 2011.

[31] Abraham J Qavi, Jared T Kindt, Martin A Gleeson, and Ryan C Bailey. Anti-DNA: RNA antibodies and silicon photonic microring resonators: increased sensitivity for multiplexed microRNA detection. *Analytical chemistry*, 83(15):5949–5956, 2011.

[32] Abraham J Qavi, Thomas M Mysz, and Ryan C Bailey. Isothermal discrimination of single-nucleotide polymorphisms via real-time kinetic desorption and label-free detection of DNA using silicon photonic microring resonator arrays. *Analytical chemistry*, 83(17):6827–6833, 2011.

[33] Matthew S Luchansky and Ryan C Bailey. Rapid, multiparameter profiling of cellular secretion using silicon photonic microring resonator arrays. *Journal of the American Chemical Society*, 133(50):20500–20506, 2011.

[34] Adam L Washburn and Ryan C Bailey. Photonics-on-a-chip: recent advances in integrated waveguides as enabling detection elements for real-world, lab-on-a-chip biosensing applications. *Analyst*, 136(2):227–236, 2011.

[35] Ott Scheler, Jared T Kindt, Abraham J Qavi, Lauris Kaplinski, Barry Glynn, Thomas Barry, Ants Kurg, and Ryan C Bailey. Label-free, multiplexed detection of bacterial tmRNA using silicon photonic microring resonators. *Biosensors and Bioelectronics*, 36(1):56–61, 2012.

[36] Melinda S McClellan, Leslie L Domier, and Ryan C Bailey. Label-free virus detection using silicon photonic microring resonators. *Biosensors and Bioelectronics*, 31(1):388–392, 2012.

[37] Ji-Yeon Byeon, FT Limpoco, and Ryan C Bailey. Efficient bioconjugation of protein capture agents to biosensor surfaces using aniline-catalyzed hydrazone ligation. *Langmuir*, 26(19):15430–15435, 2010.

[38] Abraham J Qavi, Adam L Washburn, Ji-Yeon Byeon, and Ryan C Bailey. Label-free technologies for quantitative multiparameter biological analysis. *Analytical and bioanalytical chemistry*, 394(1):121–135, 2009.

[39] Ji-Yeon Byeon and Ryan C Bailey. Multiplexed evaluation of capture agent binding kinetics using arrays of silicon photonic microring resonators. *Analyst*, 136(17):3430–3433, 2011.

[40] F Ted Limpoco and Ryan C Bailey. Real-Time Monitoring of Surface-Initiated Atom Transfer Radical Polymerization Using Silicon Photonic Microring Resonators: Implications for Combinatorial Screening of Polymer Brush Growth Conditions. *Journal of the American Chemical Society*, 133(38):14864–14867, 2011.

[41] Abraham J Qavi, Jared T Kindt, and Ryan C Bailey. Sizing up the future of microRNA analysis. *Analytical and bioanalytical chemistry*, 398(6):2535–2549, 2010.

[42] Adam L Washburn, Joseph Gomez, and Ryan C Bailey. DNA-encoding to improve performance and allow parallel evaluation of the binding characteristics of multiple antibodies in a surface-bound immunoassay format. *Analytical chemistry*, 83(9):3572–3580, 2011.

[43] Lina He, Şahin Kaya Özdemir, Jiangang Zhu, and Lan Yang. Ultrasensitive detection of mode splitting in active optical microcavities. *Physical Review A*, 82(5):053810, 2010.

[44] D. K. Armani, T. J. Kippenberg, S. M. Spillane, and K. J. Vahala. Ultra-high-Q toroid microcavity on a chip. *Nature*, 421(6926):925–928, Feb 2003.

[45] Heather K Hunt and Andrea M Armani. Label-free biological and chemical sensors. *Nanoscale*, 2(9):1544–1559, 2010.

[46] Tobias J Kippenberg and KJ Vahala. Demonstration of High-Q Microdisk Resonators: Fabrication and Nonlinear Properties. *Lasers and Electro-Optics. Baltimore, MD*, 2007.

[47] Tobias Jan August Kippenberg. *Nonlinear optics in ultra-high-Q whispering-gallery optical microcavities.* PhD thesis, California Institute of Technology, 2004.

[48] K Vahala, T Carmon, H Roksari, T Kippenberg, A Armani, and D Armani. Photonic clocks, Raman lasers, and Biosensors on Silicon. In *Lasers and Electro-Optics Society, 2006. LEOS 2006. 19th Annual Meeting of the IEEE*, pages 40–41. IEEE, 2006.

[49] Katrien De Vosa, Jordi Gironesb, Yannick De Konincka, Etienne Schachtb, Peter Bienstmana, and Roel Baetsa. Multiplexed protein detection with an array of silicon-on-insulator microring resonators. In *LEOS Annual Meeting Conference Proceedings, 2009. LEOS'09. IEEE*, pages 457–458. IEEE, 2009.

[50] Tao Lu, Hansuek Lee, Tong Chen, Steven Herchak, Ji-Hun Kim, Scott E Fraser, Richard C Flagan, and Kerry Vahala. High sensitivity nanoparticle detection using optical microcavities. *Proceedings of the National Academy of Sciences*, 108(15):5976–5979, 2011.

[51] Todd M Squires, Robert J Messinger, and Scott R Manalis. Making it stick: convection, reaction and diffusion in surface-based biosensors. *Nature biotechnology*, 26(4):417–426, 2008.

[52] Andrea M. Armani, Rajan P. Kulkarni, Scott E. Fraser, Richard C. Flagan, and Kerry J. Vahala. Label-free, single-molecule detection with optical microcavities. *Science*, 317(5839):783–787, Aug 2007.

[53] J. L. Arlett, E. B. Myers, and M. L. Roukes. Comparative advantages of mechanical biosensors. *Nat Nanotechnol*, 6(4):203–215, Apr 2011.

[54] S Arnold, SI Shopova, and S Holler. Whispering gallery mode bio-sensor for label-free detection of single molecules: thermo-optic vs. reactive mechanism. *Optics Express*, 18(1):281–287, 2010.

[55] Matthew S Luchansky and Ryan C Bailey. High-Q optical sensors for chemical and biological analysis. *Analytical chemistry*, 84(2):793–821, 2011.

[56] Jason M Gamba. *The role of transport phenomena in whispering gallery mode optical biosensor performance.* PhD thesis, California Institute of Technology, 2012.

[57] A. Armani. *Science*, 334(6062):1496–1496, Dec 2011.

[58] S Arnold, D Keng, SI Shopova, S Holler, W Zurawsky, and F Vollmer. Whispering gallery mode carousel–a photonic mechanism for enhanced nanoparticle detection in biosensing. *Opt. Express*, 17(8):6230–6238, 2009.

[59] Xiaomin Zhang, Hong Seok Choi, and Andrea M Armani. Ultimate quality factor of silica microtoroid resonant cavities. *Applied Physics Letters*, 96(15):153304–153304, 2010.

[60] J. C. Knight, G. Cheung, F. Jacques, and T. A. Birks. Phase-matched excitation of whispering-gallery-mode resonances by a fiber taper. *Optics Letters*, 22(15):1129, Aug 1997.

[61] Ming Cai, Oskar Painter, and Kerry J Vahala. Observation of critical coupling in a fiber taper to a silica-microsphere whispering-gallery mode system. *Physical Review Letters*, 85(1):74–77, 2000.

[62] S. Spillane, T. Kippenberg, O. Painter, and K. Vahala. Ideality in a Fiber-Taper-Coupled Microresonator System for Application to Cavity Quantum Electrodynamics. *Physical Review Letters*, 91(4), Jul 2003.

[63] Roland Wiesendanger. *Scanning Probe Microscopy and Spectroscopy.* Cambridge University Press (CUP), 1994.

[64] Jon D. Swaim, Joachim Knittel, and Warwick P. Bowen. Detection of nanoparticles with a frequency locked whispering gallery mode microresonator. *Applied Physics Letters*, 102(18):183106, 2013.

[65] Karl Johan Aström and Richard M Murray. *Feedback systems: an introduction for scientists and engineers.* Princeton University Press, 2010.

[66] Eugene Hecht and Alfred Zajac. *Optics*, volume 4. Addison Wesley San Francisco, CA, 2002.

[67] Elizabeth Wilcut Connolly. *Experiments with toroidal microresonators in cavity QED.* PhD thesis, California Institute of Technology, 2009.

[68] Leonid I Rudin, Stanley Osher, and Emad Fatemi. Nonlinear total variation based noise removal algorithms. *Physica D: Nonlinear Phenomena*, 60(1):259–268, 1992.

[69] *Sparse Bayesian step-filtering for high-throughput analysis of molecular machine dynamics*, 2010.

[70] Edwin Hewitt and Robert E Hewitt. The Gibbs-Wilbraham phenomenon: an episode in Fourier analysis. *Archive for history of Exact Sciences*, 21(2):129–160, 1979.

[71] Jacob W J. Kerssemakers, E Laura Munteanu, Liedewij Laan, Tim L. Noetzel, Marcel E. Janson, and Marileen Dogterom. Assembly dynamics of microtubules at molecular resolution. *Nature*, 442(7103):709–712, Aug 2006.

[72] Brian C Carter, Michael Vershinin, and Steven P Gross. A comparison of step-detection methods: how well can you do? *Biophysical journal*, 94(1):306–319, 2008.

[73] A McF Mood. Introduction to the Theory of Statistics. 1950.

[74] F Vollmer, S Arnold, and D Keng. Single virus detection from the reactive shift of a whispering-gallery mode. *Proceedings of the National Academy of Sciences*, 105(52):20701–20704, 2008.

[75] Heather K Hunt, Carol Soteropulos, and Andrea M Armani. Bioconjugation strategies for microtoroidal optical resonators. *Sensors*, 10(10):9317–9336, 2010.

[76] Frank Vollmer. *Resonant detection of nano to microscopic objects using whispering gallery modes*. PhD thesis, The Rockefeller University, 2004.

[77] Kai Siegbahn. Electron spectroscopy for atoms, molecules, and condensed matter. *Science (Washington, DC);(United States)*, 217(4555), 1982.

[78] Harvey Lodish, Arnold Berk, S Lawrence Zipursky, Paul Matsudaira, David Baltimore, and James Darnell. Molecular cell biology. *New York*, 2000.

[79] E Van Der Pol, AG Hoekstra, A Sturk, C Otto, TG Van Leeuwen, and R Nieuwland. Optical

and non-optical methods for detection and characterization of microparticles and exosomes. *Journal of Thrombosis and Haemostasis*, 8(12):2596–2607, 2010.

[80] Laura Rodríguez-Lorenzo, Roberto de La Rica, Ramón A Álvarez-Puebla, Luis M Liz-Marzán, and Molly M Stevens. Plasmonic nanosensors with inverse sensitivity by means of enzyme-guided crystal growth. *Nature Materials*, 11(7):604–607, 2012.

[81] Computed by modifying Mark Oxborrow's COMSOL code: http://www.npl.co.uk/science-technology/time-frequency/research/microwave-frequency-standards/2.5-d-simulation-of-axi-symmetric-electromagnetic-structures.

[82] Ian M. White, Niranjan M. Hanumegowda, and Xudong Fan. Subfemtomole detection of small molecules with microsphere sensors. *Optics Letters*, 30(23):3189, 2005.

[83] Stepan Podzimek. *Light Scattering, Size Exclusion Chromatography and Asymmetric Flow Field Flow Fractionation.* Wiley Blackwell (John Wiley & Sons), Feb 2011.

[84] Mayumi Noto, David Keng, Iwao Teraoka, and Stephen Arnold. Detection of protein orientation on the silica microsphere surface using transverse electric/transverse magnetic whispering gallery modes. *Biophysical journal*, 92(12):4466–4472, 2007.

[85] Jiangang Zhu, Sahin Kaya Ozdemir, Yun-Feng Xiao, Lin Li, Lina He, Da-Ren Chen, and Lan Yang. On-chip single nanoparticle detection and sizing by mode splitting in an ultrahigh-Q microresonator. *Nature Photonics*, 4(1):46–49, 2009.

[86] Woosung Kim, Sahin Kaya Ozdemir, Jiangang Zhu, Lina He, and Lan Yang. Demonstration of mode splitting in an optical microcavity in aqueous environment. *Applied Physics Letters*, 97(7):071111–071111, 2010.

Toward optical-mass spectroscopy for label-free single bio-molecule detection in aqueous solution

Single-molecule detection is one of the fundamental challenges of modern biology. Such experiments often use labels that can be expensive, difficult to produce, and for small analytes, might perturb the molecular events being studied. Analyte size plays an important role in determining detectability. Current label-free detection techniques using a bare optical resonator in solution have a lower limit of detection around 12.5 nm (radius). Here we use laser-frequency locking in the context of sensing to improve the signal-to-noise ratio of microtoroid optical resonators to the extent that single nanoparticles 2.5 nm in radius, and 15.5 kDa molecules are detected in aqueous solution, thereby bringing these detectors to the size limits needed for detecting the key macromolecules of the cell. Our results, covering several orders of magnitude of particle radius (100 nm to 2 nm), agree with the 'reactive' model prediction for the frequency shift of the resonator upon particle binding. In addition, we demonstrate that molecular weight may be estimated from the frequency shift through a simple formula, thus providing a basis for an "optical mass spectrometer" in solution. We anticipate that our results will enable many applications, including more sensitive medical diagnostics and fundamental studies of single receptor-ligand and protein-protein interactions in real time.

Highly sensitive biodetection is important for many applications such as high throughput drug discovery studies, as it can dramatically reduce the amount of analyte needed and speed the assays[1,2]. A variety of applications in medical diagnostics (e.g. detecting trace amounts of tumor specific antigens to monitor the re-occurrence of cancer[3]) and public health (e.g. detecting bacteria or viruses[4]) would benefit from improved speed and sensitivity. If the sensitivity can be pushed to the single-molecule level, fundamental studies become more direct and decisive, permitting, for example, studies of molecular conformations[1,2]. Frequency locking feedback control has been used in applications such as in scanning tunneling microscopy to maintain tip-surface separation[5]; however, to the best of our knowledge has not previously been used as a means to sense biological molecules[6]. We apply frequency locking to resonant biodetection and achieve a sensitivity that enables us to detect a wide range of nanoscale objects ranging from nanoparticles with radii from 100 to 2.5 nm to exosomes, ribosomes, and single protein molecules (160 kDa and 15.5 kDa).

Optical resonators such as microtoroids work on the principle of total internal reflection[7]. Light continuously circulates within these (often glass) devices generating an evanescent field that interacts multiple times with analytes that bind to the surface of the resonator[8]. The long photon confinement time (on order of tens of nanoseconds) of the microtoroid makes it an extremely sensitive detector with a theoretical limit of detection down to single molecules[9]. This enables us to obtain the statistics of unitary events as opposed to having to look at an ensemble average[10]. Optical resonators have the further advantage that because their surface can be functionalized, they do not require fluorescent tags[2], thus eliminating artifacts due to bleaching, blinking, and tag interference. Because optical resonators can obtain data in the microsecond time regime continuously over several seconds or more they have the potential to bridge a variety of time and length scales. In addition, optical resonators have a large (~300 μm^2) capture area thus making particle detection events more likely to occur than with nanodevices such as nanowires or nano-electrical-mechanical cantilevers. Currently, due to signal-to-noise limitations, the smallest particle radius a bare optical resonator has been shown to detect is 12.5 nm[11] in aqueous solution, and 10 nm in air[12].

In terms of single-particle biological detection, optical resonators such as microspheres[13] and microtoroids[14,15] have been used to detect individual virus particles (~100 nm) without the use of labels.

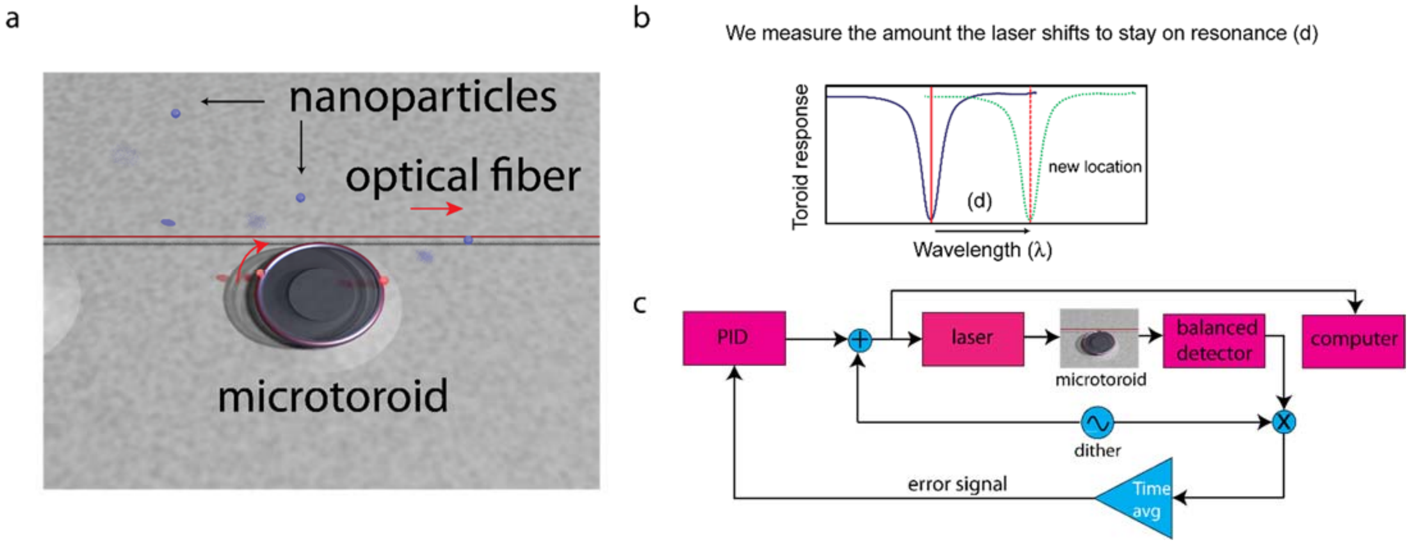

Figure 1 Overview of Frequency Locked Optical Whispering Evanescent Resonator (FLOWER). (a) Rendering of a microtoroid coupled to an optical fiber (not to scale). In our system, a frequency-tuned laser beam is evanescently coupled to a microtoroid (~90 microns in diameter) using an optical fiber (red). At resonance, light (red curved arrow) coming out of the microtoroid destructively interferes with light going straight through the optical fiber (red arrow), causing a dip in the transmission (peak in absorption) vs. light wavelength. **(b)** Conceptual basis for particle detection. The laser frequency (red solid line) is locked to the resonance frequency of the microtoroid (blue line). As particles bind, the resonant frequency of the microtoroid shifts to a new location (green dotted line). We measure the control signal needed to keep the laser locked to the microtoroid's new resonance frequency (red dashed line). **(c)** Block diagram of the sensing control system. A small high-frequency dither is used to modulate the driving laser frequency. When multiplied by the toroid output and time-averaged, this dither signal generates an error signal whose amplitude is proportional to the difference between the current laser frequency and resonant frequency. This error signal is sent to a PID controller whose output is used to set the laser frequency, thus completing the feedback loop. A computer records the observed frequency shifts.

Recently microspheres have been coupled to 70 nm radius gold nanoshells to form a hybrid system capable of detecting single BSA (66 kDa) molecules[16]. The advance described here, Frequency Locked Optical Whispering Evanescent Resonator (FLOWER), (**Fig. 1**) would improve the detection capabilities of optical resonators in general, including hybrid systems.

Both theory (**Supplementary Information**), and finite element electromagnetic computations using COMSOL indicate that for a microtoroid to detect particles of comparable size to single protein molecules (2.5 nm radius, $M \sim 36$ kDa), one must be able to resolve a wavelength shift less than 0.006 fm. This is ~80 times smaller than the approximate wavelength shift seen for detecting particles with a radius of 12.5 nm in an aqueous solution[11]. In order to detect such small wavelength shifts, we use frequency locking (**Figure 1**) in combination with filtering techniques to reduce our noise level to 9.6×10^{-4} fm over one-millisecond intervals (**Supplementary Information**). A step-finding algorithm is used to locate binding events[17].

Our frequency locking approach is an improvement over prior scanning systems that continually sweep back and forth over a large frequency range (3.1×10^{4} fm), only occasionally matching resonance[7]. In contrast, our work directly tracks the resonant wavelength location within a narrow and adaptively varied frequency range with a fixed length of 19 fm. Thus we track discrete fluctuations in signal more accurately and quickly, permitting slight and transient events to be detected. To isolate our signal we computationally filter out known sources of noise such as 60 Hz electronic line noise and apply a median filter to our data.

To characterize our system, we detect polystyrene latex nanoparticles over a range of radii, and 2.5 nm silica nanoparticles at picomolar concentrations

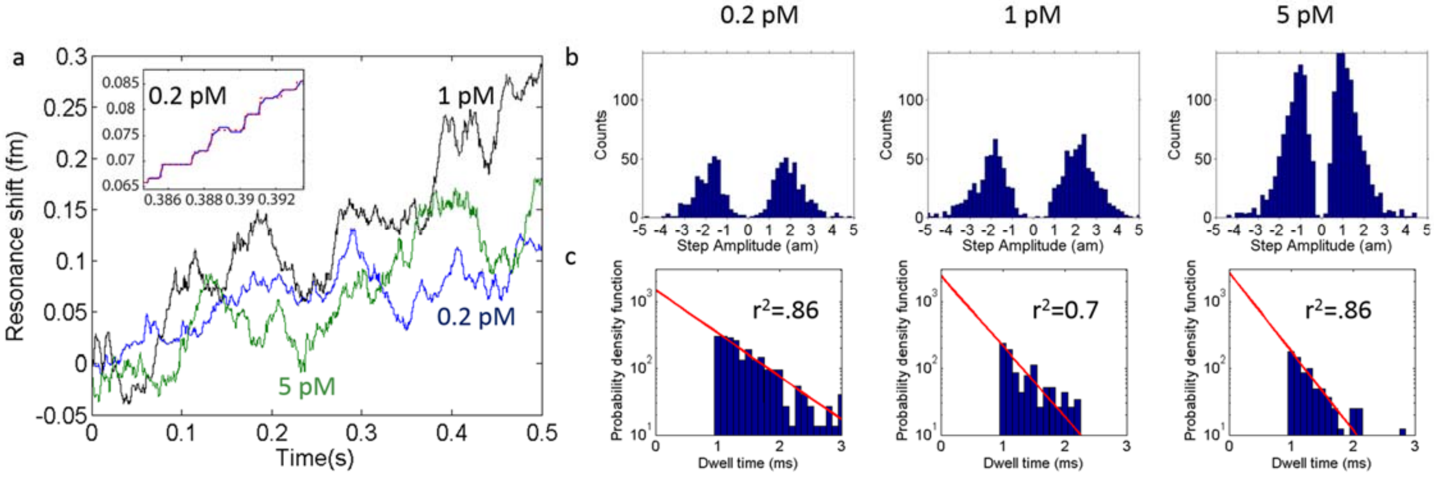

Figure 2 Individual 2.5 nm radius bead detection. (a) Detection of 2.5 nm radius glass nanoparticles at different concentrations (shown in different colors). Step down events represent the unbinding of particles. A zoom-in of the 0.2 pM case (blue) is shown in the inset. The data was filtered using a median filter and steps were fit (red dashed line) using the step-fitting algorithm of Kerssemakers *et al.*[17] **(b)** As expected, the mean step amplitude remains constant because the mean particle size does not change. **(c)** The time in-between binding events (step duration) follows an exponential distribution (red line, fit), indicating that the binding of particles follows a Poisson process. As expected, this exponential distribution shifts to shorter times in a linear fashion with concentration, illustrated here in the log-linear plots as an increase in slope. In the histograms presented, dwell times faster than the digital low pass filter applied to our data (1 ms) were considered unreliable and were not included in the exponential fit. These results are consistent with single particle binding.

(**Fig. 2a**). We perform the detection in water using microtoroids approximately 80–100 μm in diameter, with selected resonant peaks having loaded quality factors (Q) of $\sim 1\times10^5$–5×10^6 in water with an input power of 9.3-100 μW at 633 nm. These moderate Q-factors are chiefly a result of the optical fiber being positioned in direct contact with the microtoroid in the over-coupled regime[18]. This procedure was chosen to minimize noise due to the optical fiber fluctuating against the toroid during the experiment. Furthermore, we perform these experiments under stopped flow conditions where we inject enough sample volume to completely exchange the liquid in our sample chamber three times, before stopping, waiting 30 seconds, and then recording our data. This stopped flow approach mitigates noise from the optical fiber fluctuating against the toroid that occurs when a continuous injection is used[13].

Our results show that after implementing frequency locking, individual detection events appear much more cleanly (a before-and-after example of this result is shown in **Supplementary Fig. 3d**) and that the change in resonant wavelength of the microtoroid upon particle binding is proportional to particle volume (**Fig. 3a**). The theoretical basis for this result is presented in the **Supplementary Information**. **Figure 3b** shows a standard detection result for 10 nm radius nanoparticles. Individual traces of additional nanoparticle detection experiments are shown in **Extended Data Fig. 3**.

To further establish that we detect single 2.5 nm silica particles, we perform the experiment under three different concentrations (0.2, 1, and 5 pM) and record the step amplitude and dwell time (time between steps) distributions. As expected, as the particle concentration increases, the mean step amplitude remains constant, as the mean particle diameter does not change (**Fig. 2b**). Furthermore, the amplitude of the steps we obtain, as shown in **Figure 3**, are in agreement with that predicted by the RSP theory[9] (**Supplementary Information**).

We note that in contrast to the experiments with 10-100 nm nanoparticles that show predominantly up-steps, in the 2.5 nm experiments, more down-steps are observed. This is consistent with other reported particle

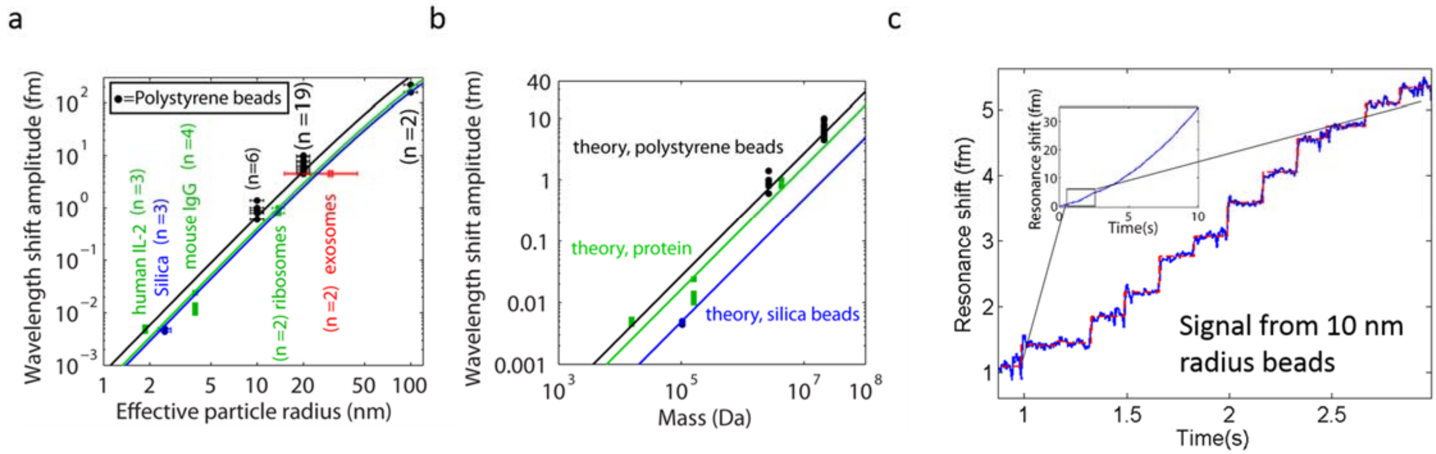

Figure 3 Summary of particle detection data. (a) A wide range of particle sizes with radii from 2-100 nm were detected. For human IL-2 and mouse IgG, an effective particle radius was calculated based on spheres having the same molecular weights as the individual molecules. The solid lines are theoretical predictions based on the reactive sensing principle. Errors bars represent the known polydispersity of our samples. **(b)** Maximum wavelength shift as a function of molecular weight for the same particles as shown in (a). Again, the experimental findings (points) agree well with theoretical predictions for different materials (solid lines). **(c)** The resonance wavelength shift (blue trace) over time of the microtoroid as polystyrene latex nanoparticles 10 nm radius bind to the microtoroid's surface. As a nanoparticle binds, the resonance frequency of the toroid changes. This change appears as a 'step' in the plot of resonance frequency shift over time. The step-fit is shown as a red dashed line. (inset) Zoom-out of the toroid response over the full recording range of 10 seconds. Remaining data sets are shown in Extended Data Figure 4.

detection work using the microtoroid, where, as the particle diameter decreases, particle desorption becomes more frequent[12]. This is expected both from the decreased surface area of interaction and also because optical trapping forces (in this case from the resonator field) decrease with particle size[19].

The dwell times associated with the 2.5 nm detection experiments clearly decrease with increasing concentration. Assuming that the adsorption of particles follows a Poisson process, the dwell times should follow an exponential distribution, which is indeed true. In **Fig. 2c**, we perform exponential fits to the function $\lambda e^{-\lambda t}$, and recover the rate parameter to be 1500, 2400, 2700 steps/second for the 0.2, 1, and 5 pM cases, respectively, demonstrating that our dwell times scale with concentration. These values indicate an offset at 0 pM, suggesting impurities in the background solution. A histogram of step heights for the background solution is shown in **Extended Data Fig. 4.**

As with many nano- or micro-sensors, our dwell times are shorter than would be expected from diffusion alone[20-22]. Recent work by Arnold, *et al.*, have shown that microspherical optical resonators generate optical trapping forces that cause significantly enhanced (100x) nanoparticle transport velocities[22]. We anticipate this effect to be even greater in our frequency-locked system as we are always on resonance as opposed to sweeping past resonance, thus increasing the amount of circulating power our devices experience. In addition, with the configuration of our microtoroid setup and injection using stopped flow conditions, convection plays a significant role in the flow around the toroid. This significantly increases the particle encounter rate, particularly for smaller particle sizes, as shown by a scaling argument (**Supplementary Information**) and is consistent with the binding rates from nanowire experiments which report saturation from the binding of thousands of molecules within seconds at similar concentrations[23].

To demonstrate the use of FLOWER for biological applications, we detected bioparticles ranging in equivalent radii from 25 nm to < 2.5 nm (molecular weight, 15.5 kDa). In particular, we detected exosomes from human mesenchymal stem cells, yeast ribosomes, mouse immunoglobulin G, and human interleukin-2. For the specific detection of particles in complex solutions, as was the case for the experiments involving exosomes and human interleukin-2, antibodies were attached to the toroid's surface using a silane linker (**Supplementary Information**). Experiments involving yeast ribosomes

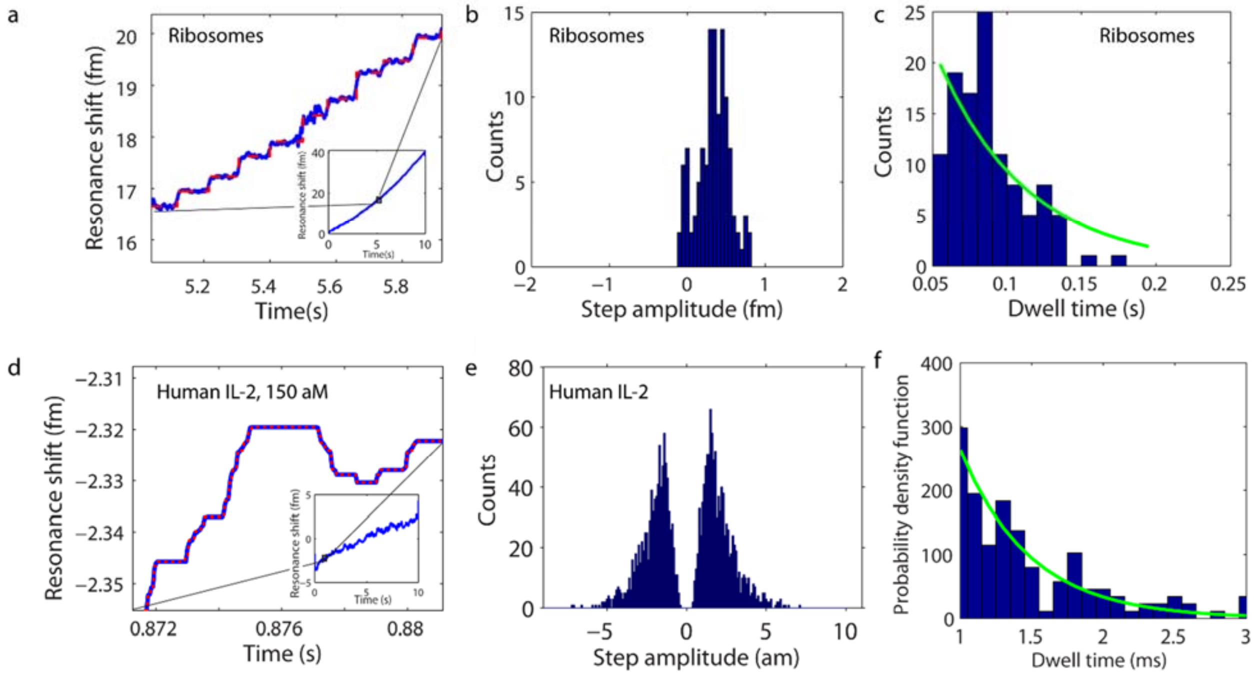

Figure 4 Individual yeast ribosome (12.5 nm radius) and human interleukin-2 (2 nm radius) detection. **(a)** The resonant wavelength shift (blue trace) over time of the microtoroid as ribosomes bind to the microtoroid's surface. The step-fit is shown in red. (inset) Zoom-out of the toroid response over the full recording range of 10 seconds. **(b)** Histogram of step amplitudes. The mean step amplitude of 0.39 fm corresponds to a size of 23 nm as predicted by our nanoparticle detection data thus suggesting that the binding of individual ribosomes is being observed. Negative step amplitudes correspond to unbinding events. **(c)** Histogram of the time in between steps (dwell times). As expected for single-particle binding, the dwell time distribution follows an exponential fit (green). **(d)-(e)** follow the same organization as **(a)-(c)** but with IL-2 as opposed to ribosomes.

and mouse immunoglobulin G, were performed in purified solutions without antibody functionalization of the toroid's surface.

Our results (**Fig. 4** and **Extended Data Figs. 6, 8, and 9**), over a range of sizes, show discrete, step-like, binding events with a step amplitude that corresponds well with the 'reactive' model prediction (**Fig. 4b**), suggesting that we are detecting single particles and not clusters. As with the nanoparticle detection data, the time delay between bioparticle binding events follows an exponential distribution (**Fig. 4c**).

The principal mechanism used to explain the observed signal shifts (e.g., steps shown in **Fig. 2a**) seen with optical resonators upon adsorption of a particle is the 'reactive sensing principle' (RSP)[9]. It applies when the wavelength shift is considerably smaller than the resonance linewidth. The RSP states that the perturbation in a resonator's photonic energy upon particle binding at $\boldsymbol{r}_p$ is equal to the energy required for the toroid's reactive (evanescent) field $E_0(\boldsymbol{r}_p)$ to polarize the particle[9]. On this basis, the shift in resonance wavelength $\Delta\lambda$ is the wavelength λ times the ratio of the particle's polarization energy to the energy in the cavity (Eq.1)[9]:

$$\Delta\lambda = \frac{\alpha_{ex} E_0^2(r_p)}{2\int \varepsilon(r_c) E_0^2(r_c)\,dV}\lambda, \tag{1}$$

where α_{ex} is the particle's polarizability, and ε is the relative permittivity within the cavity mode. Equation 1 makes a clear statement. So long as all of the analyte binds to a region where the mode intensity is the same, the shift will be proportional to the polarizability. The cavity's equator is just such a region, and furthermore it is the region for which the maximum wavelength shift is generated. This maximum wavelength shift appears distinctly in our histograms, and is our basis for estimating both particle size and molecular weight. For a particle binding to the equator with its center at r_e, the wavelength shift $(\Delta\lambda)_{\max}$ is given by

$$(\Delta\lambda)_{\max} = \frac{Da^3\left[E_0^2(r_e)/E^2{}_{\max}\right]}{2\,V_m}\lambda, \tag{2}$$

where in recognition that the polarizability is proportional to the particle volume, we have represented it as Da^3, where a is the particle radius, and D a dielectric factor dependent on the optical properties of both the particle and its aqueous environment. The intensities in the numerator and denominator have been normalized by the maximum intensity in the cavity, which allows the integral in Eq.1 to be expressed as the optical mode volume V_m. Both the intensity ratio in the numerator and V_m are easily obtained from finite element calculations. We use Eq. 2 to provide the theoretical lines plotted in **Fig. 3a.** The slope of the lines through the data and theory are both 3. This relationship between maximum wavelength shift and particle radius has previously been experimentally validated for particle radii ranging from 12.5 - 375 nm[9,11,13,23]. The agreement between theory and experiment in the current work takes bare cavity reactive detection into the single protein realm for the first time.

It is also possible to obtain an equation that predicts a bioparticle's molecular weight M from the observed maximum wavelength shift. Protein folding produces particles having densities which are constant within ~1%. This is evidenced by the constancy of the differential refractive index *dn/dc*. The latter can be used to establish a simple proportionality between molecular weight M and polarizability; $M = (c_p/2)\,\alpha$, where c_p has a value that is constant to within ~1% (**Supplementary Information**). By combining this with Eq. 2 we can estimate a protein's molecular weight from the largest wavelength shift (**Supplementary Information**),

$$M \approx \frac{c_p V_m}{\left[E_0^2(r_e)/E^2{}_{\max}\right]}\frac{(\Delta\lambda)_{\max}}{\lambda}. \tag{3}$$

We note that Eqs. 2 and 3 assume that isotropic molecules bind to the equator. Anisotropic molecules produce shifts that can be sensitive to their orientation relative to the polarization of the whispering gallery mode. In cases where our assumption is not appropriate, an orientation factor is needed[24]. **Fig. 3b** shows good agreement between the known molecular weights of our measured protein and Eq. 3.

In conclusion, we have detected nanoparticles over a large range of sizes and have validated the applicability of our system to bio-detection using exosomes, ribosomes, mouse immunoglobulin G, and human interleukin-2. Our results support the 'reactive' model that suggests that the main contribution of the frequency shift upon particle binding is caused by the energy required for the reactive (evanescent) field to polarize the particle. With theory and experiment in good agreement, FLOWER provides a means for detecting single molecules in solution and identifying their molecular weights, thus paving the way for optically estimating the mass of single molecules in solution, fundamental studies in biophysics, and applications such as high throughput drug discovery and early detection of diseases.

METHODS SUMMARY

Particle detection experiments were performed with a TLB-6300 tunable diode laser (controller number: TLB-6300-LN) from Newport in combination with a DigiLock 110 from Toptica Photonics. Top-of-peak locking was performed using a dither frequency of 2 kHz. The PID controller was set by Ziegler-Nichols tuning rules. The rise time of the system was determined to be 0.5 ms and the settling time 1.5 ms. Signals were detected using a Nirvana auto-balanced receiver (Model 2007) from Newport. Polarization was adjusted using an in-line polarization controller from General Photonics (Product Number: PLC-003-S-90). Data was recorded at 20 kHz using a 24-bit data acquisition card (NI-PCI-4461) from National Instruments. Following data acquisition, Fourier filtering was performed to remove 60 Hz and its harmonics, 100 Hz, and 2 kHz. A median filter of window size 1001 was then applied. Recombinant human interleukin-2 was purchased from Pierce Biotechnology (Product Number: R201520). Mouse IgG was purchased from Jackson ImmunoResearch (Code Number: 015-000-003). Anti-CD81 used for the exosome experiments was purchased from Santa Cruz Biotechnology. Prior to injection, solutions were thermally equilibrated for > 1 hr in a 1 L room-temperature water bath. Solutions were injected using a syringe pump (Harvard Apparatus) and a 1 mL syringe fitted with a 23 gauge luer stub, tubing (ID 0.02 OD 0.06 WALL 0.02, VWR) and a small metal tube (Corp. 23 TW (.025/.0255 OD x .0165/.018 ID, New England Small Tubes). Data was recorded in LabVIEW and filtered in MATLAB.

Acknowledgements We thank Raymond Deshaies for the ribosomes, Carver Mead for the frequency locking suggestion, Richard Murray for discussions on feedback control, Andrew Raubitschek for the exosomes, and Rob Phillips and Kerry Vahala for comments and discussion of the manuscript.

The authors declare no competing financial interests

1 Luchansky, M. S. & Bailey, R. C. High-Q optical sensors for chemical and biological analysis.

Analytical chemistry **84**, 793-821, doi:10.1021/ac2029024 (2012).

2 Vollmer, F. & Arnold, S. Whispering-gallery-mode biosensing: label-free detection down to single molecules. *Nature methods* **5**, 591-596, doi:10.1038/nmeth.1221 (2008).

3 Rodriguez-Lorenzo, L., de la Rica, R., Alvarez-Puebla, R. A., Liz-Marzan, L. M. & Stevens, M. M. Plasmonic nanosensors with inverse sensitivity by means of enzyme-guided crystal growth. *Nature materials* **11**, 604-607, doi:10.1038/nmat3337 (2012).

4 Dantham, V. R., Holler, S., Kolchenko, V., Wan, Z. & Arnold, S. Taking whispering gallery-mode single virus detection and sizing to the limit. *Appl Phys Lett* **101**, doi:Artn 043704 Doi 10.1063/1.4739473 (2012).

5 Wiesendanger, R. *Scanning probe microscopy and spectroscopy : methods and applications*. (Cambridge University Press, 1994).

6 Swaim, J. D., Knittel, J. & Bowen, W. P. Detection of nanoparticles with a frequency locked whispering gallery mode microresonator. *Appl Phys Lett* **102**, -, doi:doi:http://dx.doi.org/10.1063/1.4804243 (2013).

7 Armani, D. K., Kippenberg, T. J., Spillane, S. M. & Vahala, K. J. Ultra-high-Q toroid microcavity on a chip. *Nature* **421**, 925-928, doi:10.1038/nature01371 (2003).

8 Vahala, K. J. Optical microcavities. *Nature* **424**, 839-846, doi:10.1038/nature01939 (2003).

9 Arnold, S., Khoshsima, M., Teraoka, I., Holler, S. & Vollmer, F. Shift of whispering-gallery modes in microspheres by protein adsorption. *Optics letters* **28**, 272-274 (2003).

10 Knight, A. *Single molecule biology*. (Elsevier/Academic, 2009).

11 Lu, T. *et al.* High sensitivity nanoparticle detection using optical microcavities. *Proceedings of the National Academy of Sciences of the United States of America* **108**, 5976-5979, doi:10.1073/pnas.1017962108 (2011).

12 He, L. N., Ozdemir, K., Zhu, J. G., Kim, W. & Yang, L. Detecting single viruses and nanoparticles using whispering gallery microlasers. *Nat Nanotechnol* **6**, 428-432, doi:Doi 10.1038/Nnano.2011.99 (2011).

13 Vollmer, F., Arnold, S. & Keng, D. Single virus detection from the reactive shift of a whispering-gallery mode. *Proceedings of the National Academy of Sciences of the United States of America* **105**, 20701-20704, doi:10.1073/pnas.0808988106 (2008).

14 He, L., Ozdemir, S. K., Zhu, J., Kim, W. & Yang, L. Detecting single viruses and nanoparticles using whispering gallery microlasers. *Nat Nanotechnol* **6**, 428-432, doi:10.1038/nnano.2011.99 (2011).

15 Zhu, J., Ozdemir, S. K., He, L., Chen, D. R. & Yang, L. Single virus and nanoparticle size spectrometry by whispering-gallery-mode microcavities. *Optics express* **19**, 16195-16206, doi:10.1364/OE.19.016195 (2011).

16 Dantham, V. R. *et al.* Label-Free Detection of Single Protein Using a Nanoplasmonic-Photonic Hybrid Microcavity. *Nano letters*, doi:10.1021/nl401633y (2013).

17 Kerssemakers, J. W. *et al.* Assembly dynamics of microtubules at molecular resolution. *Nature* **442**, 709-712, doi:10.1038/nature04928 (2006).

18 Gamba, J. M., Flagan, R. C., Flagan, R. C. & California Institute of Technology. Division of Chemistry and Chemical Engineering. in *CIT theses 2012* 1 online resource (xxiii, 139 leaves) ill. (California Institute of Technology,, Pasadena, Calif., 2012).

19 Ashkin, A., Dziedzic, J. M., Bjorkholm, J. E. & Chu, S. Observation of a single-beam gradient force optical trap for dielectric particles. *Optics letters* **11**, 288 (1986).

20 Squires, T. M., Messinger, R. J. & Manalis, S. R. Making it stick: convection, reaction and diffusion in surface-based biosensors. *Nature biotechnology* **26**, 417-426, doi:10.1038/nbt1388 (2008).

21 Gamba, J. M. & Flagan, R. C. Flow-enhanced transient response in whispering gallery mode biosensors. *Appl Phys Lett* **99**, doi:Artn 253705
Doi 10.1063/1.3669698 (2011).

22 Arnold, S. *et al.* Whispering Gallery Mode Carousel--a photonic mechanism for enhanced nanoparticle detection in biosensing. *Optics express* **17**, 6230-6238 (2009).

23 Stern, E. *et al.* Label-free immunodetection with CMOS-compatible semiconducting nanowires. *Nature* **445**, 519-522, doi:10.1038/nature05498 (2007).

24 Noto, M., Keng, D., Teraoka, I. & Arnold, S. Detection of protein orientation on the silica microsphere surface using transverse

electric/transverse magnetic whispering gallery modes. *Biophysical journal* **92**, 4466-4472, doi:10.1529/biophysj.106.103200 (2007).

SUPPLEMENTARY INFORMATION

Supplementary text

Theory

Our experimental results yield a frequency shift upon protein binding that is not dependent on the circulating power over the range used in our experiments. This excludes the importance of a nonlinear mechanism. In addition, the shifts being measured here are much smaller than the linewidth (~1 part in 10^5), which essentially eliminates the coupling between clockwise and counter clockwise modes. Fiber coupling only stimulates one of these circulating modes so a single protein-binding event corresponds to the interaction between a polarizable protein and a traveling wave resonator. **Theory for this circumstance was proposed in the past [1] but has not been tested at the single protein level because the experimental signals in the past have been masked by noise**. The current frequency locking technique overcomes past experimental limitations. In Ref. [1] the theory proposed that the shift in the photonic energy within the cavity is equivalent to the energy required for the reactive field to polarize the protein (Reactive Sensing Principle, RSP). It was computed as a first order perturbation, in which the field on the resonator surface is not modified by the binding event. On this basis the fractional frequency shift is the ratio of the energy required for the reactive field to polarize a protein, divided by the photonic energy in the cavity. Expressed in terms of the shift in the free space wavelength of a laser locked to resonance, this becomes:

$$\Delta\lambda = \frac{\alpha_{ex} E_0^2(r_p)}{2\int \varepsilon_r(r_c) E_0^2(r_c) dV}\lambda, \tag{1}$$

where ε_r is the relative permittivity of the cavity, and α_{ex} is the excess polarizability (with units of volume). For a spherical nanoparticle or protein α_{ex} is expressed as a dielectric factor D times the cube of an equivalent radius, $\alpha_{ex} = Da^3$. For a microspherical resonator Eq. 1 can be evaluated analytically, however for a toroid it is more convenient to recast the equation in terms of parameters that can be calculated numerically [2]. This involves dividing the numerator and denominator by the maximum intensity in the cavity, $E_{\max}^2$. In this intensity normalized form the integral in the denominator is termed the optical mode volume, V_m. The most unique shift is for binding events at the equator (with the center of the protein at r_e from the center of the torus), where the shift for the lowest order mode is greatest. Eq.1 becomes:

$$(\Delta\lambda)_{\max} = \frac{Da^3\left[E_0^2(r_e)/E^2{}_{\max}\right]}{2V_m}\lambda. \tag{2}$$

The particle's center is at r_e from the center of the torus, where $E_0^2(r_e)/E_{\max}^2 = 0.22\exp(-a/L)$, with $\mathrm{L} \simeq 120\mu\mathrm{m}$. For the spherical nanoparticles the dielectric factor $D = 4\pi n_m^2(n_p^2 - n_m^2)/(n_p^2 + 2n_m^2)$, where n_m and n_p are the refractive indices of the medium (water) and nanoparticle, respectively. Each nanoparticle material in aqueous solution gives a different D ($D_{polystyrene} = 3.70$, $D_{protein} = 2.17$, $D_{SiO2} = 1.85$), which explains the three lines in Fig. 3a in the main text. Agreement between theory and experiments in Fig.3a, clearly validates the reactive mechanism. Next is the question of whether this mechanism can enable an estimate of molecular weight in solution.

Polarizability can be related to particle mass. This is especially the case for protein as evidenced from refractive index measurements in solution as concentration *c* is varied. As protein is dispersed into solution the refractive index of the solution increases. The change in the refractive index dn for a slight increase in concentration dc determines the differential refractive index dn/dc. For protein dn/dc = 0.185 cm^3/g, and varies by only about ~1%. By treating the protein as a polarizable object, the polarizability can be shown to be directly proportional to the molecular weight of the protein *M*,

$$M = \frac{N_A \alpha_{ex}}{2n\varepsilon_0 \dfrac{dn}{dc}}, \tag{3}$$

where N_A is Avogadro's number, and *n* is the refractive index of water. By solving Eq.2 for polarizability (α_{ex} = Da^3), and substituting the result in Eq.3, the molecular weight:

$$M \approx \frac{c_p V_m}{\left[E_0^2(r_e)/E^2{}_{\max}\right]} \frac{(\Delta\lambda)_{\max}}{\lambda} \tag{4}$$

For silica and polystyrene we use dn/dc values of 0.05 [3] and 0.256 cm^3/g [4] respectively. We note that Eqns. 2 & 4 assume that isotropic particles bind to the equator. Anisotropic molecules produce shifts that are sensitive to their orientation relative to the polarization of the WGM. In cases where our assumption is not appropriate, an orientation factor is needed [5]. Fig. 3b shows good agreement between the known molecular weights of our measured protein and Eq. 4, which provides further proof that we are detecting single protein molecules.

References

1. Arnold, S., Khoshsima, M., Teraoka, I., Holler, S. & Vollmer, F. Shift of whispering-gallery modes in microspheres by protein adsorption. *Optics Letters* **28**, 272-274 (2003).
2. Computed by modifying Mark Oxborrow's COMSOL code. http://www.npl.co.uk/science-technology/time-frequency/research/microwave-frequency-standards/2.5-d-simulation-of-axi-symmetric-electromagnetic-structures
3. White, I.M., Hanumegowda, N.M., Fan, X. Subfemtomole detection of small molecules with microsphere sensors, *Optics Letters*, **30**, 3189-3191 (2005).
4. Podzimek, S., Light Scattering, Size Exclusion Chromatography and Asymmetric Flow Field Fractionation: Powerful Tools for the Characterization of Polymers, Proteins and Nanoparticles, p. 70 (2011).
5. Noto, M., Keng, D., Teraoka, I. & Arnold, S. Detection of protein orientation on the silica microsphere surface using transverse electric/transverse magnetic whispering gallery modes. *Biophysical Journal* **92**, 4466-4472, doi:10.1529/biophysj.106.103200 (2007).

Time in between binding events is faster than from diffusion alone

The arrival rate of particles to the vicinity of the toroid = $C\hat{Q}$, where C is the concentration (number of particles/volume), and $\hat{Q}$ is the injection flow rate (volume/time). Given a concentration of 150 aM and an injection rate of 1 mL/min, this gives an arrival rate of 1500 particles/second. The velocity, V, from injection is given by, $V = \frac{\hat{Q}}{A}$, where A is the cross-sectional area of the inlet tube. V is therefore 550 mm/s. From here we calculate a Reynolds number of 550, meaning convection is 550 times bigger than viscous diffusion of the liquid molecules. The frequency, f, of vortex shedding over the toroid is given by $f = V/h$, where h=0.1 mm (**Extended Data Figure 2**), therefore an encounter rate of 10^3 to 10^4 Hz seems feasible. As smaller particles tend to be influenced by smaller vortices more, vortices shed from the ~500 nm diameter optical fiber may play a role, making the encounter rate even higher. Because our experiments occur under stopped flow conditions, we estimate how long it takes for this kinetic energy to dissipate. The kinetic energy input inside the chamber is given by $\frac{1}{2}\rho V^2 A_2 H$, where A_2 is the area of top of the chamber. The rate of energy dissipation is given by $\sim \mu \left(\frac{V}{l}\right)^2 l^3 \sim \mu V^2 l$, where μ is the dynamic viscosity and l is a characteristic length chosen to be the height of the sample chamber, H, 0.1 cm. The time, t, it takes for the kinetic energy of the injection to dissipate is therefore: $\frac{A_2}{\nu}$, $t \sim$ 100 seconds. Thus the injection rate calculated for the initial injection velocity is expected to hold valid for the duration of the experiment.

Noise determination

In our experiments, we establish our noise level by measuring how the resonance wavelength of the microtoroid changes over time when it is immersed in a buffer (background) solution. The reason we calculate our noise level in this manner is because our particle detection experiments are performed in buffer solutions, so measuring how the resonance wavelength of the microtoroid changes in just a buffer solution represents our control case of what the resonance shift looks like when there are no particles.

We calculate our noise levels before and after feedback control by calculating the standard deviation of the resonance wavelength value after subtracting a general trend (see below). Before feedback control, the standard deviation of the resonance wavelength value over 60 seconds is ~1 pm (**Extended Data Fig. 1a**). After enabling feedback control, the fluctuations are significantly decreased to ~0.07 fm over 10 seconds (**Extended Data Fig. 1b**). The shorter time interval over which we average our signal in the frequency locking case reflects the higher data acquisition rate that is enabled with feedback control.

If we calculate the noise level (standard deviation) over 1 ms intervals which is the approximate time between binding events for our 5 nm nanoparticle experiments, this number reduces further to $\sim 9.6 \times 10^{-4}$ fm. This represents an average over 20 data points for 10,000 intervals. We note that the noise level decreases when averaging over smaller time intervals as our noise is not white noise. Before these numbers are calculated, we first computationally filter the data to remove known sources of noise and then apply a median filter of window size 1001.

A general trend was subtracted from the buffer data before computing noise levels to account for thermal drift of the system. Due to the large circulating intensities within optical resonators, there is a significant, but slow (on the order of seconds), thermal drift of the resonance frequency over time. This is due to index of refraction changes due to temperature changes which have been established to be ~1 pm/1°C in silica. Thermal drift may also occur due to temperature fluctuations in the room and is considered to be one of the main sources of environmental noise for optical resonators. We expect thermal drift as we are not working in a temperature controlled environment and it is reasonable to expect temperature changes of 1–2 degrees. A downward drift indicates cooling whereas an upwards drift indicates heating of the microtoroid. We note that this long term overall drift is large (> fm) compared to the wavelength shift we expect to see from a single molecule which is 0.005 fm. In addition, we also note that the time scale of the long term shift due to temperature is on the order of seconds while the time scale of a single molecule binding event is on the order of milliseconds, and therefore, this thermal drift does not hamper our ability to detect individual binding events.

Linker Synthesis

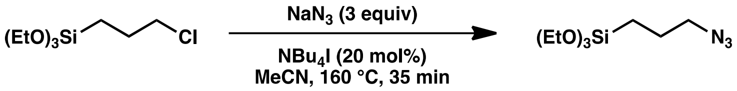

3-azidopropyltriethoxysilane. Two flame-dried, 20 mL microwave vials were each charged with 3-chloropropyltriethoxysilane (1.0 mL, 4 mmol, 1 equiv), sodium azide (813.8 mg, 12 mmol, 3 equiv), tetrabutylammonium iodide (310.6 mg, 0.84 mmol, 0.2 equiv) and dry acetonitrile (20 mL). The vials were sequentially heated in a Biotage Initiator microwave (160 °C) for 35 minutes. The reaction mixtures were combined and the solvent was removed in vacuo. To the residue was added pentane, and the mixture was filtered through Celite then concentrated in vacuo. The crude product (1.5439 g, 75% yield) appeared clean by NMR, but could be further purified by Kugelrohr distillation (0.1–0.3 torr, 88 °C bath temperature) to afford a colorless oil: ^{1}H NMR (300 MHz, CDCl$_3$) δ 3.82 (q, *J* = 7.0 Hz, 4H), 3.27 (t, *J* = 7.0 Hz, 2H), 1.79 – 1.64 (m, 2H), 1.23 (t, *J* = 7.0 Hz, 9H), 0.75 – 0.60 (m, 2H).

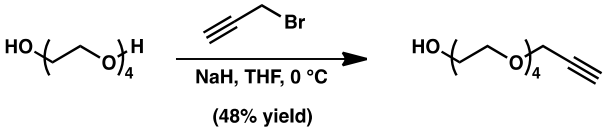

HO–TEG–Alkyne. A flame-dried 1 L round-bottom flask, equipped with a magnetic stir-bar was charged with sodium hydride (1.5070 g, 60% in mineral oil, 37 mmol, 1.2 equiv) then sealed with a rubber septum under nitrogen. To the flask was added THF (ca. 400 mL) via cannula, then the reaction mixture was cooled in an ice-water bath. Tetraethyleneglycol (8.0 mL, 46 mmol, 1.5 equiv) was added dropwise to afford a homogeneous mixture. To the stirring mixture was added propargyl bromide (3.4 mL, 80 wt% in toluene, 31 mmol, 1 equiv) dropwise, and the resulting solution was stirred until complete consumption of the bromide was observed by thin layer chromatography (2.5 hours). The reaction was quenched by addition of saturated ammonium chloride and water and the bulk of the THF was removed by rotary evaporation. The resulting mixture was extracted with dichloromethane (75 mL x 4) and the combined organic fractions were dried over anhydrous magnesium sulfate, clarified with activated charcoal, filtered and concentrated in vacuo. The residue was purified by flash chromatography (20:1 DCM:MeOH) to afford the desired propargyl ether (3.5388 g, 48% yield): ^{1}H NMR (300 MHz, CDCl$_3$) δ 4.20 (d, *J* = 2.4 Hz, 2H), 3.75 – 3.63 (m, 14H), 3.63 – 3.58 (m, 2H), 2.65 (t, *J* = 6.0 Hz, 1H), 2.42 (t, *J* = 2.4 Hz, 1H).

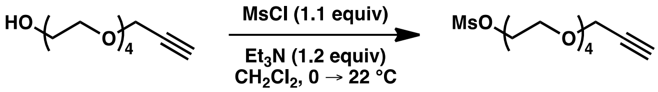

MsO–TEG–Alkyne. A flame-dried round-bottom flask was equipped with a magnetic stir-bar and charged with HO–TEG–Alkyne (3.4418 g, 14.8 mmol, 1 equiv). The flask was sealed with a rubber septum under nitrogen. To the flask was added dichloromethane (75 mL) and freshly distilled triethylamine (2.48 mL, 17.8 mmol, 1.2 equiv). The flask was then cooled in an ice-water bath, and mesyl chloride (1.26 mL, 16.3 mmol, 1.1 equiv) was added dropwise to the stirring mixture. Consumption of the starting material was observed by thin layer chromatography after 15 minutes, and saturated aqueous ammonium chloride was added then the phases were separated. The aqueous layer was extracted with additional dichloromethane (100 mL x3), then the combined organic layers were dried over magnesium sulfate, filtered, and concentrated in vacuo. The residue was purified by flash chromatography (40:1 DCM:MeOH) to afford the desired mesylate in a quantitative yield: ^{1}H NMR (300 MHz, Chloroform-*d*) δ 4.43 – 4.33 (m, 2H), 4.20 (d, *J* = 2.4 Hz, 2H), 3.81 – 3.73 (m, 2H), 3.73 – 3.60 (m, 12H), 3.08 (s, 3H), 2.43 (t, *J* = 2.4 Hz, 1H).

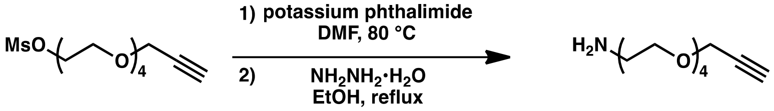

H$_2$N–TEG–Alkyne. A flame-dried 50 mL round-bottom flask was charged with MsO–TEG–Alkyne (1.0082 g, 3.2 mmol, 1 equiv) and sealed with a rubber septum under nitrogen. Dry DMF (13.5 mL) was added by syringe, followed by rapid addition of potassium phthalimide (720.8 mg, 3.9 mmol, 1.2 equiv). The thick slurry was heated in an 80 °C oil bath with good stirring. After 3 hours, additional potassium phthalimide (380 mg, 2.0 mmol) was added to the mixture, and heating was continued overnight. The reaction mixture was partitioned between dichloromethane and water and the phases were separated. The aqueous layer was extracted exhaustively with dichloromethane (until no product remained in the aqueous layer). The combined organics were dried over magnesium sulfate, filtered and concentrated in vacuo. The residue was purified by flash chromatography (40:1 DCM:MeOH) to afford a white crystalline solid that was carried forward in its entirety to the next stage. A round-bottom flask was charged with the phthalimide product from the previous stage, hydrazine hydrate (473 µL, 9.74 mmol, 3 equiv), and absolute ethanol (32 mL). The flask was equipped with a stir bar and a reflux condenser. The mixture was heated to reflux with stirring for an hour, at which point complete consumption of the starting material was observed by thin layer chromatography. The reaction mixture was filtered to remove the white precipitate formed in the reaction and the filtrate was concentrated in vacuo. The residue was dry-loaded onto silica gel and purified by column chromatography (40:1 DCM:MeOH → 15:1:0.05 DCM:MeOH:$NH_4OH_{(aq)}$ → 10:1:0.05 DCM:MeOH:$NH_4OH_{(aq)}$) to afford the primary amine (616.0 mg, 82% yield over two steps) as a yellowish oil: ^{1}H NMR (300 MHz, $CDCl_3$) δ 4.23 – 4.12 (m, 2H), 3.75 – 3.56 (m, 14H), 3.55 – 3.44 (m, 2H), 2.91 – 2.79 (m, 2H), 2.46 – 2.39 (m, 1H), 1.84 (s, 2H).

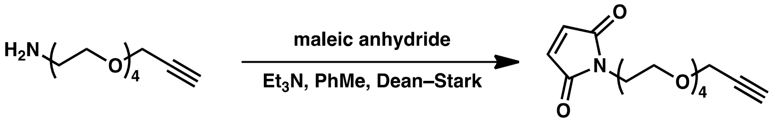

MAL–TEG–Alkyne. A round-bottom flask was charged with H$_2$N–TEG–Alkyne (231 mg, 1 mmol, 1 equiv), maleic anhydride (107.7 mg, 6.5 mmol, 1.1 equiv), triethylamine (14 µL, 0.1 mmol, 0.1 equiv), and toluene (30 mL). The flask was fitted with a Dean–Stark trap and a reflux condenser, then heated to vigorous reflux for 36 h. The reaction mixture was concentrated in vacuo and dissolved in dichloromethane (60 mL). This solution was washed with aqueous hydrochloric acid (0.1 N) then brine. The organic layer was dried over anhydrous magnesium sulfate, filtered, and concentrated in vacuo. The residue was purified by column chromatography (40:1 DCM:MeOH) to afford the maleimide (42.0 mg, 14% yield): ^{1}H NMR (300 MHz, $CDCl_3$) δ 6.70 (s, 2H), 4.20 (d, *J* = 2.4 Hz, 2H), 3.76 – 3.58 (m, 16H), 2.43 (t, *J* = 2.4 Hz, 1H), 1.62 (s, 2H).

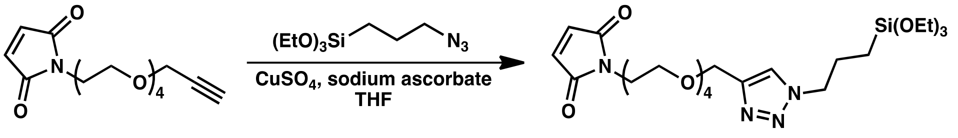

MAL–TEG–Si. A 4 mL vial was charged with MAL–TEG–Alkyne (35.0 mg, 0.11 mmol, 1 equiv) and THF (1 mL). To the solution was added 3-azidopropyltriethoxysilane (27.8 mg, 0.11 mmol. 1 equiv) and sodium ascorbate (13.4 mg, 0.068 mmol, 0.5 equiv). Finally, copper (II) sulfate (11 μL, 1M in H_2O, 0.011 mmol, 0.1 equiv) was added and a brown precipitate was immediately observed. After 30 minutes, additional copper (II) sulfate (22 μL) was added, and the suspension was stirred overnight. The reaction mixture was partitioned between dichloromethane and brine, and the phases were separated. The aqueous phase was further extracted with dichloromethane (15 mL x 3). The combined organics were dried over magnesium sulfate, filtered and concentrated in vacuo. The residue was purified by flash chromatography (20:1 DCM:MeOH) to afford the desired triazole (39.4 mg, 63% yield): ^{1}H NMR (300 MHz, $CDCl_3$) δ 7.56 (s, 1H), 6.67 (s, 2H), 4.65 (s, 2H), 4.31 (t, *J* = 7.2 Hz, 2H), 3.78 (q, *J* = 7.0 Hz, 6H), 3.71 – 3.51 (m, 16H), 2.07 – 1.91 (m, 2H), 1.18 (t, *J* = 7.0 Hz, 9H), 0.64 – 0.50 (m, 2H).

Extended Data

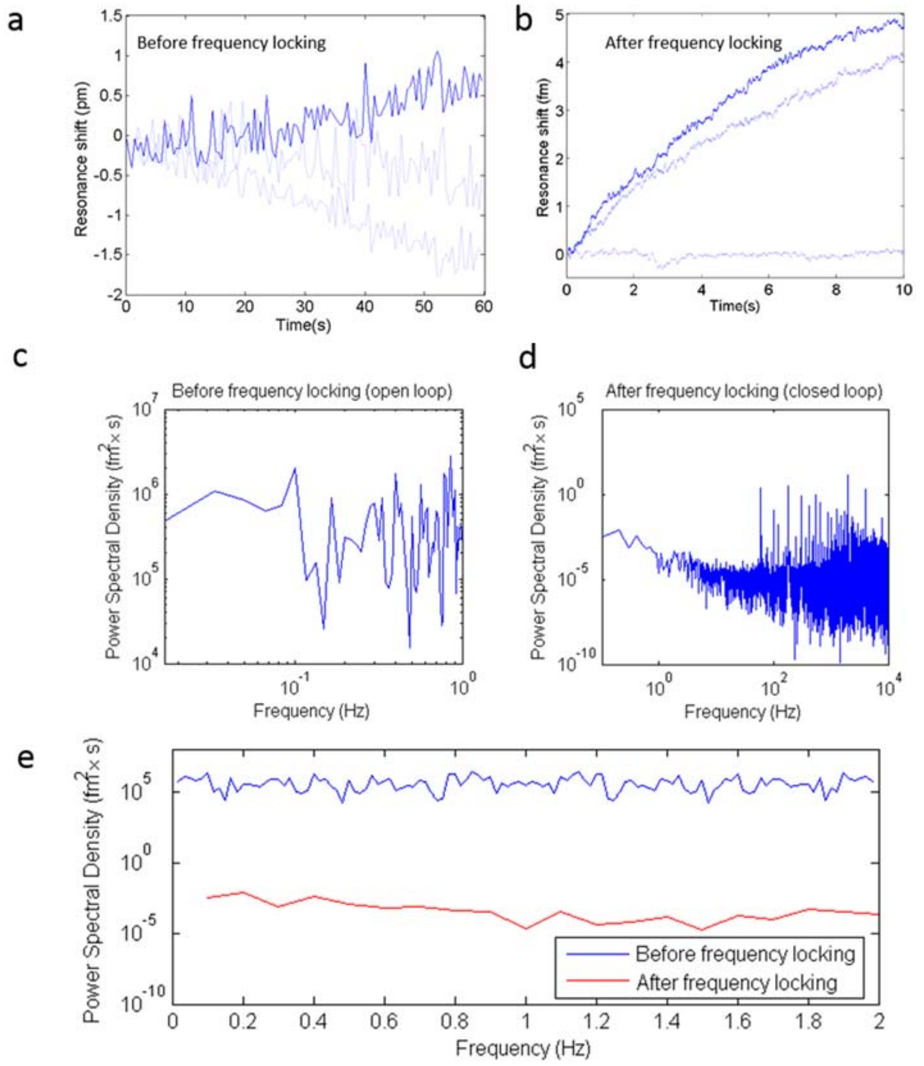

Extended Data Figure 1 | The addition of frequency locking feedback control reduces the noise level to 9.6 x 10^{-4} fm over one-millisecond intervals (a) Toroid response to a buffer (no suspended particles) solution before the implementation of frequency locking. The blue curves (n = 3) show how the resonance wavelength of the toroid changes over time when immersed in a buffer solution. The microtoroid response shows large (~1 pm) fluctuations and an overall drift due to slight temperature changes which alter the microtoroid's index of refraction (dn/dT ~ 1°C/pm in silica, where n is the index of refraction). The noise level (the root-mean-squared value) of the blue curve fluctuations is ~ 1 pm. Before computing the noise level, we computationally remove the large thermal drift from the data by subtracting an exponential fit (not shown) **(b)** Toroid response to a buffer solution after the implementation of frequency locking. The noise level of the blue traces is 9.6 x 10^{-4} fm over one-millisecond intervals and is much smaller than the noise level calculated from (a) before the addition of frequency locking feedback control. We sample over a shorter time period in (b) (10 seconds vs. 60) as frequency locking allows us to sample with a much greater frequency (20 kHz vs 100 Hz). **(c)** The power spectrum of a typical buffer data set before the addition of feedback control. The magnitude of the y-axis provides a measure of the noise level of our system which is the limiting factor in our sensitivity. **(d)** The power spectrum of a typical buffer data set after the addition of feedback control. The tallest peaks correspond to known noise sources and their multiples. The mean noise level (10^{-4} fm^{2}s) is significantly less than the mean noise level (10^5 fm^{2}s) seen in **(c)**. **(e)** The power spectrum in **(b)** and **(c)** plotted on the same axes. The difference in mean noise levels is clearly apparent, indicating the role of the feedback controller in quenching various noise mechanisms.

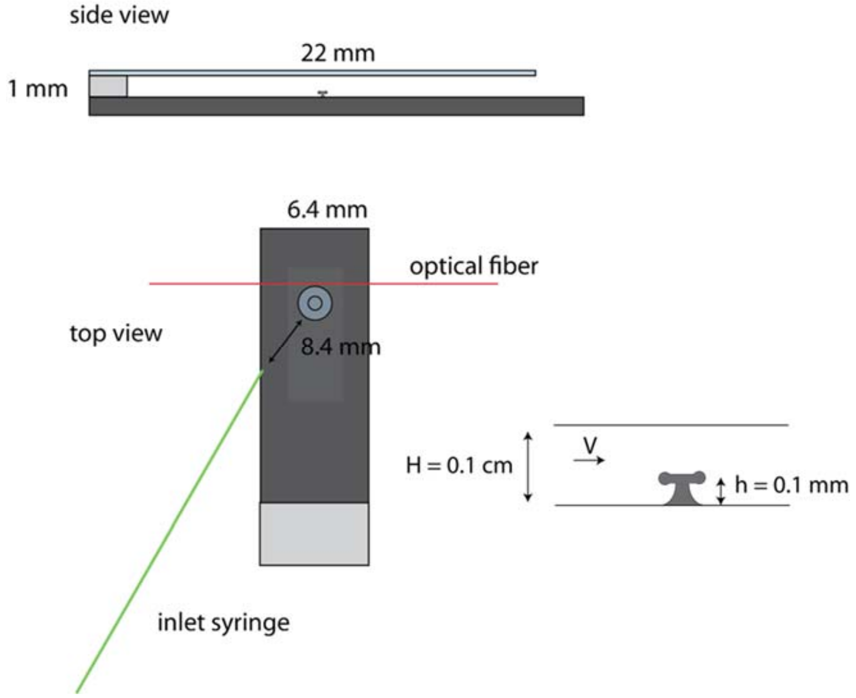

Extended Data Figure 2| Experimental schematic of microtoroid sample chamber with dimensions. The microtoroid is mounted on a steel base and a glass coverslip is placed on top. A portion of a microscope slide is used a spacer. The sample chamber is left open to allow for the optical fiber to pass through. *V* is the injection velocity, *h* is the height of the microtoroid and *H* is the height of the sample chamber.

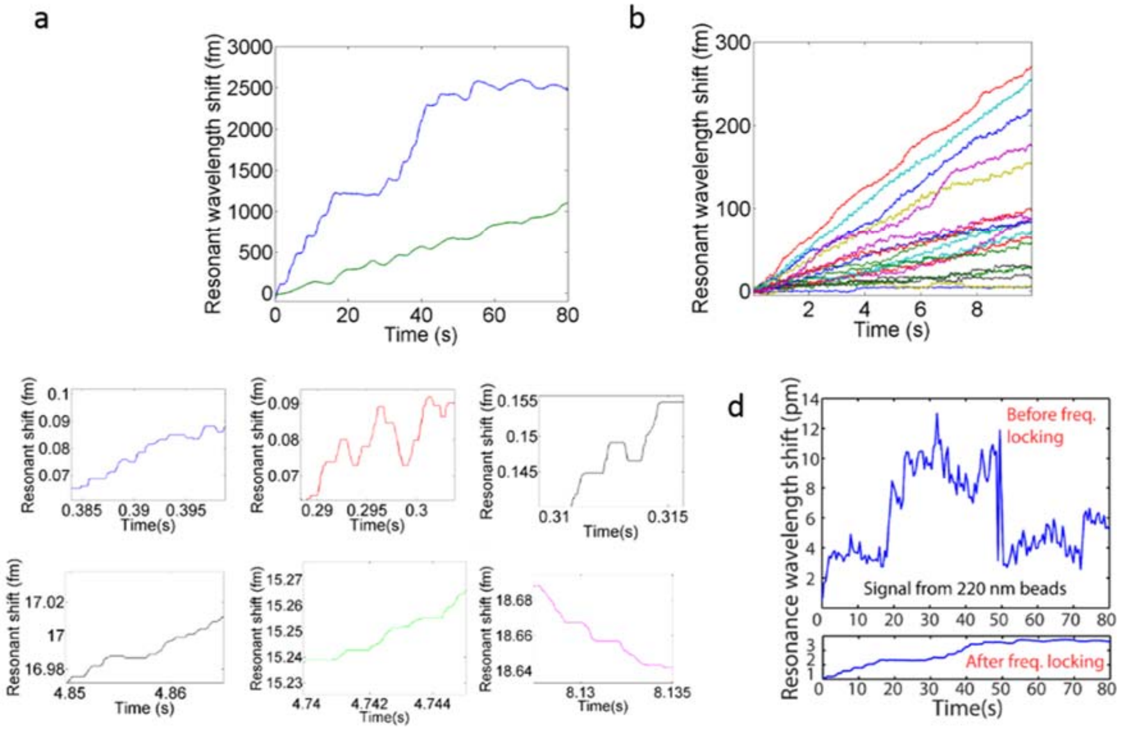

Extended Data Figure 3| Nanoparticle detection data for 5, 40, and 200 nm diameter nanoparticles. Additional 20 nm nanoparticle data is shown in **Extended Data Figure 5**. **(a)** Zoom-in of resonant wavelength shift over time of the microtoroid as 200 nm polystyrene latex nanoparticles bind to the microtoroid's surface. Each trace represents an experiment performed on a different toroid. **(b)** Zoom-in of resonant wavelength shift over time of the microtoroid as 40 nm polystyrene latex nanoparticles bind to the microtoroid's surface. The data presented here is of repeated injections on the same toroid. Two data points represent a repeated injection on a second toroid **(c)** Zoom-in of resonant wavelength shift over time of the microtoroid as 5 nm glass nanoparticles bind to the microtoroid's surface. This represents data from two different toroids. **(d)** (top) Signal from a 220 nm nanoparticle solution without frequency locking has a noise level higher than signal. The apparent steps in this trace are too large to be single 220 nm nanoparticle, and are likely experimental or electronic noise (bottom) 200 nm nanoparticle detection experiment performed using frequency locking. The noise is essentially invisible when plotted on the same axis scale.

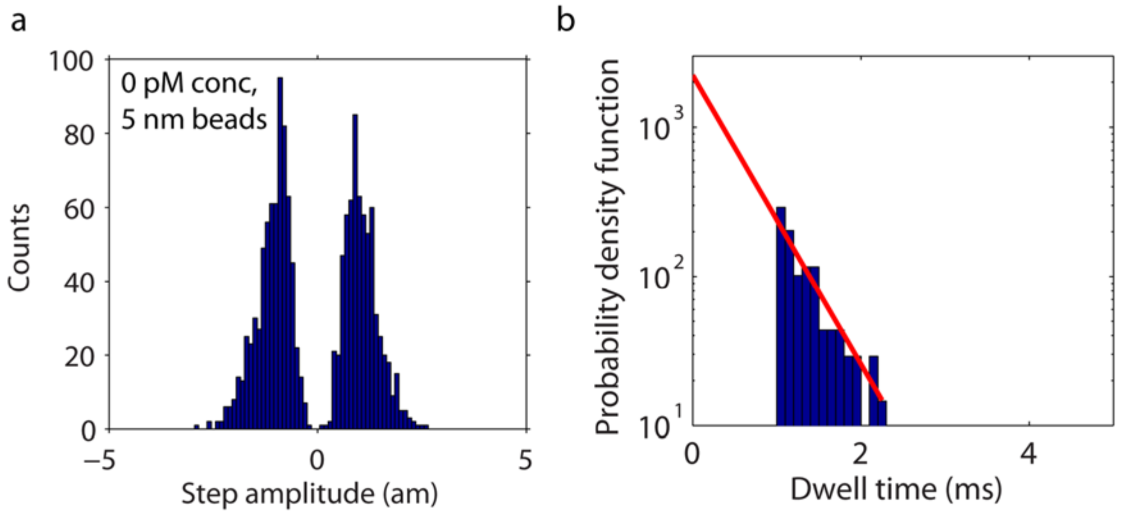

Extended Data Figure 4| Distribution of step heights for 0 pM conc, 5 nm silica beads (a) Step amplitude histogram for 0 pM conc, 5 nm nanoparticles. The maximum step amplitude is 2.6 am which is significantly smaller than the maximum step amplitude found for the solutions with non-zero concentration (Main text, Figure 2). The presence of steps is likely due to a combination of small molecule impurities in the buffer as well as noise related artifacts. We note that more steps appear in the buffer data due to the fact that the step-finding algorithm preferentially searches for larger steps. **(b)** Probability density function for step duration of events found in (a). We only show durations longer than 1 ms as shorter events are unreliable due to our filtering procedures. The rate parameter λ=2230 steps/second.

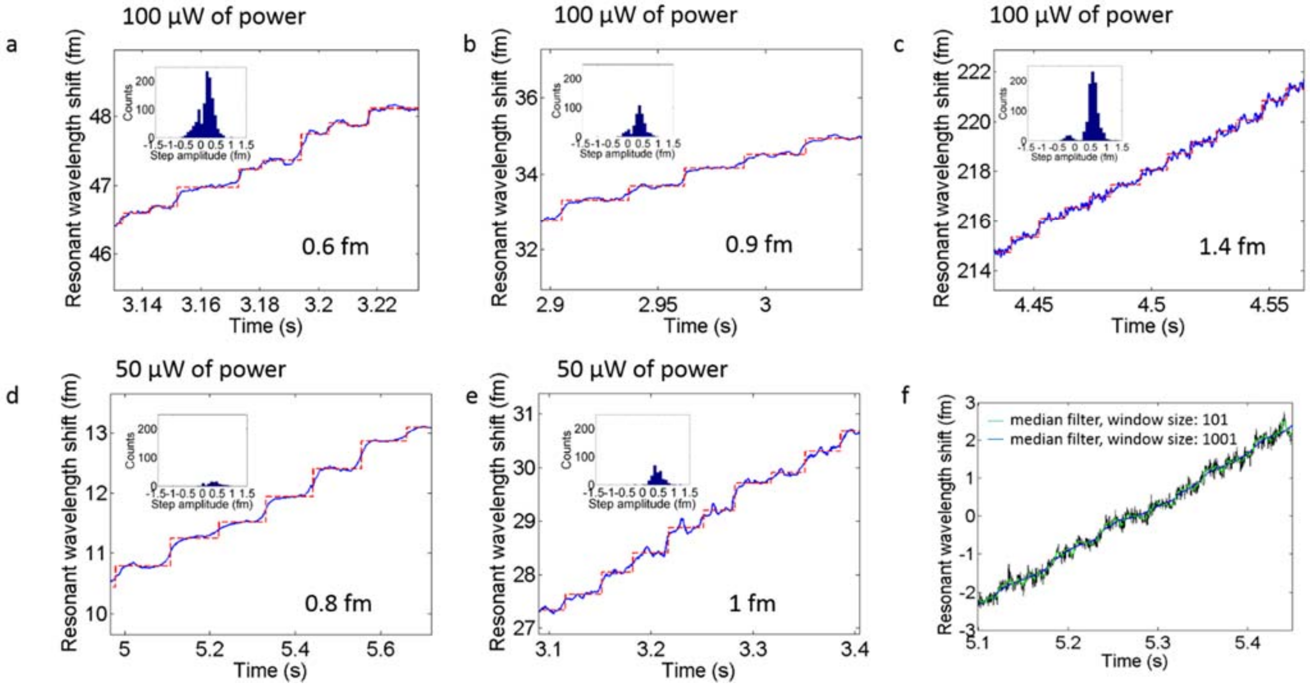

Extended Data Figure 5| 20 nm nanoparticle detection by the microtoroid at different input coupling powers shows no detectable difference in step amplitude. (a)-(c) Zoom-in of 20 nm nanoparticle detection experiments performed at 100 μW of input power. The resonant wavelength shift over time of the microtoroid as the nanoparticles bind to the microtoroid's surface is shown in blue. The step-fit is shown as a red dashed line. The insets show histograms of the step amplitude. The maximum step amplitude is reported in the lower right hand corner of each graph. **(d)-(e)** Zoom-in of 20 nm nanoparticle detection experiments performed at 50 μW of input power. The resonant wavelength shift over time of the microtoroid as the nanoparticles bind to the microtoroid's surface is shown in blue. The step-fit is shown as a red dashed line. The insets show histograms of the step amplitude. No observable difference in step amplitude was noticed between the two different powers. For consistency, a median filter window size of 1001 was used in all experiments throughout the paper, however, for visualization purposes in (a), (b), (c), and (e), median window filter sizes of 101, 101, 101, and 11, respectively were chosen. This does not significantly alter found step heights and locations but was done because for these specific cases due to differences in arrival times of the nanoparticles, a median widow size of 1001 tends creates an overly rounded step-appearance (f). **(f)** Data from (e), (shown in black) plotted with a median window filter size of 101 (green) and a median window filter size of 1001 (blue). Increasing the median window filter size to 1001 does not alter the step height and location, but creates an overly rounded appearance. These experiments were performed on the same microtoroid.

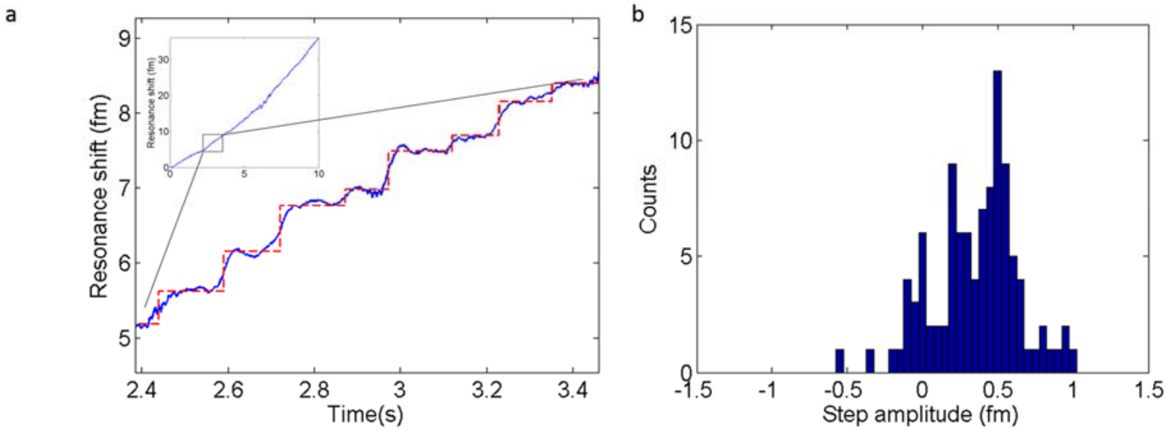

Extended Data Figure 6| Individual yeast ribosome (∼25 nm) detection. **(a)** Zoom in of the resonant wavelength shift (blue trace) over time of the microtoroid as ribosomes bind to the microtoroid's surface. The step-fit is shown superimposed as a red dashed line. This is a similar but different data set than is shown in Figure 5. (inset) Zoom-out of the toroid response over the full recording range of 10 seconds. **(b)** Histogram of step amplitudes. The mean step amplitude of ∼ 0.35 fm is similar to the value found in **Fig. 4a** (∼ 0.39 fm). A step amplitude of ∼ 0.35 fm corresponds to a particle diameter of 22 nm as predicted by our nanoparticle data thus suggesting that the binding of individual ribosomes is being observed.

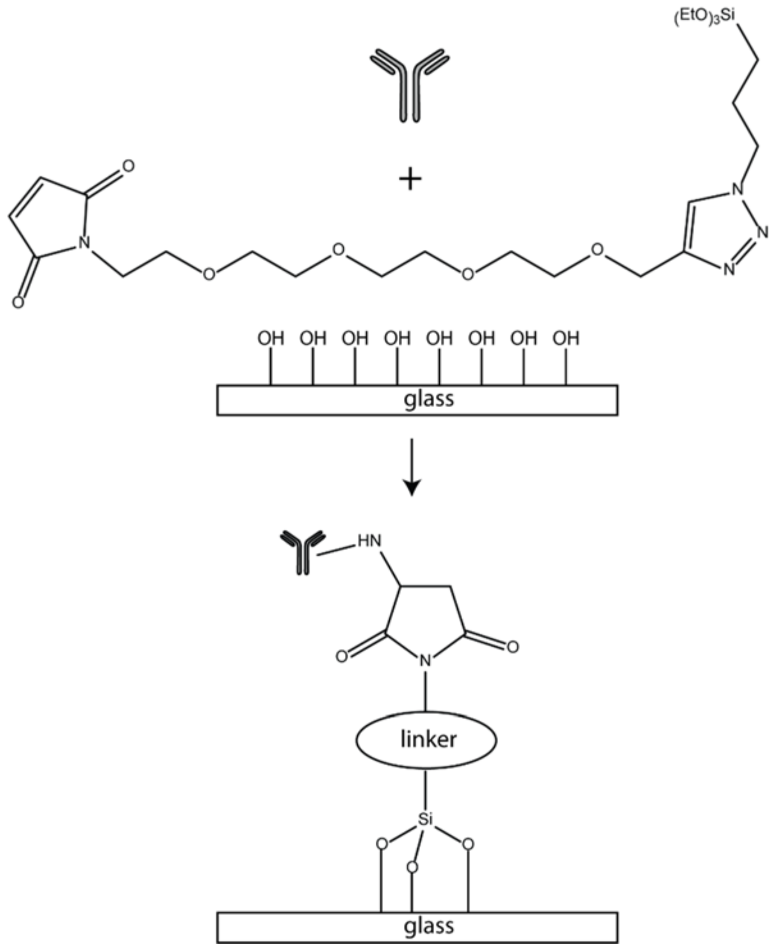

Extended Data Figure 7| Schematic demonstrating how the toroid's surface is sensitized for biological detection. A silane-PEG-maleimide linker (custom synthesis) is covalently bound to the surface of the toroid (represented as a glass substrate). Antibodies bind to the maleimide portion of the linker allowing for the selective detection of biological elements.

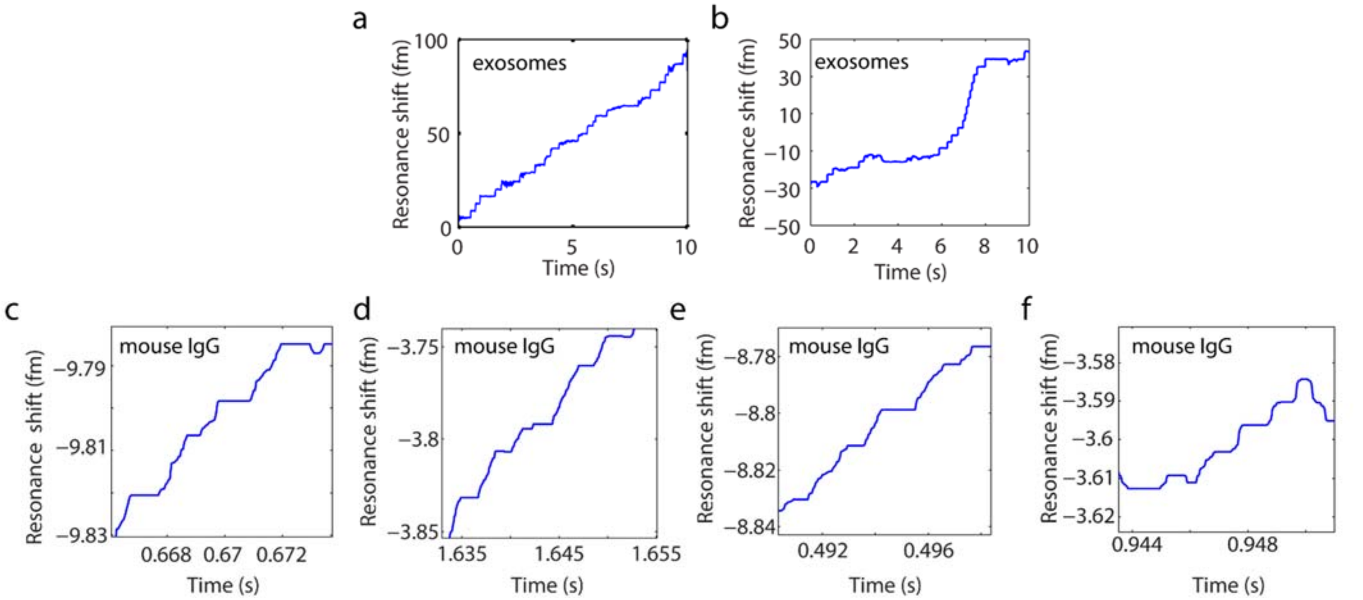

Extended Data Figure 8| Exosome and mouse IgG bioparticle detection data (a)-(b) Exosome detection recorded from two different experiments. As exosomes bind to the microtoroid's surface, the resonant wavelength of the microtoroid shifts as shown in the blue trace. Toroids were functionalized with the antibody CD-81. **(c)-(f)** Zoom-in of Mouse IgG detection data from four different experiments. As expected, the step amplitudes for the IgG detection are much smaller than for the exosome detection.

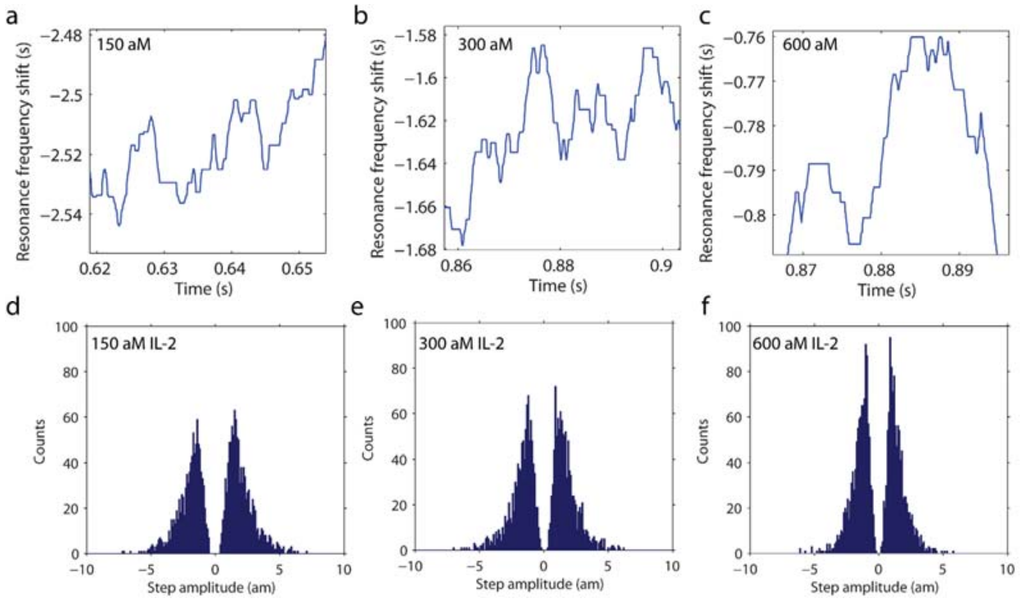

Extended Data Figure 9| IL-2 detection data at three different concentrations (a)-(c) Zoom-in of IL-2 step traces. Shown in blue is the resonance wavelength shift over time of the microtoroid as molecules bind to the microtoroid's surface. **(d)-(f)** Corresponding step amplitude histograms for **(a)-(c)**. As the concentration increases, the total number of particles increases in a linear fashion.

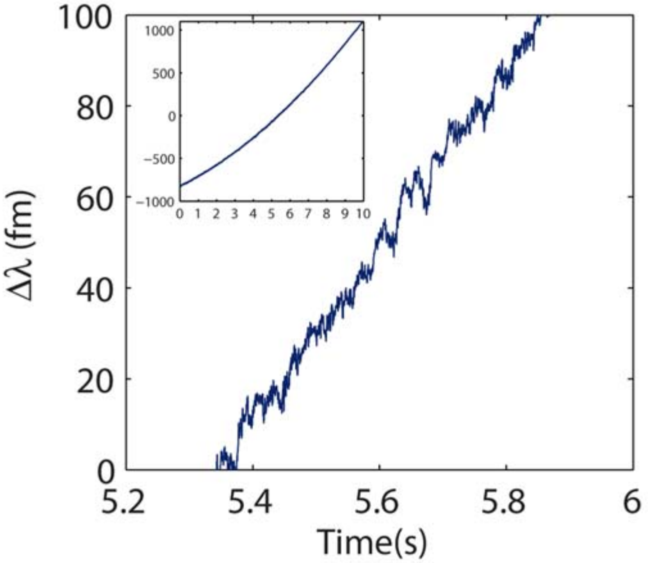

Extended Data Figure 10| Toroid functionalized with an irrelevant antibody for exosome binding shows no clean steps. Rituxan (control antibody) was bound to the surface of the microtoroid and exosomes flowed in. No distinct exosome binding events were observed.